Investigating the Characteristics and Origins of Primary Ultrafine Particles and New Particle Formation Events at the Rural Payerne Observatory

Master's thesis
Faculty of Science, University of Bern

handed in by

Lidia-Marta Amarandi-Netedu

2021

Supervisor

Prof. Dr. M. Schwikowski-Gigar

Co-Supervisor

Dr. M. Gysel-Beer

Advisor

Dr. B. T. Brem

Contents

Summary

Atmospheric aerosol particles affect the Earth-atmosphere system, including its climate, air quality and ecosystems. In addition, they affect human health. New particle formation (NPF) events are ubiquitous in the atmosphere. NPF is a two-step process consisting of a nucleation process with subsequent growth driven by condensation [Kulmala et al., 2004a]. NPF events are atmospherically relevant as a significant source of ultrafine particles (UFPs) together with primary UFP [Lee et al., 2019]. Understanding the NPF contributions to ambient UFP concentrations requires long-term observations.

This work investigates the nature of ultrafine particles at the semi-rural Payerne measurement site, in Switzerland, part of the National Air Pollution Monitoring Network (NABEL). The potential local sources of UFPs are the main road, the highway and the Payerne military airport. The main road is in the southern vicinity of the site at around 500 m while the Payerne military airport and the highway are located in the north at about 4 km from the site. The objective was centred on the distinction between primary UFPs and new particle formation events. The focus was on the frequency of occurrence, seasonality and potential origin of the primary particles and NPFs.

Normalized size distribution data in the range of 15-469 nm was provided by a Scanning Mobility Particle Sizer (SMPS) instrument. In addition, a Neutral cluster and Air Ion Spectrometer (NAIS) provided particle and positive and negative ion distributions ranging from 2.5 to 15 nm and 0.8 to 40 nm, respectively. A second SMPS down to 6 nm (nanoSMPS) and a Condensation Particle Counter (CPC) with a switchable catalytic volatile particle remover that operated downstream to 3 nm, provided information regarding the contribution of the non-volatile particles to total UFPs. Meteorological data from the Federal Office of Meteorology and Climatology (MeteoSwiss) and gaseous pollutants' information from NABEL/ Swiss Federal Laboratories for Materials Science and Technology (Empa) were further included in the data analysis. The meteorological parameters (temperature, solar radiation, relative humidity, precipitation, wind speed and wind direction), trace gas concentration (sulfuric acid (H_2SO_4) proxy) as well as NPF parameters (condensation sink (CS) and growth rate (GR)) provided information about the favourable atmospheric conditions for the occurrence of the NPF events.

During the measurement periods, high concentrations of UFPs were frequently observed at the Payerne site. The results indicated that even for this rather rural station setting, primary particles from on-road emissions observed during the rush-hours dominated these UFPs. During the colder season, primary UFPs were observed during morning and evening rush hour, in contrast to the warmer season, when they were pronounced only during morning rush hour, whereas in the afternoon a strong dilution by boundary layer dynamics occurred. The wind was mainly blowing from the airport and main road directions, but it was associated with low particle number concentration values, showing a weak influence of wind direction on UFPs.

By contrast, NPF events with distinct nucleation and growth were detected mainly around noontime. Also, from the seasonality data, more NPF events occurred during the warmer season (40 events between March-May) compared to the colder season (7 events between October-February). Meteorological parameters were relevant in finding similarities between NPF events. High solar radiation and temperature values were correlated with a higher NPF frequency, while RH was anticorrelated. Regarding the relation between H_2SO_4 proxy and NPF, its concentrations were high enough to trigger NPF, as was shown in previous studies from other rural locations. Low CS values were associated with high NPF occurrence. CS and GR were calculated and compared to other rural stations ([Nieminen et al., 2018], [Dada et al., 2020]).

With this study, it can be concluded that UFPs dominated the total particle number even at the rural Payerne site. They exhibited diurnal (both primary UFPs and NPF) and seasonal (only NPF) patterns. The primary UFPs were detected as coming from two sources, on-road vehicles and gas-turbine aeroplanes. The parameters characterizing NPFs (GR and CS) were in the same range as at other rural sites, and the trace gas conditions were similar to usual conditions during an event. As future outlook that could improve the work, investigating the seasonally dependent frequency of occurrence would require long-term measurements. Also, chemistry data, e.g. Highly-Oxygenated organic Molecules, would provide more information about the origins and growth of the UFPs. From the analysis point of view, a separation between weekdays and weekends as well as boundary layer measurements could help to improve the understanding of primary UFPs' influence. Automatic detection of NPF events could be done using machine learning.

Abbreviations

Notation	Meaning
ACI	Aerosol-Cloud Interactions
ACTRIS	Aerosols, Clouds and Trace gases Research Infrastructure
NH_3	Ammonia
BC	Black Carbon
BL	Boundary Layer
CET	Central European Time
CEST	Central European Summer Time
CCN	Cloud Condensation Nuclei
CI-APi-ToF	Chemical Ionization Atmospheric-Pressure interface Time-of-Flight mass spectrometer
CLOUD	Cosmics Leaving Outdoor Droplets
CPC	Condensation Particle Counter
CS	Condensation Sink [s^{-1}]
DMA	Differential Mobility Analyzer
DPF	Diesel Particulate Filters
eBC	equivalent Black Carbon [ng/m^3]
ELVOC	Extremely Low Volatile Organic Compound
EMPA	Swiss Federal Laboratories for Materials Science and Technology
ERF	Effective Radiative Forcing [Wm^{-2}]
GDE	General Dynamic Equation
GDI	Gasoline Direct-Injection
GR	Growth Rate [nm/h]
H_2SO_4	Sulfuric acid
HOM	Highly Oxygenated organic Molecule
IIN	Ion-Induced Nucleation
JFJ	Jungfraujoch (measurement location at 3580 m a.s.l.)
LVOC	Low Volatile Organic Compound
LT	Local Time
MeteoSwiss	Federal Office of Meteorology and Climatology
NABEL	National Air Pollution Monitoring Network
NAIS	Neutral Cluster and Air Ion Spectrometer
NO_x	Nitrogen oxides
NH_3	Ammonia
NPF	New Particle Formation
PM	Particulate Matter
PDF	Probability Density Function
PSI	Paul Scherrer Institute
rBC	refractory Black Carbon
RH	Relative Humidity[%]
SMEAR II	Station for Measuring Forest Ecosystem-Atmosphere Relations II
SMPS	Scanning Mobility Particle Sizer
SO_2	Sulfur dioxide
SS	Supersaturation
SVOC	Semi-Volatile Organic Compound
UFP	Ultrafine particle
VBS	Volatility Basis Set
VOC	Volatile Organic Compound

List of Figures

List of Tables

1 Introduction

1.1 Atmospheric aerosols

1.1.1 Definition and classification

A particulate matter (PM) is "a suspension of fine solid or liquid particles in a gas (...) that ranges in size from a few nanometres (nm) to tens of micrometres (µm) in diameter" [Seinfeld and Pandis, 2006, p. 55]. Generally, an aerosol is referred to as the particulate component only. There are four modes of atmospheric aerosols that can be observed in the number, surface, volume or mass size distributions:

1. Nucleation mode: diameter $<$ 20 nm
2. Aitken mode: 20 nm $<$ diameter $<$ 0.1 µm
3. Accumulation mode: 0.1 µm $<$ diameter $<$ 2.5 µm
4. Coarse mode: diameter $>$ 2.5 µm.

The particles smaller than 0.1 µm in diameter are referred to as ultrafine particles (UFPs), the ones smaller than 2.5 µm as fine particles, while the ones larger than 2.5 µm as coarse particles [Seinfeld and Pandis, 2006]. In all the previous definitions, the diameters stated refer to the aerodynamic diameter, which is the most relevant for public health. The aerodynamic diameter of a particle is the diameter of a sphere particle with density equal to 1 g·cm^{-3}, having the same settling velocity as the particle [Seinfeld and Pandis, 2006].

Figure 1 illustrates the number and volume distributions of atmospheric particles with their related modes and submodes. The volume distribution is dominated by two modes: accumulation and coarse modes. Nucleation and Aitken modes often dominate the number distribution. However, at times the accumulation mode can give a major or even dominant contribution to the number, too. By contrast, nucleation mode never dominates mass distribution and Aitken mode rarely does.

Accumulation mode consists of two overlapping submodes: condensation and droplet submodes. Condensation submode is the result of primary particle emissions and the growth of ultrafine particles by coagulation and vapour condensation. The droplet submode is created by the cloud processing of some of the accumulation mode particles [Seinfeld and Pandis, 2006].

The typical particle number concentrations of natural atmospheric aerosols are between 100 and 1000 cm^{-3} in continental air and between 100 and 500 cm^{-3} in marine air [Ramanathan, 2006].

1.1.2 Sources and production mechanisms

Aerosol particles are both natural and anthropogenic. Natural sources include sea salt, mineral dust, volcanoes, wildfires. Anthropogenic sources refer to man-made activities, such as fossil fuels combustion, biomass burning, agriculture, industry. Aerosol particles are either primary particles directly emitted into the atmosphere or secondary PM. Secondary PM are defined as the chemical transformation of precursor gases to PM via gas-to-particle conversion [Seinfeld and Pandis, 2006].

Primary particles are emitted directly from natural (volcanoes, wildfires, sea salt, dust) and anthropogenic sources (fossil fuel burning in combustion engines and power plants) [Reddington et al., 2011]. Generally, incomplete combustion of fossil fuels, gas-turbine engines, wood stoves are often considered the main source of primary UFPs [Brines et al., 2015]. However, incomplete combustion could also emit precursors gases of secondary PM [Chirico et al., 2010].

Both natural and anthropogenic sources contribute to the emissions of the precursors of secondary PM, e.g. sulfur dioxide (SO_2) from sulfur-containing fuel combustion, nitrogen oxides (NO_x) from fossil fuel combustion, ammonia (NH_3) from agricultural activities and volatile organic compounds (VOCs) (from vegetation) [Fuzzi et al.,

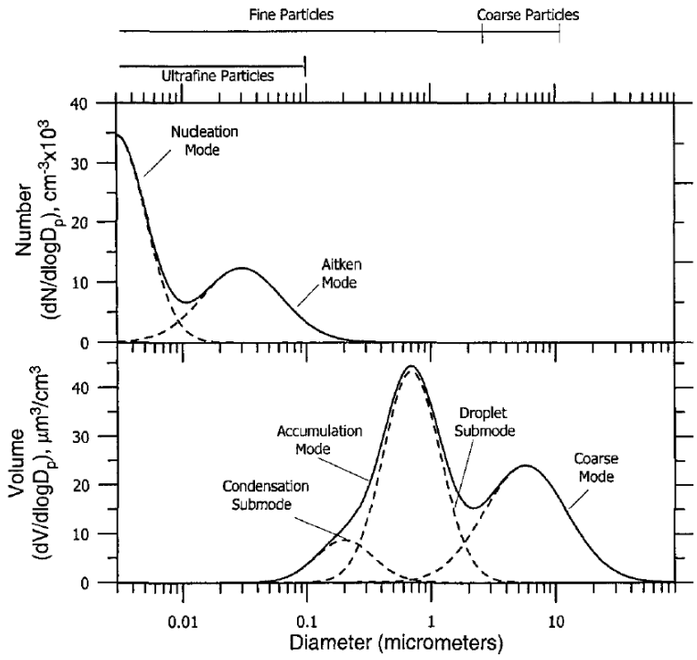

Figure 1: Number and volume distributions of atmospheric particles for different modes [Seinfeld and Pandis, 2006].

2015]. Figure 2 is a schematic for secondary PM. The grey, green and gold arrows show the competing processes of condensable precursor vapours that are further described below. Secondary PM are produced via gas-to-particle conversion from precursor gases in two ways (grey arrows). One way is represented by the condensation of precursor gases on preexisting particles. The second way is the nucleation of precursor gases, forming clusters around 1 nm in diameter. A cluster is defined as a finite-size system made of PM. The nucleation is usually driven by photochemical production of nucleating vapours such as low volatile organic compounds (LVOCs) and sulfuric acid (H_2SO_4) [Lee et al., 2019]. By the atmospheric oxidation of precursor gases through photochemistry, the saturation vapour pressure lowers and the molecules can condense and nucleate, thus partition into particulate phase [Alanen et al., 2017]. Clusters can either grow and form secondary PM (in the UFPs range) or be lost by coagulation (green arrows), depending on the growth rate (GR) of the particles. The growth of the initial cluster is mainly enhanced by extremely low volatile organic compounds (ELVOCs) and LVOCs [Tröstl et al., 2016a], [Shrivastava et al., 2016], [Matsui et al., 2011]. Cluster formation from precursor gases by nucleation and subsequent growth of clusters to stable new particles is called new particle formation (NPF) [Lee et al., 2019].

In some cases, the newly formed particles (both from condensation and NPF) can become cloud condensation nuclei (CCN) active (blue and yellow arrows in Figure 2, respectively). In these circumstances, secondary PM formed from NPF can also be lost by coagulation (yellow arrows). The ability of the particles to become CCN active depends on their size, chemical composition and hygroscopicity. Hygroscopicity represents the ability to absorb water by soluble substances. In general, the hygroscopicity of an aerosol particle depends on its chemical composition [Pöschl et al., 2009]. Depending on the site location, the chemical composition exhibits variations, from organic PM, especially in the absence of long-range transport of other chemical constituents, to inorganic components, predominantly ammonium nitrate, in high-NO_x regions [Schmale et al., 2018]. Usually, accumulation mode particles are more hygroscopic compared to Aitken mode particles. Therefore, the minimum required particle size to be CCN active is found between these two particle modes [Mcfiggans et al., 2006]. Between 10 and 60% of the NPF events (NPF that occurred between a specific time period) grow to 50-100 nm to become CCN active [Lee et al., 2019].

On the other hand, primary particles contribute about 55% of global CCN number concentrations at 0.2% supersaturation (SS) in the boundary layer (BL) and up to 70% in polluted continental regions. Also, the uncertainty in the size distribution of the emitted particles leads to an uncertainty in the contribution of primary particles to CCN [Merikanto et al., 2009].

Concerning the global mass emissions of atmospheric particles, Figure 3 suggests that the majority of aerosols are mostly of natural rather than anthropogenic origin, approximately 12,000 to 300 Tg/year, respectively. Primary and secondary atmospheric particle fluxes are expressed in teragram per year (Tg = 1012 g = 1 Mt) [Gieré and Querol, 2010].

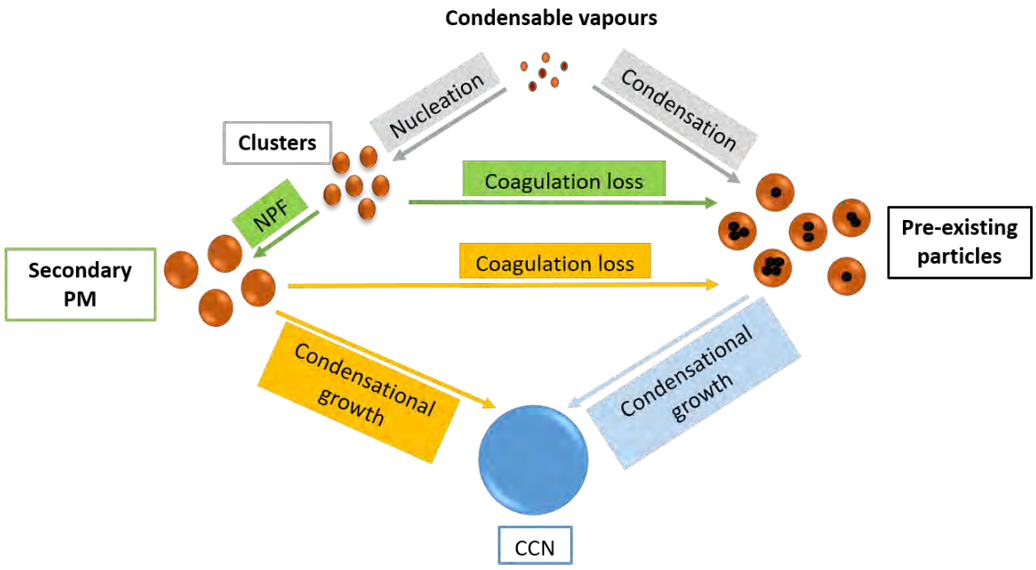

Figure 2: Diagram illustrating the formation of secondary PM via nucleation and condensation and further growth until CCN activation. Adapted from [Matsui et al., 2011]

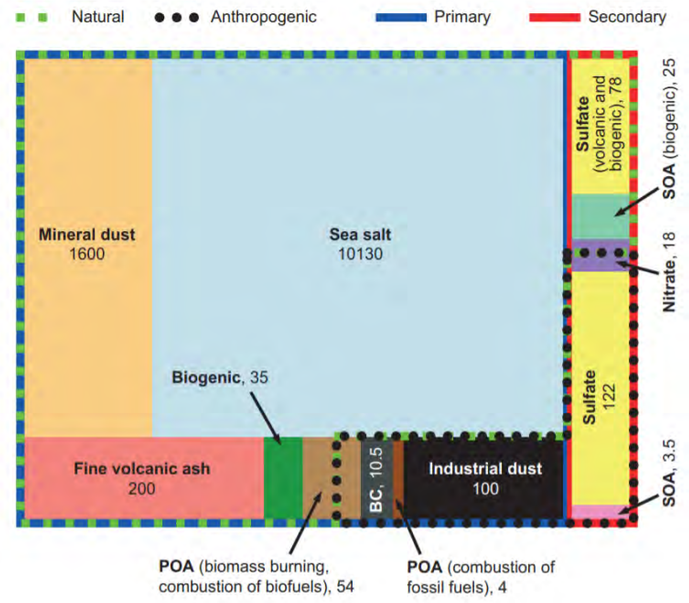

Figure 3: Primary and secondary atmospheric aerosols in teragram per year ($\mathrm{Tg} = 1012\,\mathrm{g} = 1\,\mathrm{Mt}$). The data distinguishes the aerosols according to their source (natural and anthropogenic). POA = primary organic aerosol; SOA = secondary organic aerosol; BC = black carbon [Gieré and Querol, 2010].

1.1.3 Removal processes from the atmosphere

The removal of the aerosols from the atmosphere occurs through either dry deposition or wet deposition. Dry deposition includes the removal of aerosol particles by collision at the Earth's surface by gravitational settling, impaction, interception and/or diffusion. Wet deposition occurs through precipitation of hydrometeors containing PM. Particles can enter hydrometeor by acting as in-cloud scavenging through cloud droplets formation or below-cloud scavenging through the uptake of aerosol particles forming cloud droplets followed by precipitation [Fuzzi et al., 2015]. Due to wet and dry depositions, the lifetime of fine particles in the troposphere is between a few days and a few weeks. Globally, wet deposition dominates their lifetime, but dry deposition is dominant in the absence of precipitation [Farmer et al., 2021]. Spatio-temporal variations in concentration and physical and chemical properties of tropospheric aerosols are a consequence of a variety of sources and transport and transformation processes combined with the short lifetime (between a few days and a few weeks) [Seinfeld and Pandis, 2006].

1.1.4 Environmental impacts

Aerosols particles impact climate, environment and health. Regarding their effect on climate, they influence it in three ways: (1) by scattering incoming solar radiation leading to cooling, (2) by absorbing incoming solar radiation, thus warming the atmosphere, and (3) by changing cloud properties by acting as CCN. The first two ways are commonly referred to as an aerosol-radiation interaction while the latter effect is often referred to as aerosol–cloud interactions (ACI) [An et al., 2019]. ACI can also happen through ice nucleating particles. However, this subject will not be further deepened, since it is not related to our study.

Because aerosol particles can lead to cooling or warming of the atmosphere, the uncertainty in the effective radiative forcing (ERF) is high. The total net radiative forcing of greenhouse gases, aerosols and the total anthropogenic radiative forcing is shown in Figure 4 [Haywood, 2016]. ERF is estimated over the Industrial Era from 1750 to 2011. On the y-axis is presented the probability density function (PDF), which generally describes the probability of a random variable to be found in a specific interval. PDF of aerosols exhibits a wider shape compare to the PDF of the greenhouse gases, owing to the much higher relative uncertainty. Therefore, the large uncertainty in the aerosol forcing leads to the large uncertainty in the total anthropogenic ERF [IPCC, 2013]. Moreover, their effect on the environment is seen in decreasing visibility and causing acid rain, depending on their chemical composition [Malm et al., 1994], [Singh and Dey, 2012].

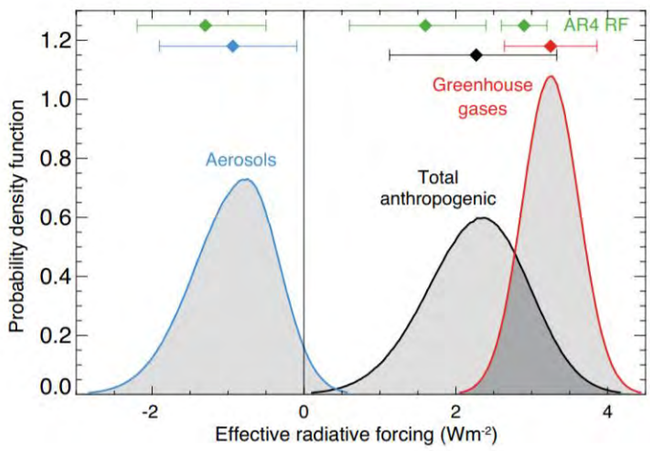

Figure 4: The probability density function of the total effective radiative forcing of aerosols (blue line), greenhouse gases (red line), and the net radiative forcing of all anthropogenic forcings (black line). The x-axis represents the effective radiative forcing [Wm^{-2}] over the Industrial Era from 1750 to 2011 [IPCC, 2013].

Their impact on health is different, depending on their size. Some health problems due to aerosol particles that can appear are respiratory, cardiovascular, and pregnancy complications [Oh et al., 2020]. Long-term exposure to combustion-related fine particles increases the risk of cardiopulmonary and lung cancer mortality [Pope III et al., 2002], [Dockery et al., 2010]. As shown in Figure 5, aerosol particles have the ability to penetrate the alveolar regions in the human respiratory system. The solid UFPs are suspected to even translocate into the blood and lymph circulatory systems [Lajili, 2019].

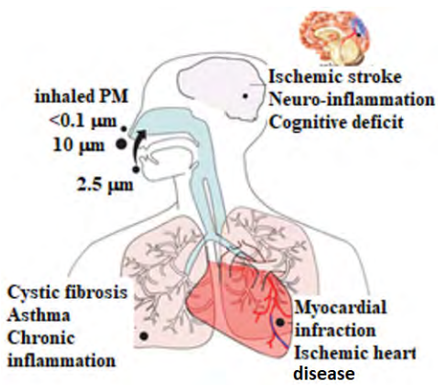

Figure 5: The effects of ultrafine and fine aerosols on human health by air inhalation [Lajili, 2019].

1.1.5 Equivalent black carbon and primary semi-volatile aerosols

Black carbon (BC) is a primary aerosol, which is the dominant form of light-absorbing aerosols. It is emitted from both anthropogenic and natural incomplete combustion processes by cooling of exhaust gas. The anthropogenic incomplete combustion usually comes from diesel engines or anthropogenic biomass burning, while the natural processes are related to wildfires [Manchester University - Centre for Atmospheric Science]. BC absorbs light in the range of 400 (visible)-1200 (infrared) µm and has a warming effect on the atmosphere [Kamita et al., 2016], [Alanen et al., 2017]. Its lifetime in the atmosphere is between 1-2 weeks, showing a regional impact [Manchester University - Centre for Atmospheric Science].

In the range of 20-30 nm, particles can form as a result of nucleation in two ways: (1) atmospheric oxidation of precursor gases and (2) fast cooling of exhaust emission gases. For the first way, the gases are semi-volatile atmospheric compounds. Regarding the second way, the cooling of exhaust emission gases is dependent on several factors: the dilution ratio, ambient temperature, preexisting particle surface area concentration, and sulfur content found in fuel. If there is high enough supersaturation, the components in the gas phase in hot exhaust gas convert to the condensed phase after cooling. Thus, black carbon (soot), a non-volatile product from incomplete combustion, can act as a condensation sink (CS) and the nucleation mode is absent in the size range. New particle formation can occur for temperature values that are lower enough and without any change in the gaseous precursors through chemical reactions [Baltensperger et al., 2002].

Equivalent BC (eBC) is used for data derived from optical absorption methods [Petzold et al., 2013]. To find the mass concentration without other species interference, e.g. organic species, the wavelength should be in the infrared range (780-1000 nm).

1.1.6 Volatility

The volatility of a chemical compound is a physical property that describes the partitioning of the components of a substance between the vapour and solid phases. If a compound has high volatility, this can relate to having high saturation vapour pressure. The saturation vapour pressure is a specific property of a compound [Cain et al., 2020].

Depending on their chemical composition, small UFPs can have different volatility. Because the composition of primary UFPs and newly formed particles differs, the volatility can be a way to distinguish them. Therefore, volatility data provides evidence if the sources of atmospheric particles are primary or secondary emissions. Primary UFPs show a lower volatile fraction, coming from fuel combustion sources with BC as primary constituent [Cass et al., 2000]. By contrast, NPF is associated with high volatility. This association can be explained as follows: semi-volatile organic compounds (SVOCs) typically make a major contribution to the condensation growth of freshly nucleated particles. Even sulfate and LVOCs may evaporate when heated to temperatures of several hundreds °C.

1.2 Continuous representation of particle size distributions

To understand the physics and chemistry of the aerosol clusters, we need to understand the behaviour of a cluster interacting with each other. The discussion is based on the changes that occur in the cluster when a vapour condenses on particles and when particles collide and stick on other particles [Seinfeld and Pandis, 2006].

Discrete and continuous distributions can be used to describe the number concentration of aerosol particles in the atmosphere. However, in practice, due to the large number of particles in wide size range, continuous distribution is used. Because of the large size range, the distribution is usually represented as a function of natural or decimal logarithm of particle diameter, $\ln D_p$ or $\log D_p$, respectively. Because it is not possible to take a logarithm of a dimensional quantity, the $\log D_p$ actually means $\log D_p/1$. 1 represents a "reference" particle with diameter of 1 µm. The number distribution function $n_N^e(\log D_p)$ can be defined as the number of particles per cubic centimetre of air having the diameter in the size range $\log D_p$ to $\log D_p + d\log D_p$.

The total aerosol number concentration N_t [cm^{-3}] is defined as:

$$N_t = \int_{-\infty}^{\infty} n_N^e(\log D_p)\, d\log D_p \tag{1}$$

Moreover, the aerosol distributions can be described also for surface area, volume or mass. Even if the functions are not equal, they can relate to each other by using the radius or diameter as an independent variable [Seinfeld and Pandis, 2006].

1.3 General dynamic equation

Gas-to-particle conversion, coagulation and particle transport change the distribution function with time and position. These processes are included into a general dynamic equation (GDE) for the continuous distribution function ($n(v,\ t)$), represented in equation 2 [Sandu, 2006]. The aerosol distribution encounters a series of physical and chemical transformations that lead to changes in number concentration [Seinfeld and Pandis, 2006].

The terms in the GDE (equation 2) describe, in order, the modification of the particle number due to growth due to condensation/evaporation, production and loss of particles of volume v due to coagulation, increase in particle number due to sources S (nucleation and emissions) and decrease in particle number due to depositions R. $I(v,\ t)$ represents the growth rate due to condensation/evaporation. $\beta_{v,w}$ is equal to $\beta_{w,v}$ and represents the coagulation function [Sandu, 2006].

$$\begin{aligned}\frac{\partial n(v,t)}{\partial t} = &-\frac{\partial[I(v)n(v,t)]}{\partial v} \\ &+ \frac{1}{2}\int_0^v \beta_{v-w,w} n(v-w,t)n(w,t)\, dv + n(v,\ t)\int_0^{\infty} \beta_{v,w} n(w,t)n(w,t)\, dv \\ &+ S(v,\ t) - R(v,\ t)\ n(v,\ t)\end{aligned} \tag{2}$$

GDE for the continuous distribution function describes the following physical and chemical transformations: increase in particle number due to nucleation and emissions, and decrease in the number of particles due to coagulation and deposition [Sandu, 2006]. In the absence of nucleation, emissions, deposition and growth, GDE for the continuous distribution function becomes the continuous coagulation equation. Without emissions and deposition terms, the equation is simplified to the condensation equation [Seinfeld and Pandis, 2006].

Condensation is defined as the process of vapour converting into liquid or solid form. Condensation can occur on particles, changing the particle diameter. The shape of the particle size distribution also changes. During condensation, the number of particles remains constant while the volume increases due to the size growth [Seinfeld and Pandis, 2006].

Coagulation represents the collision between the aerosol particles due to their Brownian motion or other forces, e.g. electrical, gravitational forces. Coagulation is most efficient between small and large particles [Saltzman, 2009]. During coagulation, the volume of particles remains constant. If both condensation and coagulation processes occur simultaneously, the total particle number decreases while the volume increases [Seinfeld and Pandis, 2006]. Coagulation loss term is defined as the removal rate of particles because of collisions with other particles of any size [Dal Maso, 2002].

1.4 Physical transformation process of aerosol particles - nucleation

1.4.1 Nucleation theory

Nucleation is a physical process by which gas molecules aggregate and form a cluster. There are two types of nucleation regarding the existence of a foreign substance: homogeneous (nucleation of vapour on embryos formed of vapour molecules only, in the absence of foreign substances) and heterogeneous (nucleation on a foreign substance or surface, e.g. an ion or a solid particle). Moreover, looking at the involving species, nucleation can be homomolecular (single species) and heteromolecular (two or more species) [Seinfeld and Pandis, 2006].

Nucleation mode particles are observed in different environments around the globe, such as forest, urban, rural, continental area. The sources of precursor gases are both natural, e.g. biogenic organic compounds in forest area, and anthropogenic, e.g. fossil fuel combustion, industry, agriculture (machinery, animal waste, fertilizers). The chemical composition of the particles in the nucleation mode includes sulfate, black carbon, metal compounds, low-volatility organic compounds.

Nucleation mode particles can be emitted directly or form from vapours. The second way requires supersaturation formed either if there is increasing production of condensable vapours, either if the temperature is low enough, so the saturation vapour pressure lowers. Given that coagulation is efficient between small and large particles, coagulation is an important process for the evolution of size distribution and survival probability of newly formed nucleation mode sized particles [Stauffer and Kiang, 1974]. During the nucleation process, both total particle number and volume increase [Seinfeld and Pandis, 2006].

The classical nucleation theory (CNT) describes homogeneous-homomolecular nucleation. From the CNT perspective, nucleation happens when a closed thermodynamic system with fixed pressure and temperature is in a metastable state, corresponding to a local minimum of free energy. For the system to go from a metastable state to a stable state (global minimum of free energy), it needs to overcome the barrier of local maximum of free energy [Kalilmanov, 2013].

The energetic approach includes Gibbs free energy G, which is a thermodynamic potential that shows how much energy is in the system. For neutral clusters which exclude charged particles, the Gibbs free energy is defined as it follows [Curtius, 2006]:

$$\Delta G = - \frac{4}{3}\pi {R_p}^3 \frac{kT}{\nu} lnS + 4\pi {R_p}^2 \sigma, \tag{3}$$

where:

R_p: nucleating particle's radius,

p_A: vapour pressure of substance A,

${p_A}^\infty$: equilibrium vapour pressure over a flat surface of liquid,

S: saturation ratio, with $S = \frac{p_A}{{p_A}^\infty}$,

k: Boltzmann constant,

T: temperature,

ν: volume occupied per molecule, and

σ: surface tension.

Figure 6 illustrates the thermodynamic representation of the neutral pathway of homomolecular homogeneous nucleation. Y-axis shows the Gibbs free energy, while the particle radius is on the x-axis. The black line constitutes the nucleation barrier. ΔG^* is the nucleation barrier of height and ${R_p}^*$ is the critical cluster size at the maximum of the barrier [Curtius, 2006].

Supersaturation is the driving force for the gas-phase molecules to condense, thus increasing the particle radius. If the system is supersaturated, then $S > 1$, and the first term on the right-hand side of the above equation is negative.

In the beginning, for small values of R_p, the second term has the main role. As the particle forms, a new surface is growing, which needs energy. The surface energy is greater than the energy gained from changing from the gas-to-particle phase. Hence, there is an effective energy barrier that prevents the gas from nucleation, even if it is supersaturated in the gas phase concerning the flat surface equilibrium pressure.

The critical radius is at the maximum of the barrier. If the cluster of molecules reached the critical radius, it will more likely grow further by condensation. If the cluster does not reach the critical radius, then energetically the

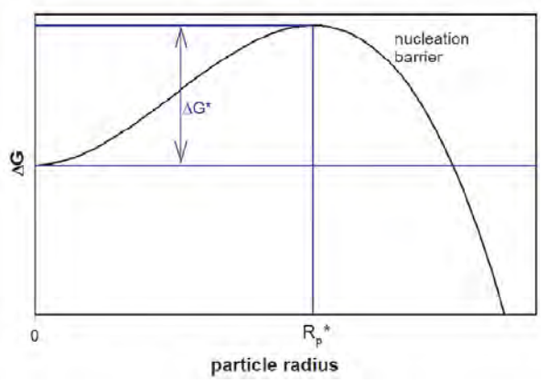

Figure 6: Thermodynamic representation of aerosol nucleation for a single chemical compound. ΔG^* is the nucleation barrier of height and ${R_p}^*$ is the critical cluster size at the maximum of the barrier [Curtius, 2006].

molecules are more prone to evaporation than another molecule condensing on them and the clusters will separate into gas molecules again.

Nucleation mode particles would require very high supersaturation of water to act as cloud condensation nuclei. Therefore, they first need to grow to reach several tens of nanometers in diameter before they reach the size range in which they can act as CCN at typical atmospheric supersaturation. If the growth is faster enough, the particle loss through coagulation is smaller and more particles become CCN [Lajili, 2019].

In contrast to neutral clusters, atmospheric ions, which are produced by cosmic rays or due to natural or anthropogenic radioactivity, can form stable molecular clusters, leading to ion-induced nucleation (IIN). Compared to homogeneous nucleation (neutral nucleation), when the cluster is formed around the molecules that condense, for IIN, the cluster forms around an ion. The electrostatic interaction between the ion and condensing molecules lowers the free energy required for the cluster to form [Seinfeld and Pandis, 2006], [Lovejoy et al., 2004]. IIN clusters can also form by recombination of oppositely charged clusters. Consequently, IIN can be dominant in unfavourable conditions for neutral nucleation. IIN has an upper rate limit given by the ion formation rate, whereas neutral channel formation rates have no upper limit with increasing supersaturation [Bianchi et al., 2016], [Eisele et al., 2006].

Tropospheric ions concentrations (10^2–10^3 cm^{-3}) are much smaller than neutral gas ones (10^9 cm^{-3}). Even if ion-neutral reaction rate coefficients are about an order of magnitude faster compared to neutral ones, because of such low concentrations, ions are assumed to not show a major influence on tropospheric chemistry. On the other hand, ions possess an influence in the cases where they allow reactions that would not be possible otherwise. At low temperatures, IIN occurs with almost no potential barrier. Therefore, low ion concentrations could initiate the ion cluster production, which could further lead to NPF. In these cases, IIN is limited by atmospheric ion production rates, which show a high level at higher altitudes and sulfuric acid concentrations [Eisele et al., 2006], [Lovejoy et al., 2004].

1.4.1.1 Nucleation of sulfuric acid

Previous studies ([Weber et al., 1996], [Kulmala et al., 2004b], [Sihto et al., 2006]) had shown that sulfuric acid (H_2SO_4) is a key driver for NPF events, especially because of its low volatility. It is produced in the atmosphere by oxidation of sulfur dioxide emitted from e.g. fossil fuel combustion, power plants, volcanoes. The atmospheric measurements of gas-phase sulfuric acid are difficult to conduct because the sulfuric acid concentration is low (10^5-10^7 molecules cm^{-3} or lower) [Berndt et al., 2010]. The measurements can be done only with state-of-art instruments, e.g. chemical ionization atmospheric-pressure interface time-of-flight mass spectrometer(CI-APi-ToF) [Dada et al., 2020].

Berndt et al. [2010] conducted nucleation experiments in an atmospheric pressure flow-tube. The input gases were a premixed humidified air with SO_2, O_3, H_2 and CO or 1,3,5-trimethylbenzene. The sulfuric acid concentration was detected at a maximum of $5{\cdot}10^4$ molecules cm^{-3} for a 5 minute integration period.

Moreover, their lab calculated the sulfuric acid concentration by models. There is 1:1 correspondence

between the measured and calculated values using models was in good agreement until (3-5)·10^7 molecules cm^{-3}. By adding H_2 and CO or 1,3,5-trimethylbenzene, the nucleation did not show a change. However, additional NH_3 enhanced the nucleation rate and growth [Berndt et al., 2010].

Whenever sulfuric acid vapour concentration measurements are not available, the concentrations can be estimated from other parameters affecting the source and sink terms. For the estimation, a proxy that covers physical and chemical parameters is needed. Dada et al. [2020] proposed the sulfuric acid proxy, considering the production of gas-phase sulfuric acid from sulfur dioxide (SO_2) chemically reacting with hydroxyl radical (OH·) as oxidant, as is presented in the proxy equation 4. Moreover, the CS and the molecular cluster formation were taken into consideration. The hypotheses were evaluated by the measurements in four different locations, covering a semi-pristine boreal forest, rural environment in the Mediterranean area, urban environment, and heavily polluted megacity, respectively. Moreover, the proxy was verified by independent data sets. Consequently, sulfuric acid concentration can be estimated for different environment types. For the rural location located in Agia Marina, Cyprus, the stated correlation between the measured values and the proxy concentration of the sulfuric acid was 0.88. For our measurement site, which is semi-rural, we used the rural sulfuric acid proxy, with its equation below [Dada et al., 2020]:

$$C_{H_2SO_4} = -\frac{CS}{2 \cdot (2 \cdot 10^{-9})} + \left[\left(-\frac{CS}{2 \cdot (2 \cdot 10^{-9})}\right)^2 + \frac{C_{SO_2}}{2 \cdot 10^{-9}} \cdot 9 \cdot 10^{-9} \cdot G_g\right]^{1/2}, \quad (4)$$

where $C_{H_2SO_4}$ [cm^{-3}] is the sulfuric acid concentration. CS [s^{-1}] represents the value of condensation sink calculated for sulfuric acid as the diffused gas that is lost to the particles. C_{SO_2} [cm^{-3}] is the measured concentration of sulfur dioxide and G_g [W/m^2] represents the global radiation for values greater than 50 Wm^{-2}.

1.4.1.2 Nucleation of organic vapours

Even if sulfuric acid vapour is involved in nucleation, it cannot explain the observed growth related to NPF due to its insufficient concentration in the atmosphere. Cosmics Leaving Outdoor Droplets (CLOUD) chamber experiments revealed that organic vapours can be the mechanism of the initial growth, at least in the planetary boundary layer. The experiments were conducted at atmospheric conditions, in the absence of inorganic acids and bases, e.g. sulfuric acid or ammonia (NH_3) and amines, respectively Tröstl et al. [2016a].

The ability of organic vapours to drive or not the initial growth is related to the volatility. If they possess extremely low volatility, then they can be the driver of the growth. As the size of the cluster increases, the nucleation barrier falls. The subsequent growth is mainly due to more abundant organic vapours, volatile organic compounds (VOCs), which undergo oxidation reactions in the atmosphere, lowering the volatility and leading to low volatile organic compounds (LVOCs) or extremely LVOCs (ELVOCs). LVOCs and ELVOCs drive the initial growth of NPF.

The atmospheric oxidants are hydroxyl radical (OH·), ozone (O_3), nitrate radical (NO_3·), and chlorine radicals (Cl·). OH· is under daytime, NO_3· under night time, and O_3 under both day and night time chemistry, respectively. Cl· is a minor contributor, with similar reactions as OH·.

Generally, atmospheric LVOCs or ELVOC are highly oxygenated molecules (HOMs). They are formed in the atmosphere via autoxidation involving peroxy radicals (RO_2·) arising from VOC. Their volatility is not exactly known. They have six or more oxygen atoms [Bianchi et al., 2019]. Formation of HOMs occurs in the first steps of oxidation in a time period of seconds-minutes [Almeida et al., 2013].

1.5 New particle formation parameters

1.5.1 Growth rate

The growth rate (GR) is defined as the rate of change in the diameter, d_p, being the growing particle.

$$GR = \frac{dd_p}{t} = \frac{\Delta d_p}{\Delta t} = \frac{d_{p_2} - d_{p_1}}{t_2 - t_1} \ , \tag{5}$$

where d_{p_1} and d_{p_2} are the particle diameters at time t_1 and t_2, respectively [Kulmala et al., 2012].

[Kulmala et al., 2012] presented two methods to infer GR from observed size distribution data. The methods were compared for a 7-year long data set from the Hyytiälä SMEAR II station by [Yli-Juuti et al., 2011]. These methods agreed with each other within a factor of 2. However, the requirement of the calculations is several hours of growth. Therefore, these methods work especially for regional NPF and not transported events that may have a short growth time.

The methods presented are (a) maximum-concentration and (b) log-normal distribution function methods. For the first method, the diameter is considered the centre of the size bin. For each bin, the considered time is defined when the concentration maximum is reached. A suitable function should be applied to the concentration time series to minimize the measurement noise. For the second method, for each time step, a log-normal distribution should fit the measured number size distribution. Also, for each time step, the geometric mean of the fitted distribution is calculated. The fitting can be done by least-square minimization or other functions. The GR is calculated from the slope of a linear fit to data points that are obtained via the previously presented measurements. The GR can be computed for the entire growth or specific diameter values: <3, 3-7, 7-20, and >20 nm [Kulmala et al., 2012].

1.5.2 Condensation sink

Condensation sink (CS) is defined as the loss term for condensable vapours describing their loss rate by condensation to preexisting aerosol surface. It shows how many molecules are lost to preexisting particles per second [Kulmala et al., 2001]. Therefore, CS is a function of the size distribution and the capacity of the available gases to diffuse and stick on the particles. For these calculations, sulfuric acid was considered the condensable gas which is lost to the particles.

The equation was first introduced by Kulmala et al. [2001]. It was derived considering condensing vapour mass flux to particles in continuum regime and applying the transitional correction factor. The CS equation is proposed as it follows:

$$CS = 2\pi D \sum_i \beta_{m_i} d_{p_i} N_i \ , \tag{6}$$

where D, d_{p_i}, N_i and β_m are the diffusion coefficient in air, particle diameter, number concentration and transitional correction factor, respectively, in the size class i [Kulmala et al., 2001], [Yli-Juuti et al., 2011]. The transitional correction factor was suggested by Fuchs and Sutugin [1971]:

$$\beta_m = \frac{1 + k_n}{1 + 0.377k_n + \frac{4}{3\alpha}k_n + \frac{4}{3\alpha}{k_n}^2}, \tag{7}$$

where k_n is the Knudsen number, defined as:

$$k_n = \frac{2\lambda}{d_p}. \tag{8}$$

The parameters mean free path in air λ, sticking coefficient α and D are specific for sulfuric acid, having the values of $1.21{\cdot}10^{-7}$ m, 1, and 0.0998 cm^2 s^{-1}, respectively. The sticking coefficient α is considered at normal atmospheric conditions of temperature, relative humidity (RH) and pressure equal to 298.15 K, 50%, and 1 atm, respectively [Kulmala et al., 2001]. RH is defined as the percentage of the amount of water in the air in relation to the maximum amount of water vapour that could be held at its current temperature.

1.6 Motivation and broader aim

New particle formation (NPF) is a phenomenon that happens in the atmosphere under diverse environmental conditions, such as Boreal forest (Hyytiälä SMEAR II station, Finland) [Dal Maso et al., 2005], [Dada et al., 2018], rural (Agia Marina, Cyprus) [Dada et al., 2020], urban (Budapest, Hungary) [Nieminen et al., 2018], megacity (Beijing, China)[Matsui et al., 2011]. Because NPF influences the global aerosol particle number, it was investigated via atmospheric observations [Bianchi et al., 2016], chamber experiments [Tröstl et al., 2016a] and theoretical computational studies [Kurtén et al., 2008]. The frequency, location, duration, growth of NPF mainly depend on meteorological conditions, presence of precursor gases and preexisting aerosol particle concentrations [Nieminen et al., 2018], [Lee et al., 2019].

Nieminen et al. [2018] conducted a long-term analysis of NPF in 36 different places of which 16 were rural locations. The results for the rural locations showed a seasonality, with more events during summer compared to winter, and higher growth rates compared to pristine locations. Hence, we considered that studying NPF in Payerne, a rural location in Switzerland, could improve our current understanding of NPF in similar environments.

Our investigation was motivated by the previous normalized particle size distribution measurements done in Payerne. The normalized size distribution is defined as the size distribution of particles in a size bin divided by the width of this bin. The normalized size distribution plots characterized particle sizes down to 15 nm, including UFPs. There were observations of UFPs, so the assumption was the existence of primary UFPs and/or secondary PM related to NPF. The visual analysis revealed several reoccurring features related to NPF events for the year 2020. NPF was reported in previous literature as owning a "banana" shape [Manninen et al., 2010a], [Cheung et al., 2011], therefore being easy to spot from size distributions. The reoccurring features possessed the typical "banana" shape. To exemplify our motivation, there are two possible NPF events presented in Figure 7, on May 27 and 29, around 15 LT (local time - Central European Time (CET)/Central European Summer Time (CEST)) (marked by grey patch) and 12 LT (marked by yellow patch), respectively. These events reoccurred almost once every two days. They were associated with high values in total particle number concentration (∼15,000 cm^{-3}) measured by both Scanning Mobility Particle Sizer (SMPS) and Condensation Particle Counter (CPC) in red and black, respectively. The upper limits of nucleation and Aitken modes, represented by red and gold dashed lines, respectively, enhanced that the NPF events started at the edge of nucleation upper limit and grew into the Aitken mode.

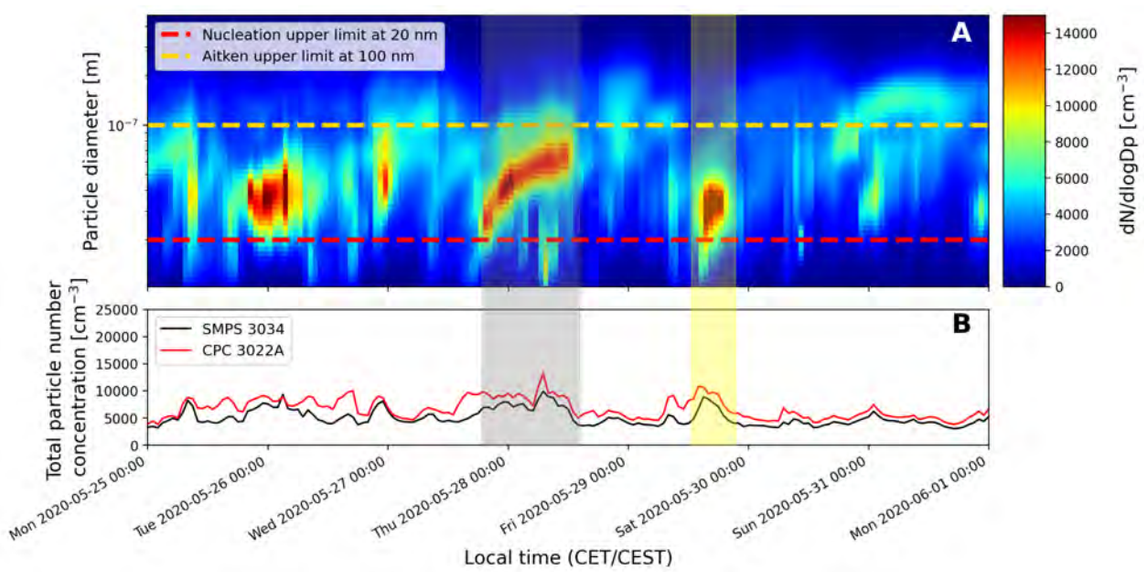

Figure 7: A) Normalized particle size distribution (particle diameter between 10.4 and 469.8 nm) measured in Payerne showing typical NPF "Banana", in which particles grow into Aitken mode particles. The normalized concentration values are in the 0 (blue)–15,000 (red) cm^{-3} range. The upper limits of nucleation and Aitken modes are represented by red and gold dashed lines, respectively. B) Time series for total particle number concentration with values in the range 0–25,000 cm^{-3} for Scanning Mobility Particle Sizer (SMPS) and Condensation Particle Counter (CPC) in red and black, respectively. The grey and yellow patches show two possible NPF events on May 27 and 29, respectively. Data measured in Payerne between May 25 and June 1, 2020.

On the other hand, high number concentration values could also be observed during morning rush hours. Figure 8 depicts both primary UFPs during the morning rush hours (10-11 LT) and a NPF event in the afternoon

for the same day. Primary UFPs remained in the nucleation mode, without further growth, whereas NPF expressed a growth to the Aitken mode.

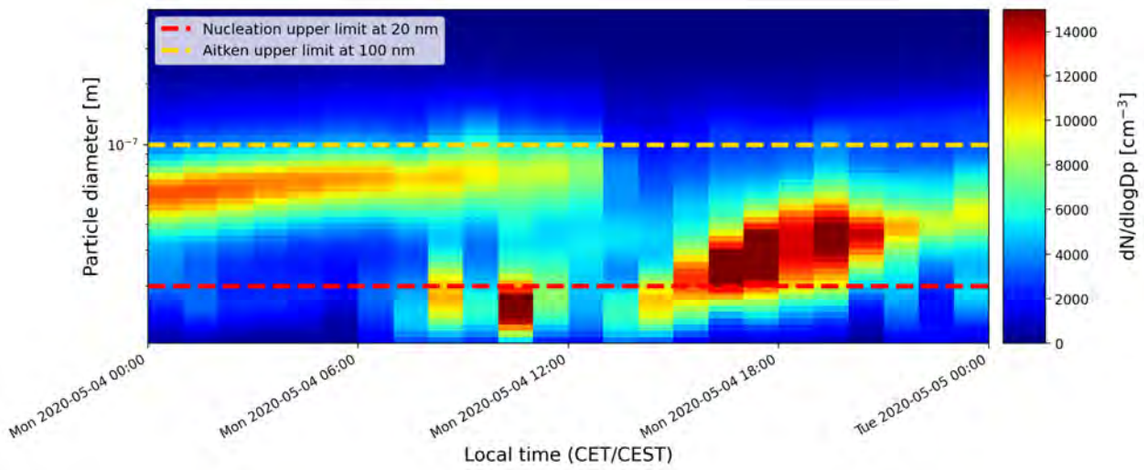

Figure 8: Same as Figure 7, but only normalized particle size distribution showing primary UFPs between 10-11 LT and a typical NPF event during afternoon, when particles grew into Aitken mode particles. Data measured on May 4, 2020.

The primary aim of my thesis was to investigate the abundance and nature of ultrafine particles at the Payerne measurement site, in Switzerland. The objective was centred on differentiating between primary UFPs and secondary PM associated with NPF. For the primary particles, the main focus was to identify the potential sources based on diurnal variability, non-volatile particles and trace gas measurements. Regarding the NPF, I focused on the frequency of occurrence, seasonality, favourable atmospheric conditions and potential origin of particles. Concerning the NPF events, gas-to-particle conversion was studied, which implies semi-volatile particles.

Taking into consideration the motivation mentioned above, the thesis research questions that we are seeking to answer are:

- Are the events seen in the previous measured data primary UFPs or secondary PM associated with NPF?
- Are the sources of primary UFPs from on-road traffic or airport?
- What are the favourable atmospheric conditions, frequency of occurrence and seasonality for NPF?

1.7 Objectives

To tackle the research questions mentioned in section 1.6, this thesis had the following research objectives:

1. Determine the frequency of occurrence of NPF at the Payerne site by using previously and currently collected data.
2. Better characterize nucleation mode size particles between 2.5 and 15 nm at the Payerne site by deploying, operating and maintaining additional instrumentation.
3. Supposing that primary UFPs are mainly non-volatile because of their source (on-road traffic/airport) and NPF mainly volatile due to their production mechanism, use volatile particle number fraction as one of the observation parameters to distinguish primary UFPs from NPF. The volatility data is obtained using a switchable catalytic volatile particle remover. When the catalytic volatile particle remover is switched on, the particles are heated to 350°C, thus only the non-volatile particles will remain.
4. Evaluate the potential sources of primary UFPs by considering normalized non-volatile particle size distribution, trace gas concentration and parameters measurements, e.g. eBC. To assess the frequency, duration, growth rate and seasonality of NPF, analyse favourable conditions and precursor gases for the NPF by taking into account local meteorological data such as solar radiation, temperature, RH, precipitation, wind speed, and wind direction, and trace gas concentration, such as H_2SO_4 proxy.

2 Field site and methods

2.1 Payerne research station

The Laboratory of Atmospheric Chemistry at the Paul Scherrer Institute (PSI) is operating multiple aerosol research stations, one of them being a simple monitoring station in Payerne. It has now been running for over one year. The long-term goal of the Payerne station is to complement the existing aerosol monitoring infrastructure from the Federal Office of Meteorology and Climatology (MeteoSwiss) and the Swiss Federal Laboratories for Materials Science and Technology (Empa). Payerne is a rural station of the National Air Pollution Monitoring Network (NABEL). In addition, the site can become part of the European Aerosols, Clouds, and Trace gases Research Infrastructure Network (ACTRIS) in the future. ACTRIS' role is to foster new knowledge as well as guide policy issues related to climate change, air quality, and long-range transport of air pollutants.

The study site is in Payerne, canton of Vaud, Switzerland. Payerne is located at 456 m above sea level. The city area is 24.19 km^2 (square kilometre), with a population of around 10,000 inhabitants [Ville de Payerne, 2020]. The station is located at around 500 m north to the main road and about 4 km south to the highway and Payerne military airport (Figure 9a). For the moment, the station is placed in a container next to the MeteoSwiss infrastructure, as is presented in Figure 9b.

The last report published by NABEL presented the relative contribution of the main fine aerosol components for the five sites of the 2018–2019 measurement period, including Payerne. Compared to the other urban and suburban stations, Payerne exhibited the lowest aerosol mass concentration, being considered a station with a low pollution level [Hüglin et al.].

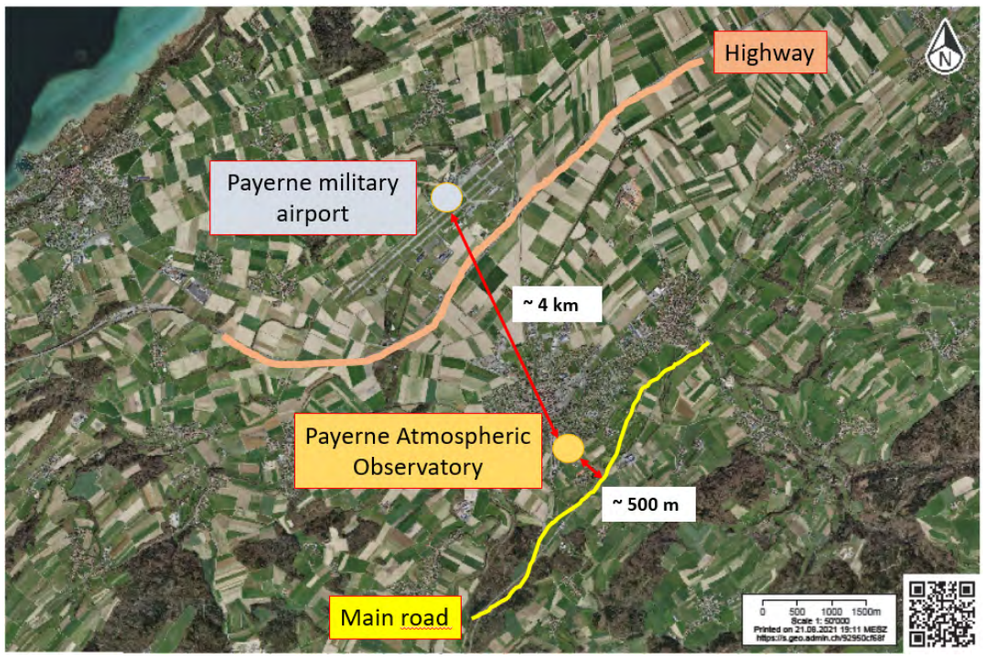

(a)

(b)

Figure 9: (a) Location of the Payerne aerosol monitoring station. The distance to the main road is around 500 m (to the south) and to the highway and Payerne military airport (to the north) is around 4 km [Swiss Confederation, 2021]. (b) Measurement station exterior (Figure courtesy of Dr. Benjamin Tobias Brem, Laboratory of Atmospheric Chemistry, Paul Scherrer Institute).

2.2 Instrumentation

For the aerosol characterization, the station is equipped with the instruments presented in Figure 10: Neutral cluster and Air Ion Spectrometer (NAIS Airel), two Scanning Mobility Particle Sizers (SMPS TSI Incorporated (TSI) 3034 , SMPS TSI 3938) and two Condensation Particle Counters (CPC TSI 3022A, CPC TSI 3775).

SMPS 3034 (SMPS) and CPC 3022A (CPC) were already installed in Payerne for long-term monitoring since 2019. They have been measuring data for more than one year. Both of them were connected to a PM_{10} inlet. PM_{10} refers to PM with the aerodynamic diameter equal to or smaller than 10 µm. SMPS has a time resolution of 3 minutes for each normalized size distribution. It measures atmospheric particles in the range of 10–469 nm [TSI Incorporated, 2020]. CPC measures total particle number concentration for particles down to 7 nm every 1 s, but it does not provide any particle size information [TSI Incorporated, 2002]. Therefore, both SMPS and CPC data will be used as a reference for the NAIS and to identify previous NPF events.

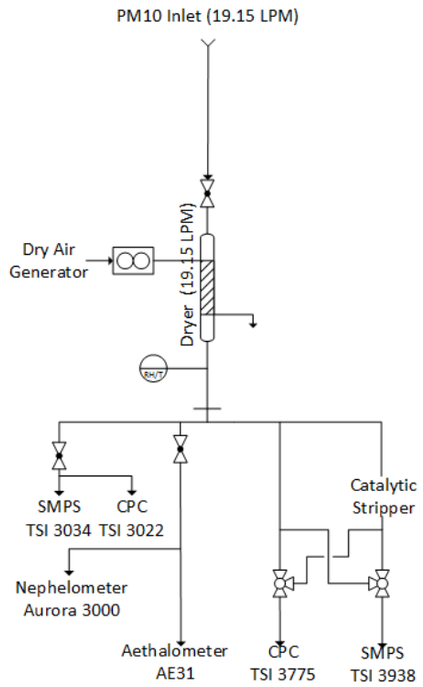

Figure 10: Instrumentation setup in Payerne (Figure courtesy of Dr. Benjamin Tobias Brem, Laboratory of Atmospheric Chemistry, Paul Scherrer Institute).

A second SMPS (SMPS 3938 - nanoSMPS) and CPC (CPC 3775) were installed in October 2020 to provide information about the volatility of atmospheric particles. NanoSMPS was set to measure the size distribution in the range of 3–110 nm in one minute [TSI Incorporated, 2014]. It was currently using a butanol based CPC (CPC 3776). The CPC 3775 measured down to 4 nm, and it was also butanol based [TSI Incorporated, 2007]. A switchable catalytic stripper was placed in front of SMPS to evaporate the volatile particles and CPC 3775 was in parallel with the SMPS. The catalytic stripper was a CS015 model, with an operating gas temperature of 350°C [Catalytic Instruments, 2020].

In Table 1 are presented the instruments used for analysing primary UFPs and NPF events. Moreover, the institution which provided the meteorological and trace-gas data are listed. The studied parameters are marked together with their time resolutions. The block average records mentioned below represents one average record from start to finish of each element in the measurement cycle [Airel, 2015].

The NAIS was installed in Payerne in October 2020. It was in operation until the end of May. It had a separate inlet to minimize the losses. Once per month, we had to go to the site to check the flow of the instruments, replace consumables (for CPCs) and perform size calibrations (for SMPSs), which represented a part of the second research objective.

Table 1: The instruments used to examine primary UFPs and nucleation PM associated with NPF [Airel, 2015], [TSI Incorporated, 2002], [TSI Incorporated, 2003], [TSI Incorporated, 2007].

Parameters	Instrument	Notes
Particle size distribution 2.47-14.47 nm	NAIS	Block average records
Particle size distribution 14.9-469.8 nm	3034 SMPS; 3022A CPC	Time resolution: 3 min; 1 s
[a]Positive ion size distribution 0.8-40 nm	NAIS	Block average records
[b]Negative ion size distribution 0.8-40 nm	NAIS	Block average records
Volatile particle number fraction information	3938 SMPS; 3775 CPC	Time resolution: 1 min; 1 s
NO_2, NO_x, SO_2	NABEL	Time resolution: 1 hour
Temperature, solar radiation, dew point	MeteoSwiss	Time resolution: 10 min
Precipitation, wind direction, wind speed	MeteoSwiss	Time resolution: 10 min
equivalent black carbon	Aethalometer	Time resolution: 1 hour

[a]Positive/ [b]Negative ions are molecules or atoms that lost/gained one or more electrons, respectively.

2.2.1 Neutral cluster and Air Ion Spectrometer (NAIS)

Neutral cluster and Air Ion Spectrometer (NAIS) is the main instrument that provided the data regarding the nucleation mode particle events. It is a multichannel instrument that measures the normalized number size distribution of the atmospheric ions and particles. Ions are defined as naturally electrically charged molecules or atoms in the atmosphere. Atmospheric particles are defined as neutral molecules or atoms. The ions' size range is 0.8-40 nm, whereas the particles' is between 2-40 nm. The measurements time resolution is one-second [Airel, 2015].

The instrument has an aerosol processing unit with electric filters and an aerosol detection unit. As is shown in the schematic picture of NAIS presented in Figure 11, the processing unit is made of unipolar corona chargers (one charger and one discharger for each spectrometer channel) and electric filters (one filter and one postfilter for each spectrometer channel). For the detection unit, NAIS provides four operating modes: ion mode, particle mode, alternating charging mode and offset mode:

- The ion mode measures naturally charged particles (ions). For this mode, all parts of the preconditioning unit are switched off and there is no modification made on the aerosol sample.
- For the particle mode, the main charger and postfilter are switched on, while the discharger and filter are switched off. The instrument measures all particles including the uncharged ones which are charged by the main charger. Then the excess of charger ions is removed by the postfilter.
- The alternating charging mode has the discharger, main charger and postfilter switched on and the filter off. The mode is used to neutralize the sample to improve its performance in the case of a non-steady-state charge distribution.
- The offset mode measures the zero signal and the noise levels of electrometers. For this, the discharger and filter are switched on, so the particles are charged by the discharger with ions of opposite polarity and then are filtered out. Its purpose is to have no induced currents in the analysers.

The aerosol detection unit has two Differential Mobility Analysers (DMAs) that separate the charged particles (charged by the main charger) and ions according to their mobility. Because there are two parallel DMA, NAIS measures simultaneously positively and negatively charged particles and ions. Each DMA has 25 electrometers that can detect charged particles at different mobilities [Manninen et al., 2016], [Wagner et al., 2016].

A schematic of the DMA is presented in Figure 12. It is made of cylindrical electrodes, with the central one having several sections, each of them at a different fixed electric potential. The charged aerosol is sucked into a circular slit near the central electrode. The clean sheath air is introduced near the outer electrode. The charged particles travel in the analyser. If the particles possess the same electrical polarity as the central electrode, then they are deposited on the outer electrodes by a radial electric field. The deposited particles pass their charge to the amplifiers. The outer electrodes are connected to electrometric amplifiers at near ground potential, and they are

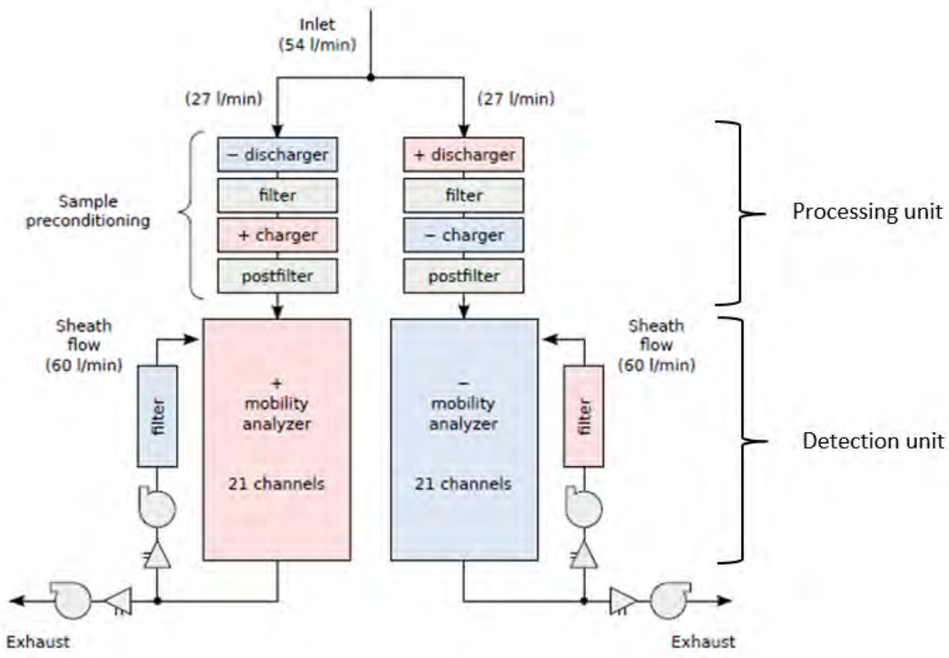

Figure 11: NAIS principal schematic for the 4 pump version [Airel, 2015].

further connected to the data acquisition system [Airel, 2015], [Mirme and Mirme, 2013].

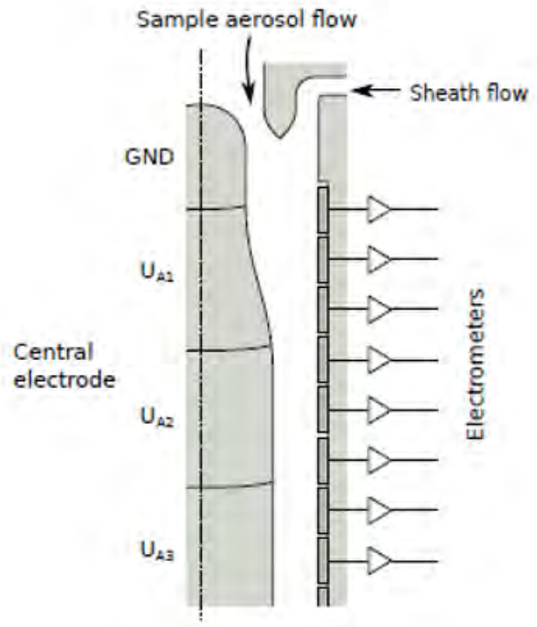

Figure 12: Working principle of the mobility analyser [Airel, 2015].

2.2.2 Scanning Mobility Particle Sizer (SMPS)

The Scanning Mobility Particle Sizer (SMPS) measures the normalized size distribution of polydisperse aerosols. The measurements are based on classifying the charged particles in an electric field by their electrical mobility and then counting them. Multi-charge correction is applied to convert to normalized size distribution in terms of diameter. SMPS's components are an electrostatic classifier, a DMA and a CPC.

The electrostatic classifier has a radioactive source (Kr-85 bipolar charger) and two laminar flows for sheath and aerosols. The radioactive source neutralizes the incoming aerosol particles and applies a stationary-state charge distribution on the particles. The DMA is made of two concentric cylinders, with the negatively charged rod at the centre and its working principle is shown in Figure 14a. The charged particles travel through the sheath air and are

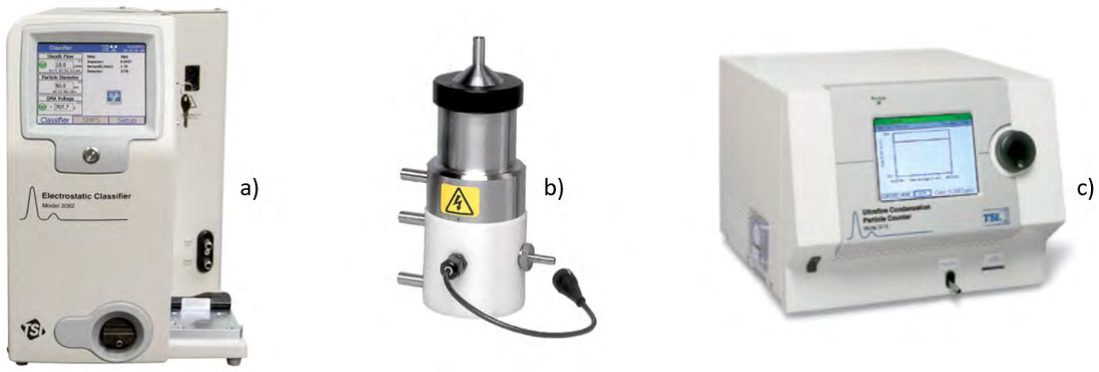

Figure 13: SMPS components: a) electrostatic classifier, b) differential mobility analyser, c) condensation particle counter [Weingartner, 2020].

attracted to the charged rod. At a certain voltage, only particles with the corresponding electrical mobility leave the DMA as a monodisperse aerosol distribution. The aerosols are counted with the CPC (working principle shown in Figure 14b). Each scan is done for a different voltage, so the full distribution is obtained. After entering the CPC, the particles go through a wick and grow by heterogeneous condensation (water or butanol based). The particles pass through a light beam and scatter the light on a photodetector. The electrical pulses are counted using the efficiency curve [Weingartner, 2020], [TSI Incorporated, 2014]. Figure 15 shows the SMPS schematic.

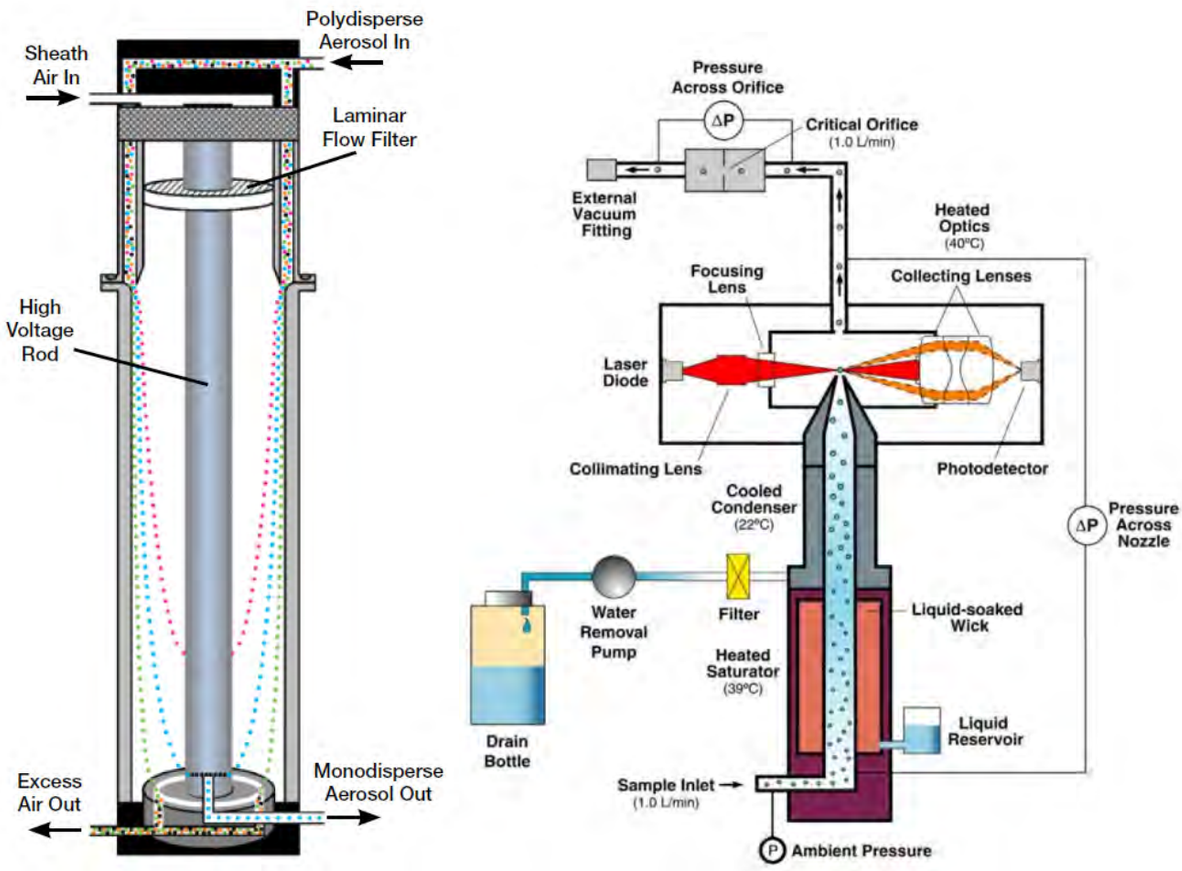

(a) (b)

Figure 14: (a) DMA working principle [Emanuelsson, 2013]. (b) CPC working principle [Kuang, 2016].

2.2.3 Condensation particle counter (CPC) and nanoSMPS with a switchable catalytic volatile particle remover

To detect potentially existing non-volatile nucleation mode particles in UFPs, we used a CPC with a switchable catalytic volatile particle remover. During five minutes, the catalytic stripper had the valve open and the particles are heated at 350 °C. Thus, only the non-volatile particles remained. The non-volatile particles are assumed to consist of refractory black carbon (rBC) from incomplete combustion of on-road vehicles and gas-turbine aeroplanes. rBC is an aerosol component, released from various incomplete combustion processes [Wang et al., 2018].

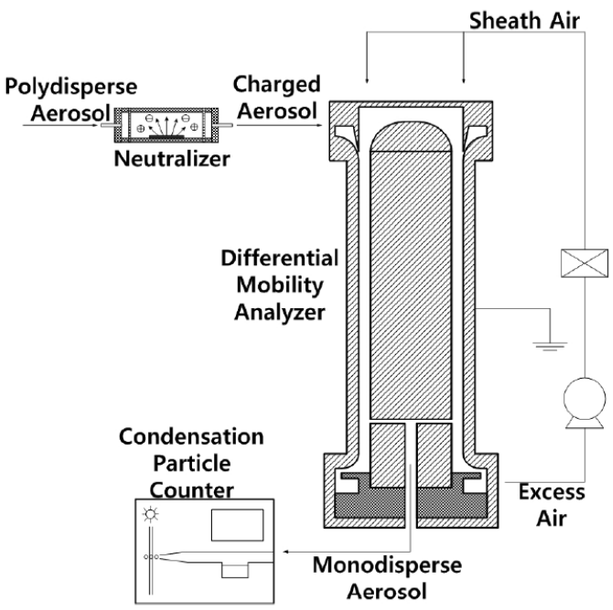

Figure 15: SMPS working principle scheme [Kim et al., 2009]

The volatile fraction of the particles is related to secondary compounds and gas-to-particle conversion, and also to primary condensable material (section 1.1.2).

Because of valve failures from March 18, 2021, to the end of the measurements campaign, the valve was always open, measuring only the non-volatile particles. The concentration of volatile particles was measured as a difference between total particle number (CPC) and the number of non-volatile particles (CPC 3775).

Because the SMPS 3938 (nanoSMPS) had different malfunctioning periods, it was disconnected from the installation arrangement on March 17, 2021. The data from nanoSMPS provided volatility information for each bin between 3-110 nm, with a time resolution of 1 min.

The periods when the instruments had shown malfunctions were: February 22, 2021 - March 12, 2021; April 21, 2021 - May 5, 2021; May 23, 2021 - May 25, 2021.

2.3 Laboratory and field-related work

For reliable measurements from NAIS, we checked that the instrument was fulfilling the conditions presented in [Airel, 2015]. We checked the flow rate with a flow calibrator (Mini-BUCK Calibrator M-5) [A. P. BUCK, 2017]). Moreover, we ran NAIS indoor in the laboratory, and we diagnosed it based on the diagnostic checklist presented in the manufacturer's manual. We compared the discharger and charger current values for ions, particles and offset modes. We found that the positive main charger was fluctuating and that the charger had to be cleaned and replaced.

2.4 Data treatment

The objectives of the thesis mentioned in section 1.7 are presented in two flowcharts. The first one is shown in Figure 16 and the last three objectives in Figure 19. The latter three objectives are presented in a common flowchart because they co-depended.

To determine the occurrence of NPF at the Payerne site, we used existing aerosol normalized size distributions and total particle number concentration for the entire year 2020 from SMPS and CPC data. The SMPS data was evaluated and inverted by using the aerosol instrument manager software provided by TSI Instruments. The SMPS data was corrected for sampling losses, diffusion losses being of particular importance for UFPs, and for instrument losses due to penetration efficiency. The SMPS and CPC data for the entire period was included in joint data files and average to a common time base in the range of 10 minutes. We did normalized size distributions plots for SMPS and total particle number concentration time series for both SMPS and CPC. We evaluated the normalized size distributions visually by checking for the "banana" shape and thus counting the NPF event. Therefore, we

analysed the frequency of occurrence of NPF events.

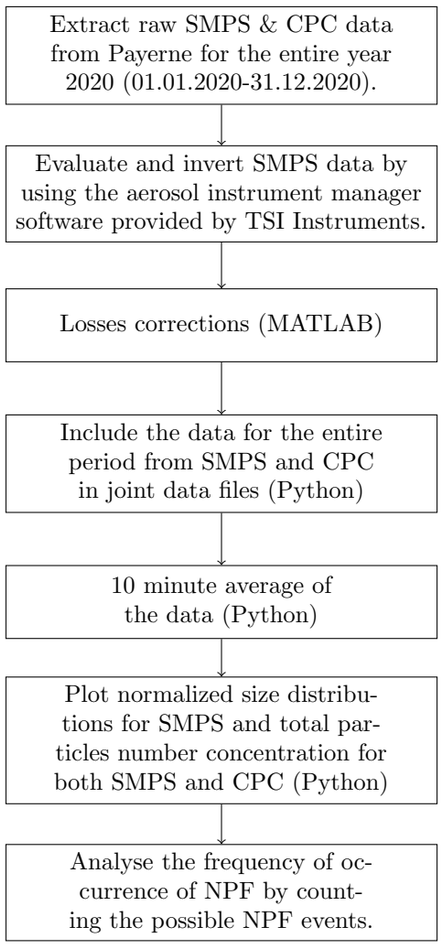

Figure 16: Flow chart for the first objective.

To better characterize nucleation mode size particles between 2.5 and 15 nm, we used additional instrumentation, NAIS, besides SMPS and CPC. The time interval for the analysis was between October 12, 2020, and May 31, 2021. The data covered three seasons (autumn, winter and spring) because long-term measurements are required for a better understanding of NPF events [Hari and Kulmala, 2005], [Manninen, 2011]. For both NAIS and SMPS, we applied an empirical correction for size-dependent losses, sampling losses mainly due diffusion and instrument losses due penetration efficiency. The data provided by NAIS was in block average records, one average record from start to finish of each element in the measurement cycle. After, the NAIS data was merged to create daily data. The normalized size distribution (provided by NAIS, SMPS data) and total particle concentration (provided by CPC and SMPS data) data was merged in one data file and averaged to a common time base in the range of 10 minutes. Because NAIS overestimates the measured normalized size distribution for negative particles by a factor of 2-3 [Gonser et al., 2014], we corrected it by dividing the values by 3. Negative particles are neutral particles that are negatively charged using the NAIS instrument.

The normalized size distributions for both negative particles and positive and negative ions were plotted and classified into different NPF events based on [Dada et al., 2018]. The classification was the following: regional events, transported events, ion burst events and non-events, as is shown in Figure 18.

For the classification, we implemented thresholds. NPF events can be grouped into different classes: I, II and III. We further exemplify the class I NPF event by a "show-case". Figure 17 illustrates the normalized size distribution for A) NAIS negative particles (<14.46 nm) combined with SMPS particles (>14.9 nm), B) negative ions and C) positive ions on April 11, 2021. Also, time series for A) geometric mean diameter (< and > 19.8 nm in the black and green line, respectively) is plotted. Data between 12 and 18 LT (marked by the grey patch) is representative of the class I NPF event. We started by looking at the concentrations of negative ions. The values were greater than 6000 cm^{-3} for more than 10 minutes. By looking at negative particles concentrations, we saw concentrations greater than 2500 cm^{-3} lasting more than 30 minutes. Because of the mentioned findings, this day was classified as a class I NPF event.

Based on similar approach as in Figure 17, we did the classification presented in Figure 18. The classification

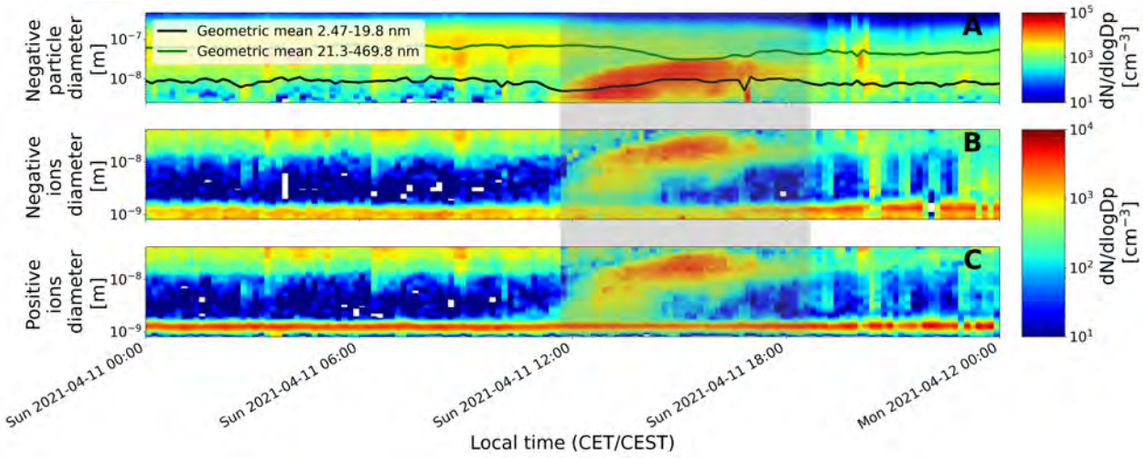

Figure 17: Normalized size distribution for A) NAIS negative particles (<14.46 nm) combined with SMPS particles (>14.9 nm), B) negative ions, C) positive ions. Time series for A) geometric mean diameter (< and > 19.8 nm in black and green, respectively). Data is representative for class I NPF (marked by grey patch). Measurements conducted on April 11, 2021..

scheme was originally developed for Boreal forest data. Because our measurement site has different conditions, we used specific values for the classification, which were obtained by analysing several NPF events and understanding the necessary threshold. For the classification, we needed to ask several questions. The first question was if there were NAIS negative ions with total concentrations greater than 6000 cm^{-3} that persist at least 10 minutes. The second question implied if there were NAIS negative particles with at least 10 consecutive sizes with concentrations greater than 2500 cm^{-3} for more than half an hour. If the answers were confirmed positive for both of the questions, there was a regional event. If there were ions, but no particles, then it was labelled as an ion burst. If there were no ions, but particles, it is a transported event or Class III event. If the answers were found negative for both of them, it was classified as a non-event. The regional events were further classified in Class I and Class II. For Class I, both the nucleation mode particles and growth are seen. The growth of the particles was observed in the normalized size distribution, started also in the ion mode. Class II events or bump events are similar to Class I events, but the growth was not observed. Transported or Class III events covered particles carried horizontally or vertically to the measurement site. Compared to [Dada et al., 2018], the thresholds for our measurement site were greater for total particle number concentration and lower for persistence time.

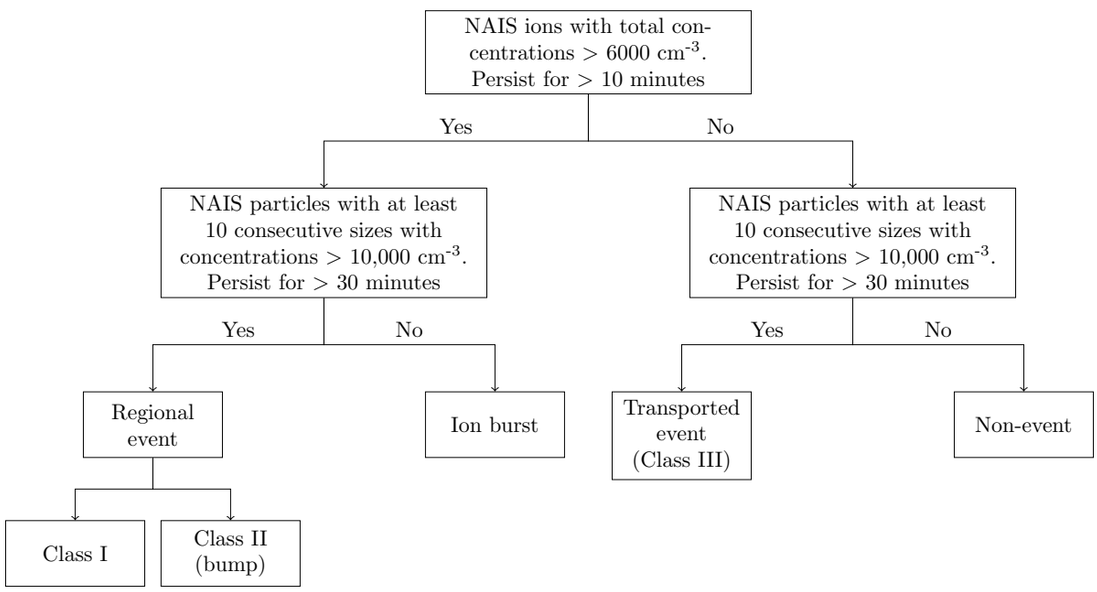

Figure 18: Flowchart for the event classification in Payerne based on [Dada et al., 2018].

Geometric mean diameter was calculated for the nucleation mode for particles with the diameter between 2.47-19.8 nm. We further used the geometric mean diameter and maximum concentration method to calculate the growth rate (GR).

Based on volatile particle number fraction, equivalent black carbon and diurnal variability of nucleation and Aitken modes, we distinguished between primary UFPs and secondary PM. Regarding secondary PM related to

NPF, we analysed the meteorological data (solar radiation, temperature, dew point used for calculating RH, wind direction, wind speed, precipitation) and trace gas concentration data (SO_2 to further calculate sulfuric acid proxy) to understand the favourable conditions and precursor gases for the NPF events. Condensation sink (CS) was also calculated as it was previously described in section 1.5.2.

The potential sources of primary UFPs were evaluated by considering normalized non-volatile particle size distribution obtained from the nanoSMPS, trace gas concentration and other parameters measurements, e.g. eBC, volatile particle number fraction. Usually, the gas turbine particles maximum aerodynamic diameter is between 1 and 20-30 nm [Allouis et al., 2010]. By plotting normalized size distribution and time series of the non-volatile particles in the nucleation mode size range, we could observe if gas turbines from the aeroplanes were one of the sources. On the other hand, the non-volatile UFPs in the Aitken mode size range were associated with on-road traffic emission as a source.

Since the 18^{th} of March 2021, the nano SMPS did not function properly and was disconnected from the setup. The catalytic stripper was connected permanently to the CPC 3775. For the new setup, the value of volatile particles was calculated from the difference between the data measured by CPC (measuring both volatile and non-volatile particles) and CPC 3775.

To analyse the role played by ambient conditions, as was presented in the fourth objective, local meteorological and trace gas concentration data will be accessed through the MeteoSwiss CLIMAP service. Laboratory of Atmospheric Chemistry (LAC) from PSI has a licence. For specific variables, such as wind condition at the height of the sampling inlets, we checked data from our colleagues at MeteoSwiss. Trace gas data was provided by NABEL/Empa.

Meteorological data with a 10-minute time resolution and trace gas and eBC data with a 1-hour time resolution is presented in Table 2 and Table 3, respectively.

Table 2: Meteorological parameters data.

Meteorological parameters	Units
Air temperature 2 m above ground	°C
Precipitation	mm
Global radiation	W/m^2
Pressure at station level (QFE)	hPa
Wind direction	°
Wind speed	m/s
Dew point 2 m above ground	°C

Table 3: Trace gases and eBC concentration data.

Trace gas and eBC parameters	Units
NO_x, SO_2	$\mu g/m^3$
equivalent black carbon concentration at 950 nm	ng/m^3

NAIS instrument is provided with a software package that contains two programs, Spectops and Retrospect. Spectops is for running the measurements and viewing the live data, whereas Retrospect is for viewing and reprocessing collected data [Airel, 2015]. The Retrospect software was used for data processing, as seen in Figure 20. We chose the "block averaging period" option to record the output as one average record during one measurement cycle for each element.

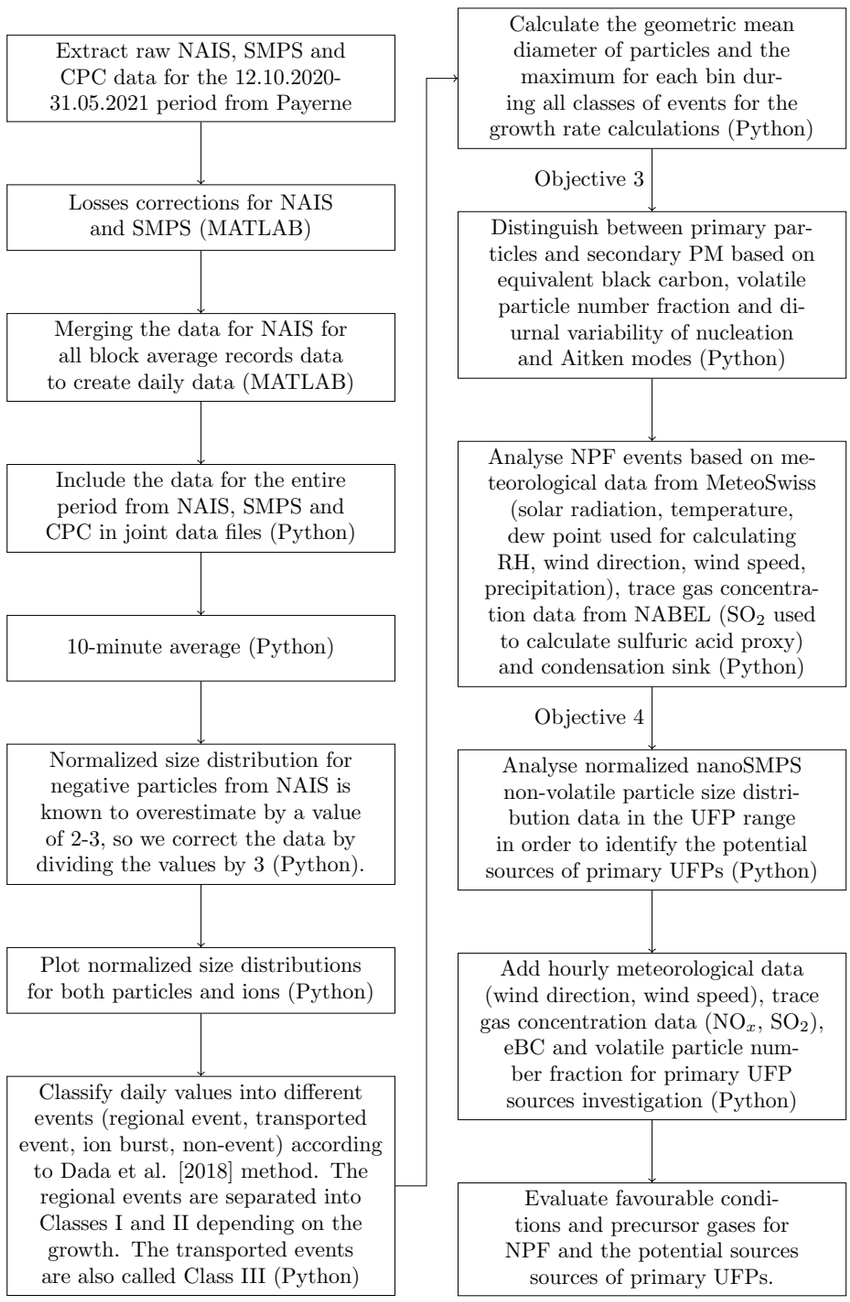

Figure 19: Flow chart for data treatment.

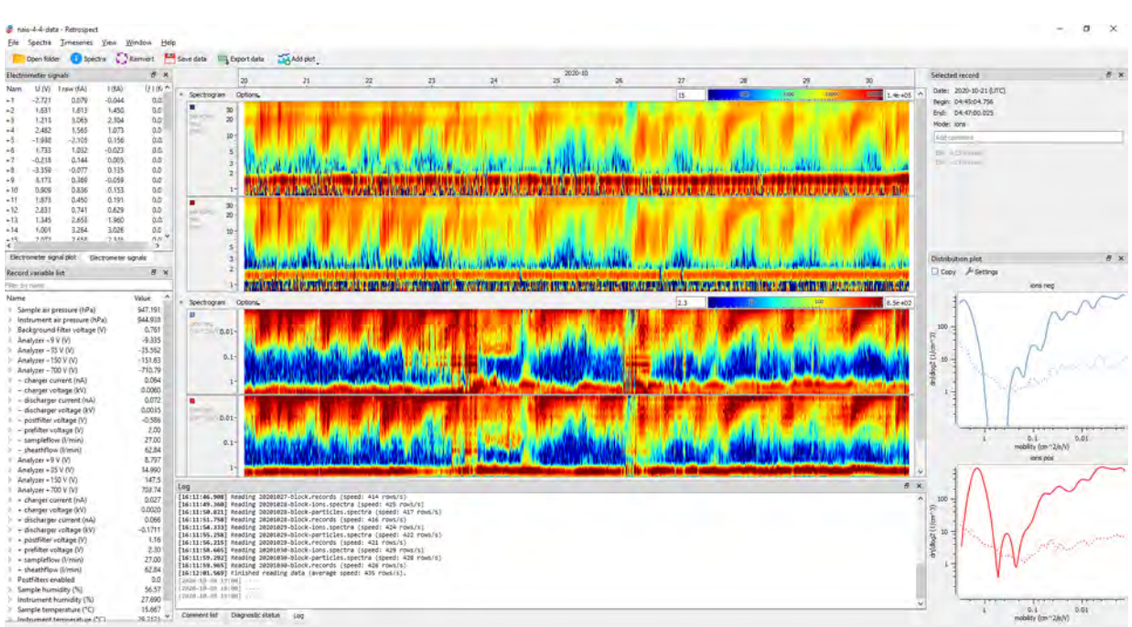

Figure 20: NAIS Retrospect software [Airel, 2015].

3 Results and discussion

3.1 Identification of NPF using existing normalized size distribution data set

We analysed the normalized size distribution data to identify periods when NPF was detected. When the UFPs temporal evolution showed the typical banana shape, we attributed this to a NPF event. Initially, we started the analysis with previous data collected for the year 2020. Based on the normalized size distributions, we visually investigated the existence of NPF events. We focused only on the frequency of the NPF events rather than focus on the primary particles because it was visually easier to detect. NPF usually possess the specific form of a banana, with a high concentration for small particles (< 20 nm) that decreases with time.

To visually inspect the number of NPF events, we looked at periods with concentrations greater than 10,000 cm^{-3} that lasted more than 30 minutes. Because the NPF mainly occurs during time periods with high solar radiation, usually noontime [Manninen et al., 2010b], we took into account the high concentrations during noon-afternoon. Between January and December 2020, the number of NPF events were around 60. The value of 60 was counted without including the supposed NPF events that occurred when the instrument was broken, e.g. months of July and August. Figures 21a, 21b, and 21c show the normalized size distributions and total particle number concentrations for the months February, March and November, respectively. These months were chosen as an example because they show better the frequency of NPF events, the data covered the entire month, and the instrumentation functioned properly. The plots are the same as Figure 7, but for (a) February, (b) March and (c) November, 2020. Total particle number concentration was measured using both Scanning Mobility Particle Sizer (SMPS) and Condensation Particle Counter (CPC) and it is shown in red and black lines, respectively. The SMPS total particle number concentration is the integral over all size bins in the range of 10.4-469.8 nm. Strong nucleation mode particle events reoccur almost every day at the same early morning hours. White arrows point out the possible NPF events.

Understanding true NPF events was ambiguous by measuring the nucleation mode particle diameter with the SMPS device only. In some cases, we did a visual inspection from monthly to daily data. For Figure 21b previously shown, the first step was a 10-minute average for the entire month of March. The average data helped us understand where the possible weeks and days with NPF events were. Due to period with concentration values higher than 10,000 cm^{-3} that lasted more compared to other days' high concentration, e.g. March 13 compared to March 1, we concluded that a possible strong NPF event around March 13 was recorded, so we continued to shrink the plotting interval, between March 9 and 16, 2020, and March 13 and 16, 2020, as plotted in Figure 22a and 22b, respectively. We plotted the same as the monthly plots, but for a shorter interval.

We observed the "banana" shape for the data starting on March 13 and ending on 14 (marked by the black dashed rectangle in Figure 22a). The NPF event started with a sharp appearance of nucleation mode particles with a diameter of about 20 nm. The absence of sub-10 nm particles at the start of the event suggests that the nucleation could have occurred in another area and afterwards particles were transported to the measurement site. Afterwards, the particles underwent continuous growth until their diameter reached around 100 nm and concentrations of 6,000 cm^{-3}. On March 14, around 7 LT, there is the possibility of primary UFP sources, marked by the white arrow. This is an example in which the NPF event directly leads all the way to potential CCN, given that typical CCN activation threshold diameters are in the range of around 87 nm for supersaturation of about 0.35% [Hammer et al., 2014].

We estimated the end of the event on March 14, at noontime. We initially observed a long tail between the afternoons of March 14 and 15, but it belongs to a separate plume. On March 14 at around 16 LT, there was a new source for particles with diameters around 50 nm and a concentration of 15,000 cm^{-3}. Therefore, the NPF event occurred between March 13, noontime, and March 14, noontime.

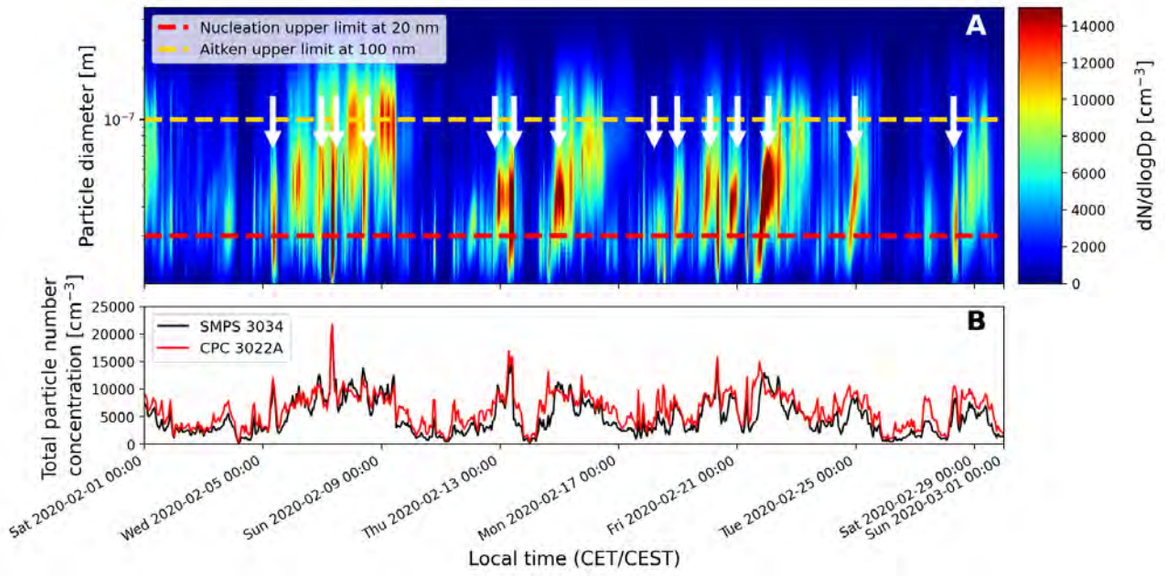

(a)

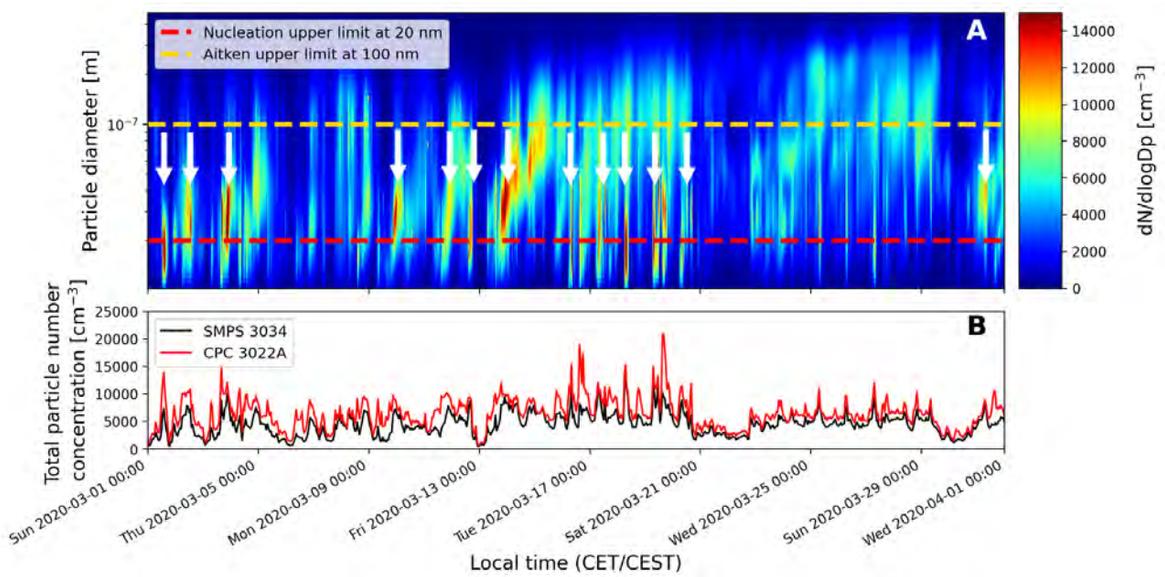

(b)

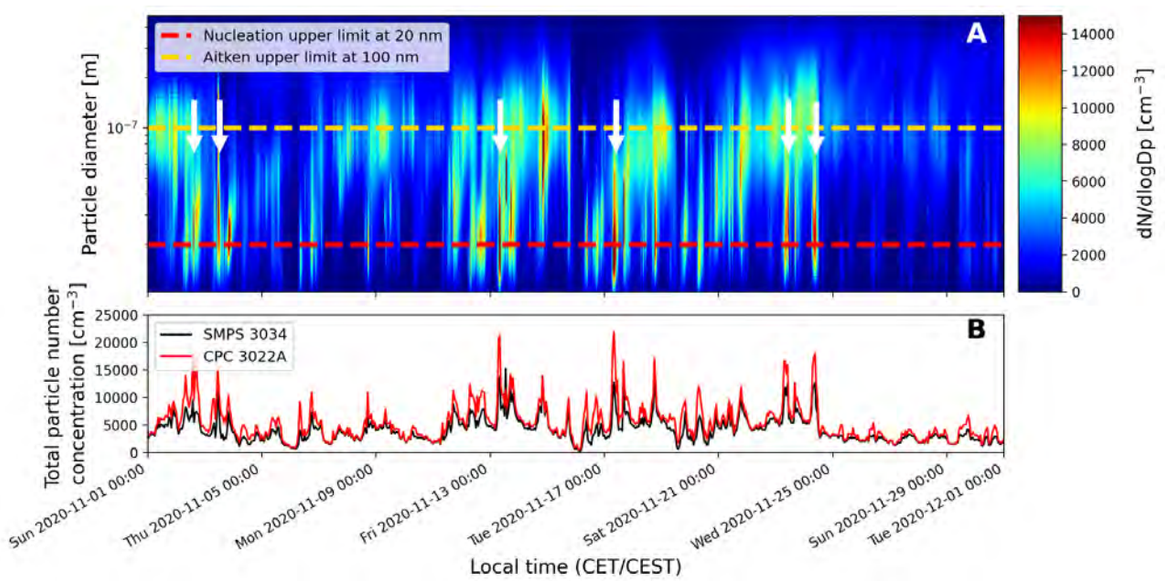

(c)

Figure 21: Same as Figure 7, but for (a) February, (b) March and (c) November, 2020. Strong nucleation mode particle events reoccur almost every day at the same early morning hours. White arrows point out the possible NPF events.

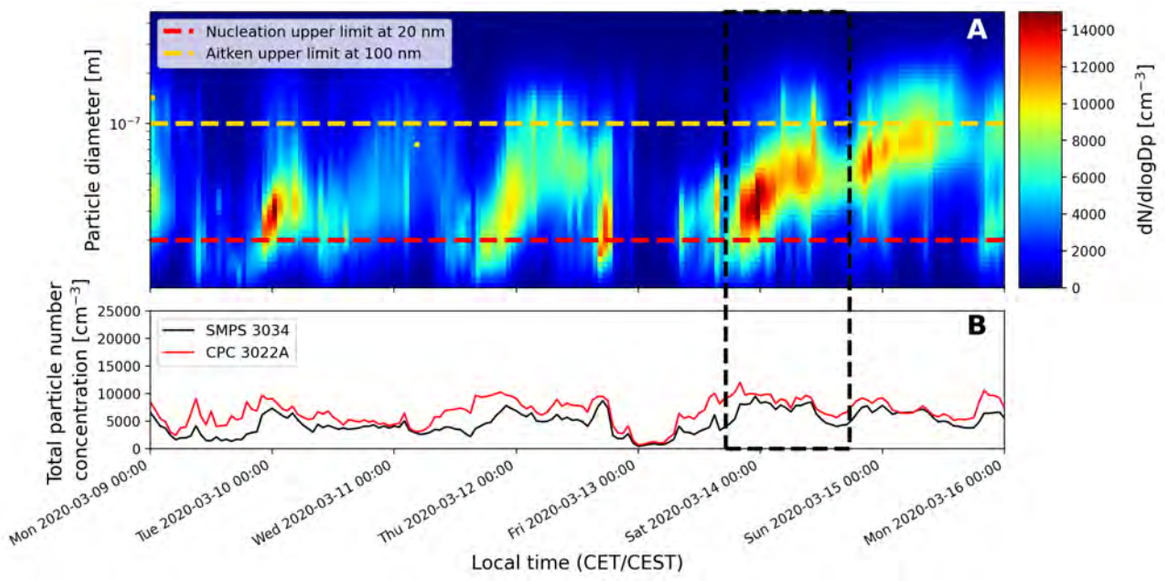

(a)

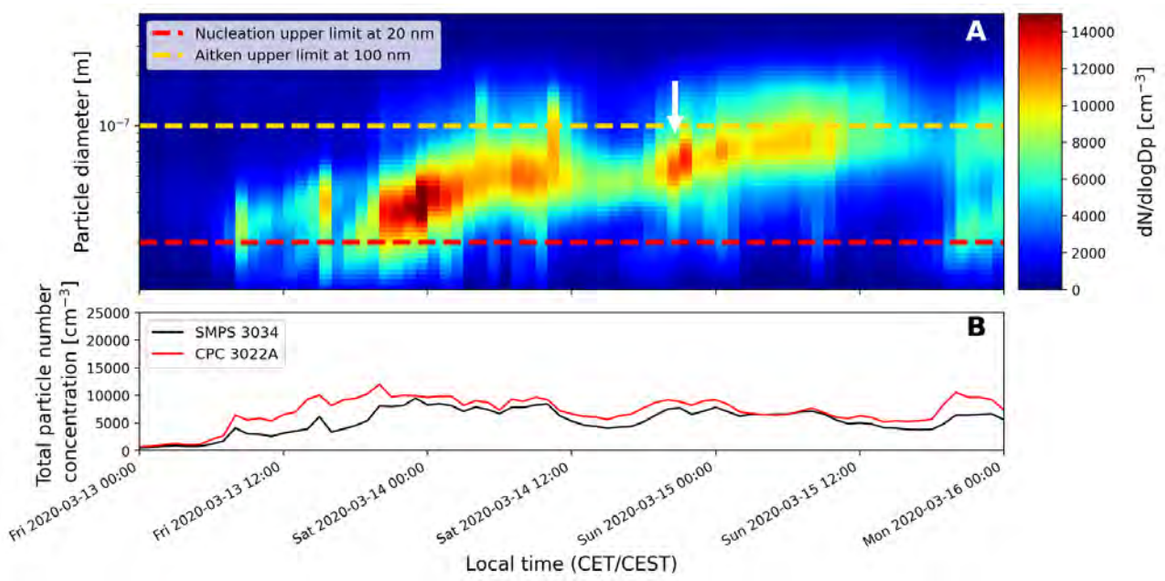

(b)

Figure 22: Same as Figure 7, but for presenting the period from (a) March 9 to 16, 2020, and (b) March 13 to 16, 2020, respectively. Black dashed rectangle in Figure a) underlies the plausible NPF event. White arrow in Figure b) shows a possible primary UFP source.

3.2 Distinction of primary ultrafine particles and secondary particulate matter

We started the distinction between primary UFPs and secondary PM by analyzing the seasonal and diurnal variability. Because primary UFPs were mainly associated with direct emissions of incomplete combustion of fossil fuels and gas-turbine engines coming from the road and airport, we expected to find them during rush hours for all seasons and related to high eBC concentrations. On the other hand, secondary PM related to NPF were supposed to be found during periods with higher solar radiation, therefore during noontime. Also, because of this assumed favourable meteorological condition, the warmer season was seen more prone to NPF.

3.2.1 Seasonal variability of ultrafine particles

The seasonality pattern of nucleation and Aitken particle modes can provide information about the frequency of occurrence of UFPs within these two modes. For the analysis of the number concentration, we used box plots. The data is between October 2020 - May 2021, therefore it does not cover an entire year.

Figures 23a and 23b show the seasonal frequency of particle number concentration of a) nucleation and b) Aitken modes, respectively, presented by box plots. For nucleation mode particles, we did the graph using raw data from the NAIS instrument only, with a 5-minute resolution, because the 10-minute average values were 1.5 times higher. Therefore, the values were between 2.47-14.46 nm. By comparing the spread of medians (central red marks) with typical interquartile range (IQR) within a month, only weak seasonality was observed compared to intra - month variability. The median value of most months fell within the IQR of e.g. March.

Similar to nucleation mode, Aitken mode seasonality was investigated using raw data from the SMPS instrument, with a 3-minute resolution. There was a similar pattern for the particle number concentration within the Aitken mode (Figure 23b). The Aitken mode IQR is similar to the nucleation mode one. This demonstrates that sources of particles within these size ranges were a priori not different. The strong covariance of particle number concentrations within these two modes shows that Banana-Type NPF events could be the dominant contribution. The aerosol number concentration values for nucleation mode is around twice as high as the Aitken mode ones, subject that will be deeper analysed in section 3.2.3.

The outliers seen in both nucleation and Aitken modes had two different potential sources: local plumes or instrument problems. We checked the raw data and we concluded that there single-source plumes which produce high outliers. However, despite their high number concentration values, they represent around 2% of the total monthly values.

3.2.2 Diurnal variability of volatile particle number fraction and eBC

Particulate matter properties, such as volatility and equivalent BC (eBC), were used to differentiate between primary and secondary nucleation mode atmospheric particles. Our expected output is a distinct volatile particle number fraction pattern for primary and secondary UFPs, as we previously mentioned in section 1.1.6.

Figure 24 shows the hourly variations of volatile particle number fraction values between December 2020 and May 2021, using the methodology described in section 2.2.3. The data is shown in local time (LT) (Central European Time (CET)/Central European Summer Time (CEST)) and is between 0 and 1. 0 represents the least volatile particle number fraction and 1 that all particles were volatile.

The hourly variations of volatile particle number fraction values were in the range of 0.6-0.9 for the entire period. There was a segregation of spring (March, April, May) and winter (January, February, December) values, respectively. Volatile particle number fraction during winter months was quite high (0.7-0.8), thus not dominated by non-volatile primary UFPs, such as BC. The proportions of volatile particle number fractions in background aerosol (during night-time) and “fresh UFPs” (primary UFPs and NPF related) were quite similar, except for summer, when the latter appears to have a greater fraction of volatile particles.

The morning UFP plumes’ high volatile particle number fraction values were related to volatile traffic particles. In atmospheric conditions without secondary nucleation mode particles due to photochemistry, the accu-

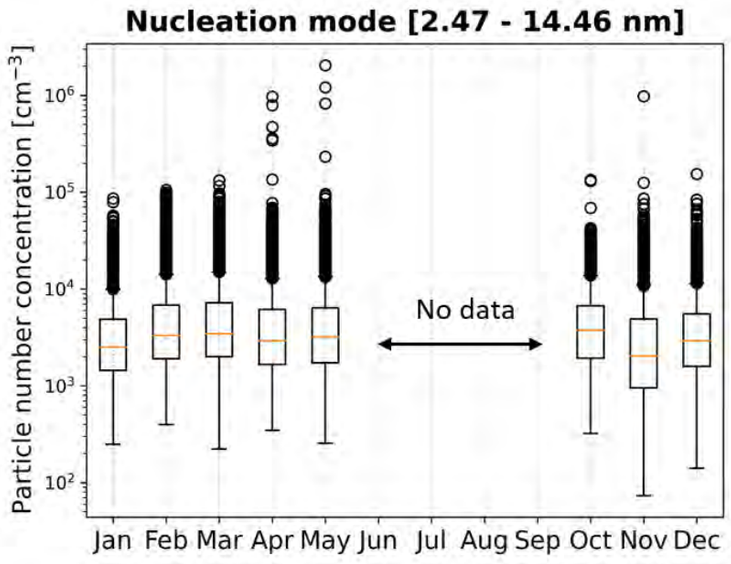

(a)

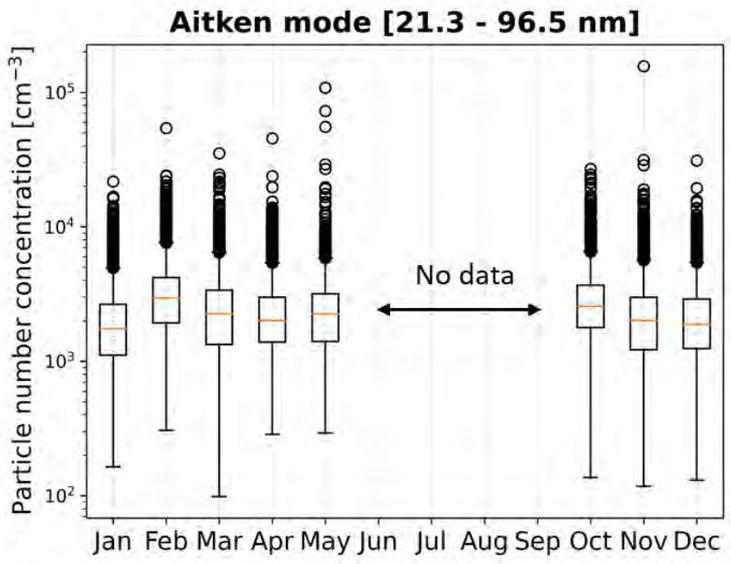

(b)

Figure 23: Monthly variation of particle number concentration of a) nucleation and b) Aitken modes presented by box plots. The central red marks indicate the median, the bottom and top edges of the box indicate the 25$^{\text{th}}$ and 75$^{\text{th}}$ percentiles, respectively. The circles represent the outliers (95$^{\text{th}}$ percentile). Data has a) 5-minute and b) 3-minute time resolution and covers the months October 2020 - May 2021.

mulation mode particles dominate in the morning due to traffic emissions. As the boundary layer rises and mixes, the concentration of the emissions dissipates. In most cases, the vertical mixing suppresses the local source signals. Therefore, rush hour related emissions should have a greater impact when inversion is stronger in the colder season. However, this is not the case for our data and it is possible because "fresh UFPs" and background particle features were not too different in the colder season.

The second peak that is noticed in the afternoon was related to NPF, especially to the gas-to-particle conversion of secondary nucleation mode atmospheric particles due to photochemistry. The greater volatile particle number fraction during the afternoon in spring compared to winter was in good agreement with the observation of more NPF events in the warmer months (40 events) in contrast to the colder period (7 events).

To better understand if the UFPs are of primary and/or secondary origin, equivalent black carbon (eBC) concentration at 950 nm [ng/m^3] was used. The wavelength of 950 nm was chosen as it must be in the infrared range to not interfere with other species (section 1.1.5). eBC concentration is presented in Figure 25. The hour values are in LT. The values showed peaks during the morning and evening traffic rush, around 7-8 and 18-20 LT, respectively. The diurnal cycle of eBC is useful to quantify the diurnal pattern of regional traffic emissions. However, eBC is mass-based and not necessarily the dominant contributor to the number of particles emitted by traffic, at least in certain size ranges. If eBC was a dominant contribution to UFPs number, then the UFP' volatile particle number

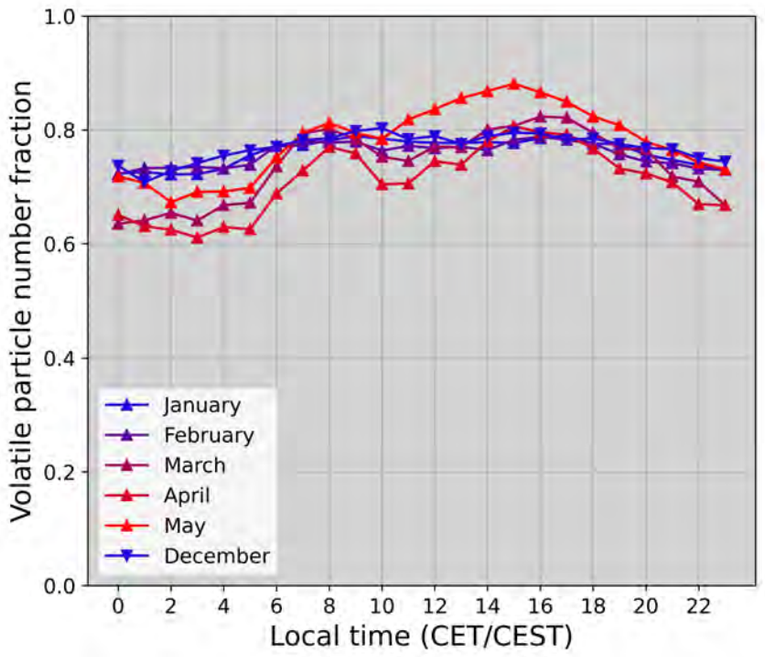

Figure 24: Hourly variations of volatile particle number fraction values between December 2020 and May 2021.

fraction would need to drop concurrently with traffic-related UFP number increase.

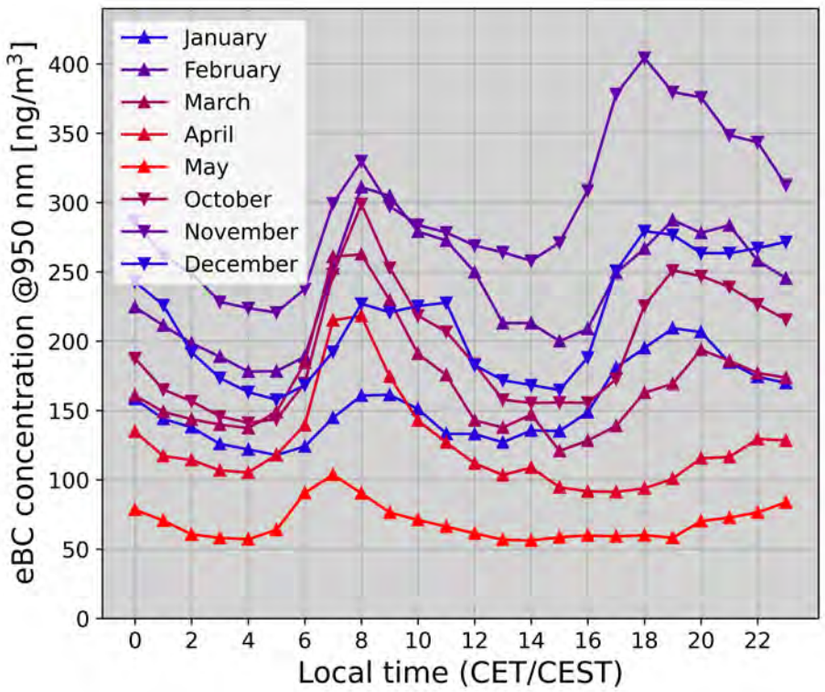

Figure 25: Hourly variations of equivalent black carbon (eBC) at 950 nm [ng/m^3]. Data has 1-hour time resolution and covers the months October 2020 - May 2021.

The boundary layer (BL) is another factor influencing the temporal behaviour of primary UFPs. For a visual detection of BL, we used wind speed data as a proxy for BL mixing. Similar to Figure 25, Figure 26 illustrates the hourly variation of wind speed [m/s] from a 10-minute time resolution data, during October 2020 - May 2021. In the morning, the wind speed is lower compared to the afternoon, thus there is no mixing of the BL. When the UFPs were detected during this period of little mixing, we assume that the source was close to the station. In the afternoon, as the troposphere is warming, the warm air rises through convection, thus enhancing the mixing of the BL.

In the evening, the solar heating of the surface and the convection stops. So, there are no turbulent eddies from the mixing and the air that was mixed during the day remains in the residual BL. Because there is no convection, the wind is not affected by the friction, so it can increase because of the pressure gradient. Because of the wind, a shear appears and there is a little mixing in the BL, so the BL is a little higher during the night compared with the

BL during the morning [Rotach and Calanca, 2019]. The height of BL can explain the presence of more primary UFPs in the morning compared to evening, even during rush hours.

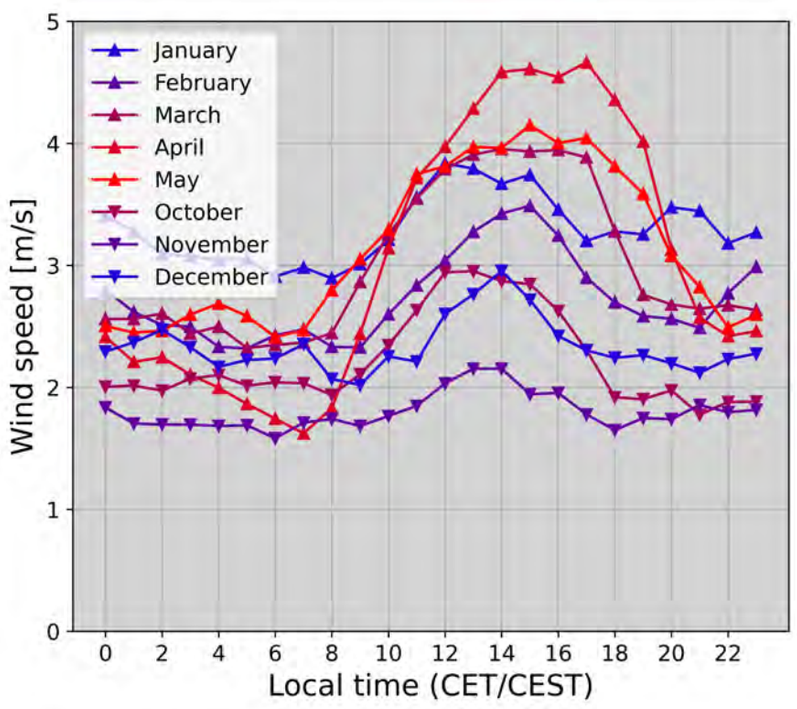

Figure 26: Same as Figure 25, but for wind speed [m/s] and data has 10-minute time resolution.

Different days with NPF events, primary UFPs and non-events are shown below to help understanding in distinguishing between them. A NPF event day is considered a day when a NPF occurred while a non-event day represents a day when no NPF event occurred. Figures 27a, 27b and 27c present data measured on May 30 (NPF event between 10 and 20 LT marked by the grey patch), January 26 (primary UPFs around 6 LT and 18 LT marked by blue and green patches, respectively) and January 23, 2021, respectively. They are similar to Figure 17, but there are also time series for D) total particle number concentration in the range of 0–25,000 cm^{-3} for SMPS (black) and CPC (red) and E) volatile particle number fraction.

A "show-case" of a day with one NPF event is shown in Figure 27a. One NPF event occurred between 12:00 and 22:30 LT (marked by grey patch). The volatile particle number fraction was in the range of 0.70-0.87, with the maximum value of 0.87 at noontime, around 13:00 LT. During the entire studied period, 96% of the NPF events presented volatile particle number fraction values above 0.75.

For January 26, 2021, shown in Figure 27b, UFPs during morning hours were found between 6-11 LT (marked by blue patch), with the peak around 9 LT. The evening rush hours lasted between 18 and 22 LT, marked by a green patch. Around 18 LT, the spikes in the total particle number concentration, along with high concentrations observed in normalized particle distribution, could be also traffic-related UFPs. The volatile particle number fraction was in the range of 0.8-0.9 both in the morning and evening, being consistent with previous statements that primary UFPs are also volatile. The sharp drops in volatile particle number fraction could be related to on-road vehicles because they overlapped with high values in eBC concentrations (150 ng/m^3), as it will be observed in Figure 28b.

January 23, 2021 (Figure 27c) was selected as it represents a non-event day. The volatile particle number fraction was greater than 0.7 in mean value even if it was a non-event day. These single-day examples were consistent with the findings of the overall diurnal variability as all of them have similarly high volatile particle number fractions. The low spike in the volatile volatile particle number fraction was associated with eBC concentration of 30 ng/m^3, as it will be observed in Figure 28c, which could be an indication of the absence of on-road vehicles, but another source of primary particles. Nonetheless, the low spikes presented above for January 26 and 23 could be due to an instrumentation error, and the overlap with high eBC concentration for January 26 could be only a coincidence.

For our example days, we plotted the time series for eBC at 950 nm [ng/m^3] for the entire days in Figures 28a, 28b and 28c. The scale is between 0 and 300 [ng/m^3]. For the event day (Figure 28a), the eBC concentration was higher in the morning (approx. 150 [ng/m^3]) compared to the values during the NPF event (50 [ng/m^3]). Also, the values during a non-event day had a maximum of 50 [ng/m^3], similar to the event day. eBC is an indication of

the variability of regional traffic contribution to UFPs. By comparing Figures 27b and 28b, we could conclude that both UFP spikes in the morning and in the evening are most probably traffic related.

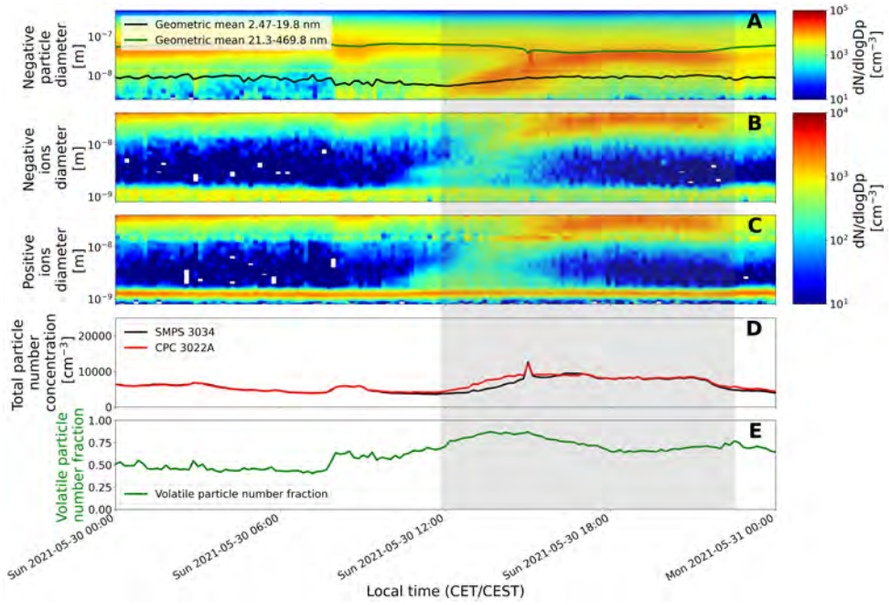

(a)

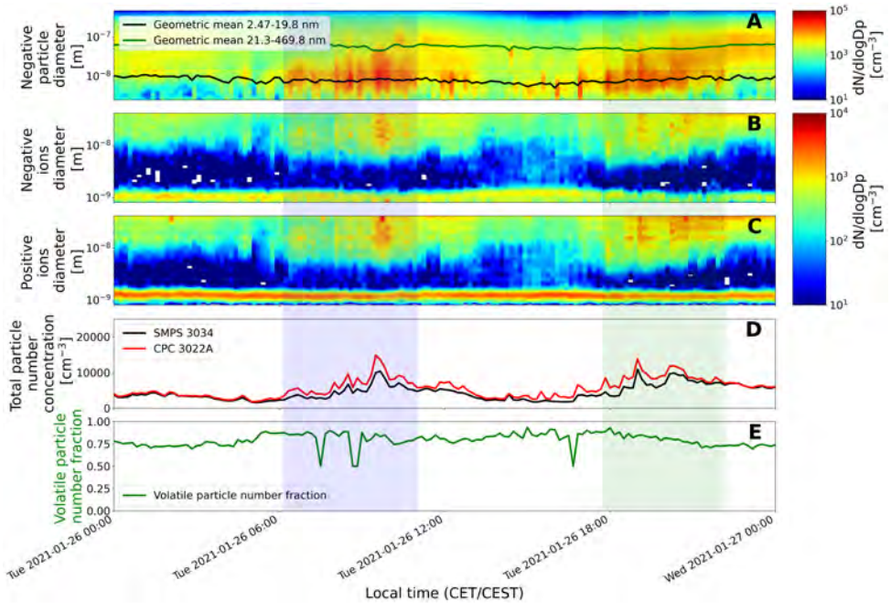

(b)

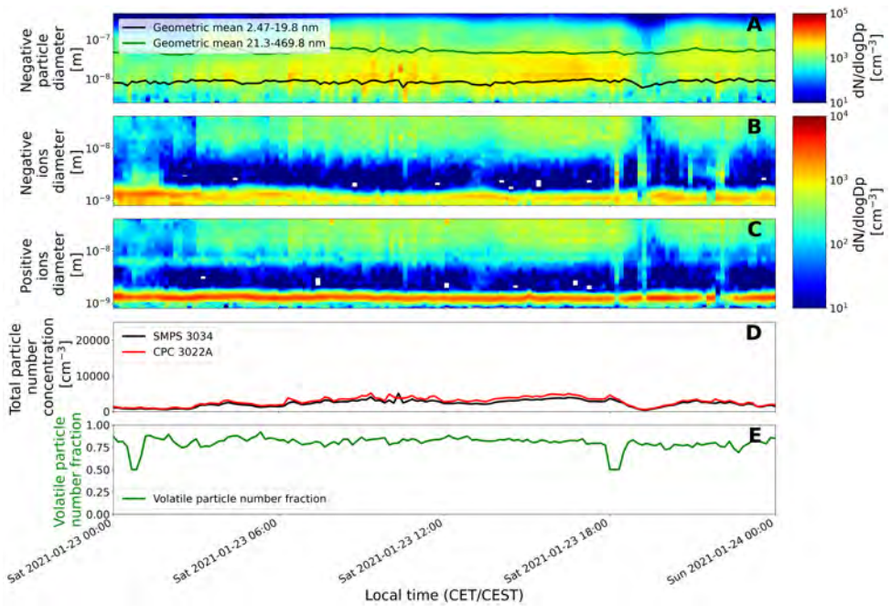

(c)

Figure 27: Same as Figure 17, but also time series for D) total particle number concentration in the range of 0–25,000 cm^{-3} for SMPS (black) and CPC (red) and E) volatile particle number fraction. Measurements were conducted on (a) May 30 (NPF event between 10 and 20 LT marked by grey patch), (b) January 26 (primary UPFs around 6 LT and 18 LT marked by blue and green patches, respectively), and (c) January 23 (non-event day), 2021.

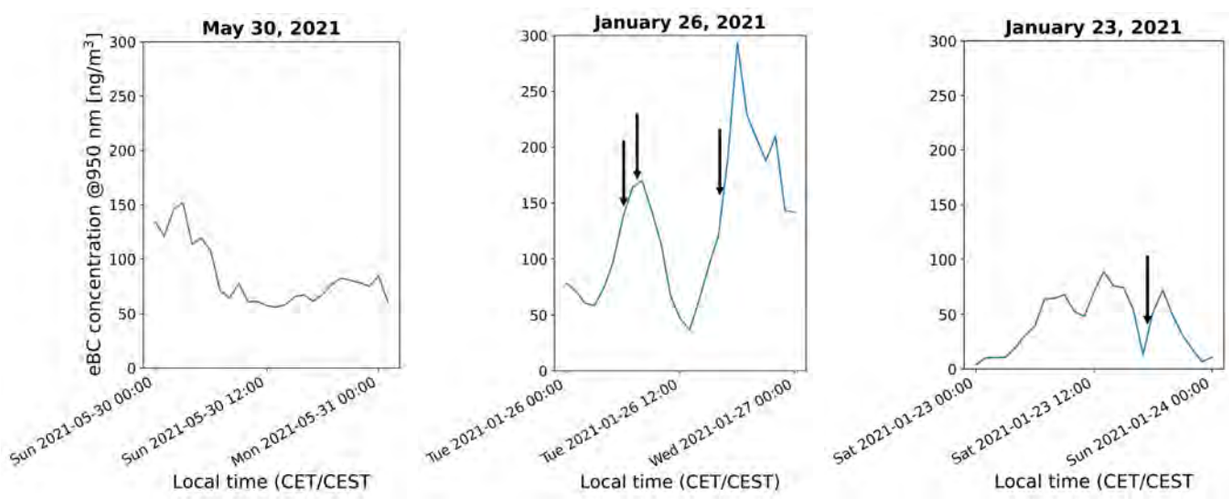

(a) (b) (c)

Figure 28: Time series of 1-hour time resolution of eBC at 950 nm [ng/m^3] for (a) May 30, (b) January 26, and (c) January 23, 2021. The black arrows suggest the time periods with low spikes in volatile particle number fraction.

3.2.3 Diurnal variability of ultrafine particles

Diurnal variability of nucleation and Aitken modes provides information on the primary UFPs and NPF cycles. Due to the supposed origins of primary UFPs and the production mechanism of NPF, we would expect to find different diurnal cycles, e.g. primary UFPs during rush hours and NPF during noon-afternoon time.

Figures 29a and 29b depict the diurnal variation of particle number concentration of (a) nucleation and (b) Aitken mode. Data has a 10-minute time resolution and covers the months October 2020 - May 2021. By analysing the diurnal variability of the nucleation mode, there was a clear cycle. For the nucleation mode particles, the highest concentration was found in the morning, between 7-8 local time (LT). Due to the time of the day when the morning rush hours took place and the lack of solar radiation, these nucleation mode particles were assumed to be primary UFPs rather than NPF. Between October and January, the concentration had its minimum during the afternoon period, followed by another peak in the evening. The evening nucleation mode particles were assumed to be primary UFPs, similar to the morning peak. However, the peak was prominent during colder months due to low boundary layer heights and low atmospheric mixing. Between February and May, the second peak in nucleation mode particles occurred between 13 and 15 LT because of more NPF events from the secondary PM.

The Aitken mode cycle (Figure 29b) is similar to the nucleation mode, but the number concentration values were around half in intensity compared to the nucleation mode ones. There were two peaks in the hourly mean concentration. One peak was found in the morning between 8 and 10 LT. The second peak was noticed in the evening after 19 LT, except for April and May with the highest values between 16 and 17 LT. The diurnal cycles suggest that the nucleation mode primary particles could grew during the rush hours or there could be direct emissions of both nucleation and Aitken mode primary particles. Moreover, the Aitken mode cycle showed a higher minimum particle concentrations than the nucleation mode cycle.

The analysis of diurnal patterns of total particle number concentration between 2.45 and 468.9 nm (Figure 29c) demonstrates that variability of total particle number was driven by variations in UFP number, which itself had a greater contribution from nucleation mode and a smaller contribution from Aitken mode. Figure 29c shows higher particle number concentration in the morning compared to noon, suggesting a large contribution of anthropogenic particles source in the morning. Moreover, the warmer months with a higher nucleation mode particle concentration showed a smaller peak during the afternoon, being an indication of NPF during that time period.

Figures 29a-29c illustrate that the evening rush hour peak is similarly important to the morning rush hour peak in the colder seasons. In the warmer season, only the morning rush hour peak was seen, whereas the evening rush hour peak was obscured by boundary layer dynamics.

The geometric mean diameters of all particles falling within the nucleation and Aitken modes, i.e. between 2.47-19.8 nm and 21.3-96.5 nm, respectively, was analysed to gain further insight into the contribution of primary versus secondary nucleation mode atmospheric particles. The hourly variation of geometric mean diameter calculated for particles between (a) 2.47–19.8 nm and (b) 21.3-96.5 nm is presented in Figures 30a and 30b, respectively. Data has a 10-minute time resolution and covers the months October 2020 - May 2021. Geometric mean diameter for nucleation mode particles (Figure 30a) illustrates that both primary and NPF particle size within the nucleation mode during the day was smaller than the night-time background.

Figure 30b exhibits a different pattern for geometric mean diameter between 21.3 and 96.5 nm. The values increased after 3-4 hours after the morning rush period, revealing a peak at around 13 LT, followed by a decrease in the evening, with a low peak between 17-18 LT. Therefore, Aitken UFPs from local and regional sources were smaller than Aitken background UPFs. Diurnal patterns of UFPs were the main driver behind the diurnal pattern in overall geometric mean diameter.

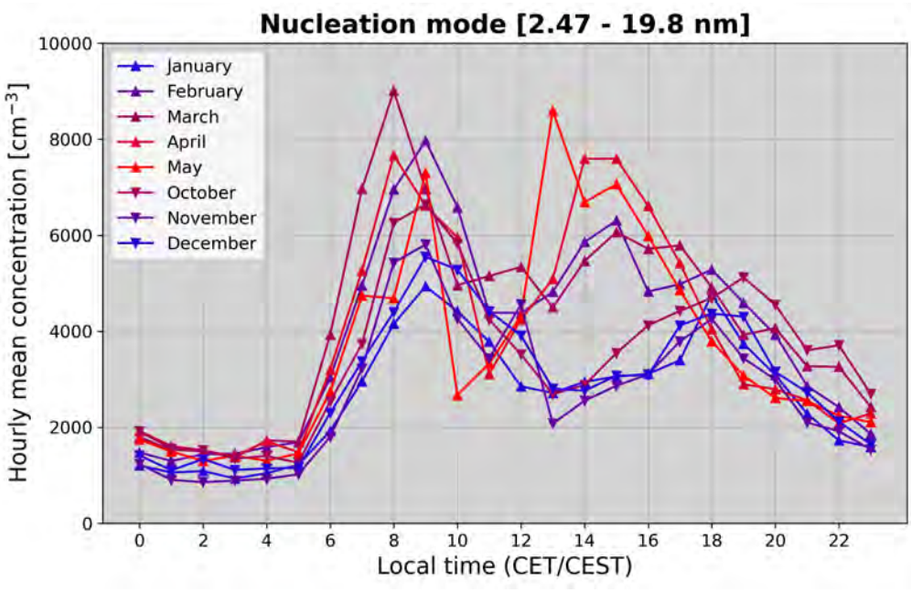

(a)

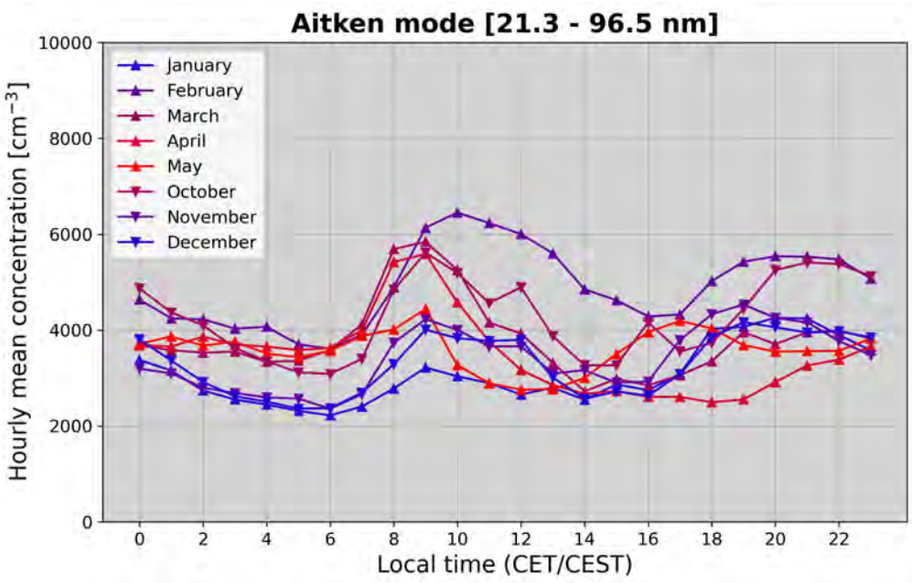

(b)

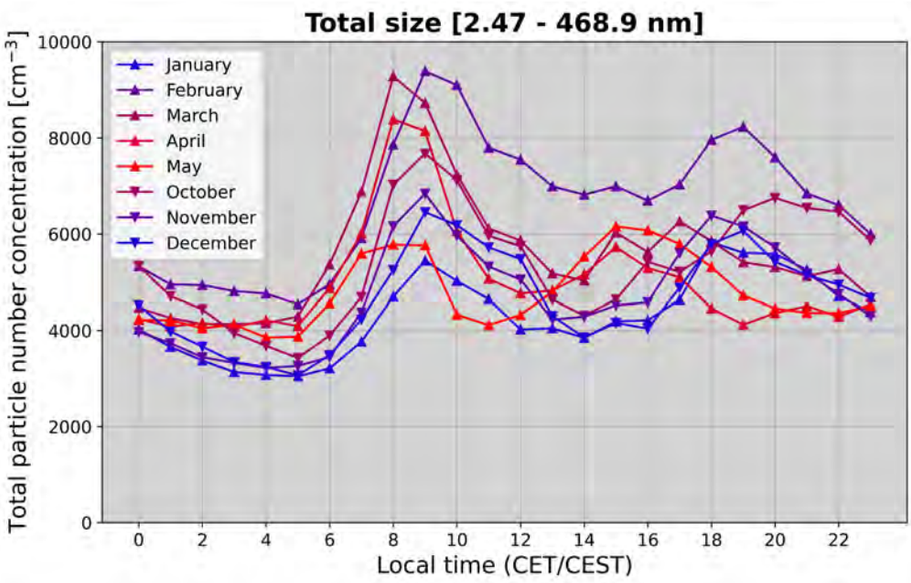

(c)

Figure 29: Diurnal variation of (a) nucleation mode, (b) Aitken mode and c) total particle number concentration. Data has a 10-minute time resolution and covers the months October 2020 - May 2021.

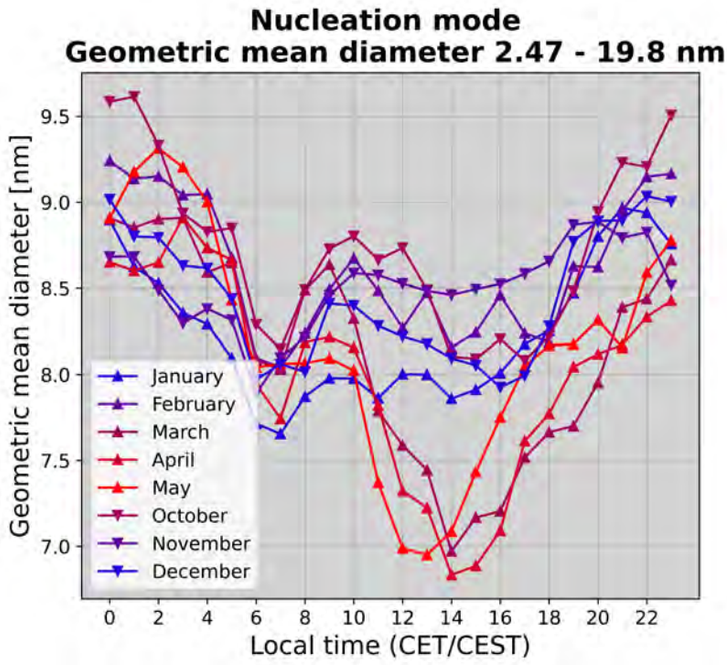

(a)

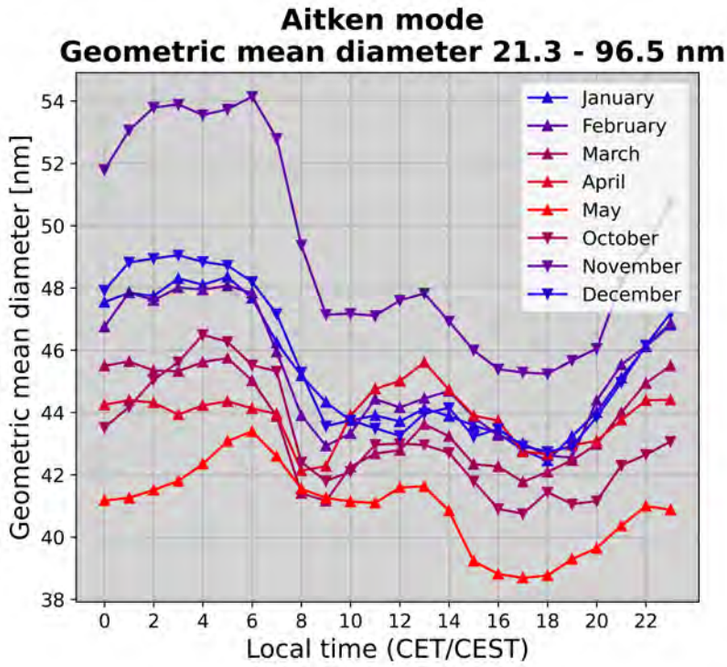

(b)

Figure 30: Same as Figure 26, but for geometric mean diameter between (a) 2.47–19.8 nm and (b) 21.3-96.5 nm.

3.3 Primary ultrafine particles

As we saw in sections 3.2.2 and 3.2.3, primary UFPs usually appear during the traffic rush hours. Because of their diurnal cycle, we further continued the investigation to understand if on-road vehicles represent the only potential source of primary UFPs or emissions from gas turbine aeroplanes can also be detected at the measurement site.

For a better insight into the analysis of potential sources, we also investigated the meteorological conditions (wind direction and wind speed) and trace gas concentrations (SO_2 and NO_x). Moreover, for a better distinguish between on-road vehicles and gas turbine aeroplanes, we used normalized non-volatile particle size distribution covering both nucleation and Aitken modes.

The analysis of primary UFPs was done for the entire studied period regarding wind direction, but only for 5 days (January 18 - January 23, 2021) concerning a more detailed investigation. Therefore, the primary UFPs is still an ongoing investigation. From the short studied period, we could make suppositions about the primary UFP sources, but the analysis of sources, diurnal variability and seasonality requires a longer time interval.

3.3.1 Potential sources of primary ultrafine particles

Starting with the investigation of wind direction for morning UFPs, we gained information about the location of sources. Figure 31 illustrates the probability density function of the total wind direction (purple bars) and the mean particle number concentration for each wind direction bin (blue line). The values were considered during morning rush hours, between 6 and 10 LT for the entire studied period (October 2020 - May 2021). The probability density function plot shows the frequency of each wind direction, while the line plot provides information about what directions exhibited the highest UFPs' concentration. The most frequent direction of wind blowing was between 180° and 220°, with a maximum between 200° and 210°. In contrast, for these wind direction values, the mean particle number concentration presented a local minimum, around 3500 cm^{-3}, underlying that the mean particle number concentration depended only weakly on wind direction. Similar was for the second most frequent wind direction (30°-40°) when the minimum of mean particle number concentration during the studied period was found at about 3000 cm^{-3}. On the other hand, when the mean particle number concentration showed the maximum values (7000 cm^{-3}, followed by 5000 cm^{-3}) the wind direction (270°-300°) manifested the least influence.

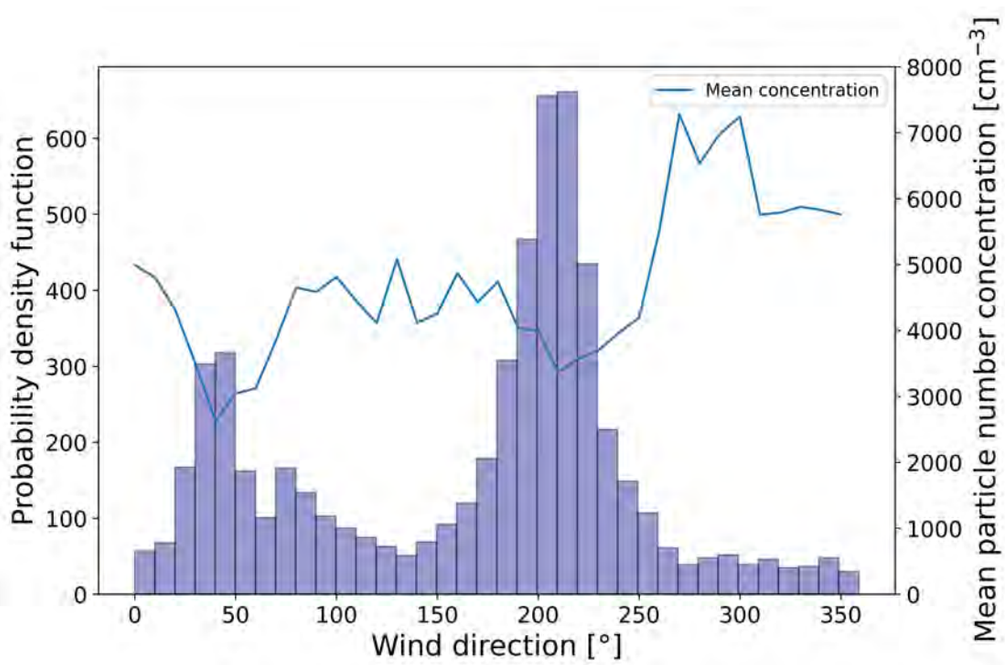

Figure 31: The probability density function of the total wind direction (purple bars) and the mean particle number concentration for each wind direction bin (blue line). The values were considered during morning rush hours, between 6 and 10 LT for the entire studied period (October 2020 - May 2021).

Besides the particulate matter properties (section 3.2.2), seasonal and diurnal variability (sections 3.2.1 and 3.2.3) and meteorological measurements discussed above, we used normalized non-volatile particle size distribution

data in the range of 0-20 nm to investigate primary UFP sources. The non-volatile nucleation mode particles were detected using the switchable catalytic stripper as presented in section 2.4. The measurements helped with the analysis of the sources of primary UFPs. If the particles were non-volatile, they were usually soot particles from vehicles or gas turbine aeroplanes. Our starting hypothesis was the following: while diesel car engines produce soot particles with a peak between 50 and 100 nm, the gas turbine aeroplanes produce emissions at sizes smaller than 20-30 nm [Allouis et al., 2010]. The highest concentration of nucleation mode non-volatile particles by an aeroplane is produced at taking off, but also idle exhaust consists of large amounts of non-volatile particles [Durdina et al., 2017]. Aviation emissions consist primarily of carbon dioxide, water vapour, NO_x, SO_2, BC [Lee et al., 2010], [Freeman et al., 2018].

We studied the non-volatile particles for a period of five days (January 18, 2021 - January 22, 2021). The period was chosen so all of the instruments were working properly. In Figure 32, the normalized size distribution is plotted for non-volatile particles between 6.38 and 224.7 nm, together with meteorological (wind direction and wind speed), trace gases (SO_2, NO_x), particulate matter properties (volatility and eBC) data and total particle number concentration from SMPS and CPC. To distinguish aircraft emissions from traffic-related UFPs, we analysed the concentration peaks for both nucleation and Aitken modes. The upper limit for nucleation and Aitken modes is marked by the black and green dashed lines, respectively.

By analysing the normalized non-volatile particle size distribution (Figure 32A), we could identify if the particles were found in nucleation or Aitken mode, or both of them. We took January 20 as an example day due to its broad size range for high concentrations (marked by the grey patch). One high peak in concentration was observed at the noon-afternoon time. The high peak presented a wide particle diameter range, between 10 and 150 nm, which could be associated with both gas turbine (nucleation mode) and traffic-related emissions (Aitken mode).

Even if the dependence of the particle number concentration on wind direction was weak, we could use wind direction and wind speed as an instrument used to differentiate between the main road and airport influences. As is shown in Figure 32B), for three out of five days (January 20-22), we could see the wind blowing from the airport direction (values from northwest and northeast). However, on January 20, a mixture between airport and road directions (southeast and southwest) was observed. The wind speed for the entire period showed values between 2 and 10 m/s, high enough to transport pollutants from the airport (located at 4 km away from the measurement station). Kim et al. [2015] stated that wind speeds higher than 2 m/s could influence vehicular pollutants transport.

Because trace gases (SO_2, NO_x) could be emitted by gas turbine aeroplanes, higher values could represent an indication of aeroplanes influence. Higher concentration ($\sim$10 $\mu g/m^3$) of NO_x were found overlapping with the high total number particle concentration and eBC values. During the studied period, SO_2 varied between 0.5 and 1 $\mu g/m^3$, with the highest concentrations of SO_2 found during January 20, when also the highest value in number concentration was observed. There were some strong short-time low peaks in volatile fraction reaching 0.5, which could be from aeroplanes emissions since traffic-related particles exhibited high volatile particle number concentration (section 3.2.2). However, this did not exclude the possibility of on-road vehicles emissions, since the low spikes coincided with high eBC concentrations for some time frames. To understand if the low peaks in the volatile particle number fraction were genuine, we compared their occurrence times with the ones from total particle number concentration. For most of the time, low spikes in volatile fraction values overlapped with high number concentrations, showing that there was not a problem with the instrumentation.

Similar to January 20, January 18 in the morning could be considered another example of high concentration (6000 cm^{-3}) values at both nucleation (particle diameter $<$ 20 nm) and Aitken mode (particle diameter between 20 and 40 nm) sizes (marked by the yellow patch). For particle diameter values greater than 40 nm, the number concentration decreased to 4000 cm^{-3}. Therefore, the strongest primary UFP emissions were found for particles smaller than 40 nm in size, compared to January 20, when the highest concentration was observed for a broader size range. Because of the wind direction (mainly southwest), during that day the airport emissions were not significant, hence the main influence was the main road.

Oppositely to January 20, on January 18, SO_2 concentration was around 0.5 $\mu g/m^3$. Only NO_x values were high, around 50 $\mu g/m^3$. The eBC values showed a peak during the morning. Because there were non-volatile particles both in nucleation and Aitken modes, we would have expected influences from gas turbine aeroplanes and on-road vehicles, respectively. However, it seemed that this was a case when on-road traffic emissions start from

the nucleation mode. Therefore, considering the meteorological, trace gas and parameters data, we concluded that the on-road traffic had the main influence on non-volatile primary UFPs on that day, unlike our expectations. Yet, more research is required to assess the sources of primary UFPs, including additional data of the airport flights daily schedule.

Our starting hypothesis stated that diesel car engines produce soot particles in the Aitken mode. However, the observations on January 18 contradicted the hypothesis. The contradiction could be caused by Diesel Particulate Filters (DPFs) and/or Gasoline Direct-Injection (GDI) engines that could play a role in shifting the average size of non-volatile cores from Aitken to the edge of nucleation mode. During DPF utilization, emissions present also nucleation mode particles besides Aitken mode particles, which increase particle number concentration [Yanagisawa et al., 2010]. GDI engines generate a greater number of UFPs compared to diesel engines. They are also a source of nucleation mode particles [Raza et al., 2018] and their BC emissions from GDI engines are significantly higher than the ones from usual diesel engines [Liggio et al., 2012].

Taking into consideration the above-discussed results, between January 18 and January 22, 2021, both traffic-induced and aeroplanes emissions were identified as primary sources of UFPs. Gas turbine aeroplanes, GDI and DPF engines were noticed influencing nucleation mode non-volatile particles. In contrast, diesel car engine emissions were observed in the Aitken mode non-volatile particles. Low spikes volatile particle number fraction and high eBC concentration values supported the finding of non-volatile UFPs.

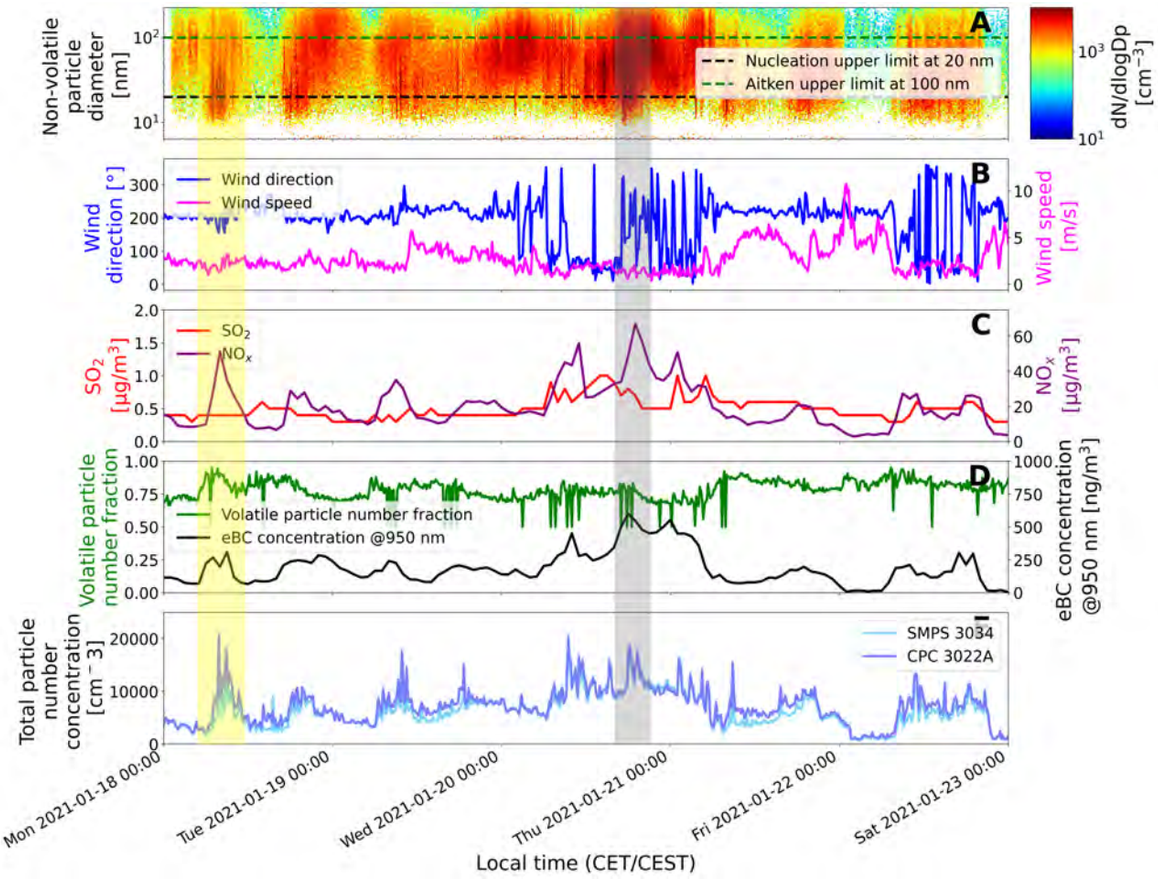

Figure 32: A) Normalized size distribution for non-volatile particles between 6.38-224.7 nm. Nucleation and Aitken modes upper limits are marked by black and green dashed lines, respectively. Time series of B) wind direction, wind speed, C) SO_2, NO_x, D) volatile particle number fraction and eBC concentration, and E) total particle number concentration. The yellow and grey patches highlight high number concentrations on January 18 and January 20, 2021, respectively. Measurements were conducted between January 18 and January 23, 2021.

3.4 New particle formation events

To further characterise NPF events at the Payerne site, we present the type of events classified by classes and assess how the occurrence or absence of NPF were related to meteorological parameters and trace gas concentrations. The analysed meteorological parameters were temperature, solar radiation, relative humidity, wind speed and wind direction. The discussed trace gas was H_2SO_4 proxy. Moreover, the growth rate and condensation sink provided information about the occurrence of the events and relevant atmospheric conditions.

3.4.1 New particle formation classification scheme

As presented in section 2.4, NPF events can be grouped into three classes: I (both the nucleation mode particles and growth), II (bump, the growth not observed.) and III (carried particles horizontally or vertically to the measurement site.). In the following figures, one example of each class is shown. Figures 33a and 33b show the A) normalized distribution for negative particles and time series for geometric mean diameters, and normalized distribution for B) negative ions and C) positive ions. Time series is also plotted for D) total particle number concentration in the range of 0–25,000 cm^{-3} for SMPS (red) and CPC (black). The measurement conducted on (a) February 17, 2021, can be representative for class I NPF event (grey patch) while the one on (b) May 13, 2021, for both class II (green patch) and class III (grey patch) at different time windows.

Class I NPF event occurred between 12:30-18:00 LT. Both the nucleation mode particles and the growth are noticed in ion (number concentration up to around 10^4 cm^{-3}) and particle mode concentrations (number concentration up to 10^5 cm^{-3}). For the second day, classes II and III events were observed. Class II event was around 14:30-15:30 LT, with no growth in particle size. The ion signal is not as pronounced as in the class I event, previously discussed (only up to 10^3 cm^{-3}). However, the particles concentration is about $5{\cdot}10^4$ cm^{-3}. After 2 hours, a class III event occurred around 17:30 LT and lasted about 1.33 hours. It shows the same intensity in concentration as the class II event. However, the event did not show a strong concentration between 3-20 nm in particle diameter, thus the particles could have been horizontally or vertically carried to the measurement site.

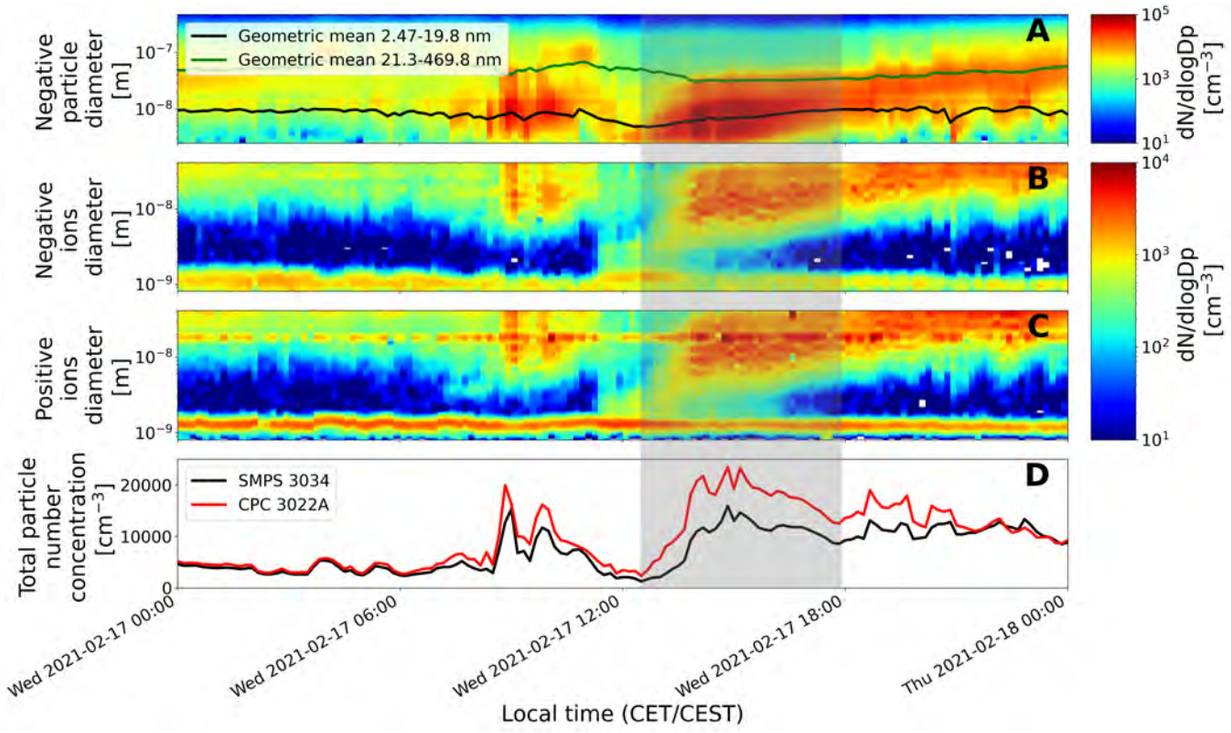

(a)

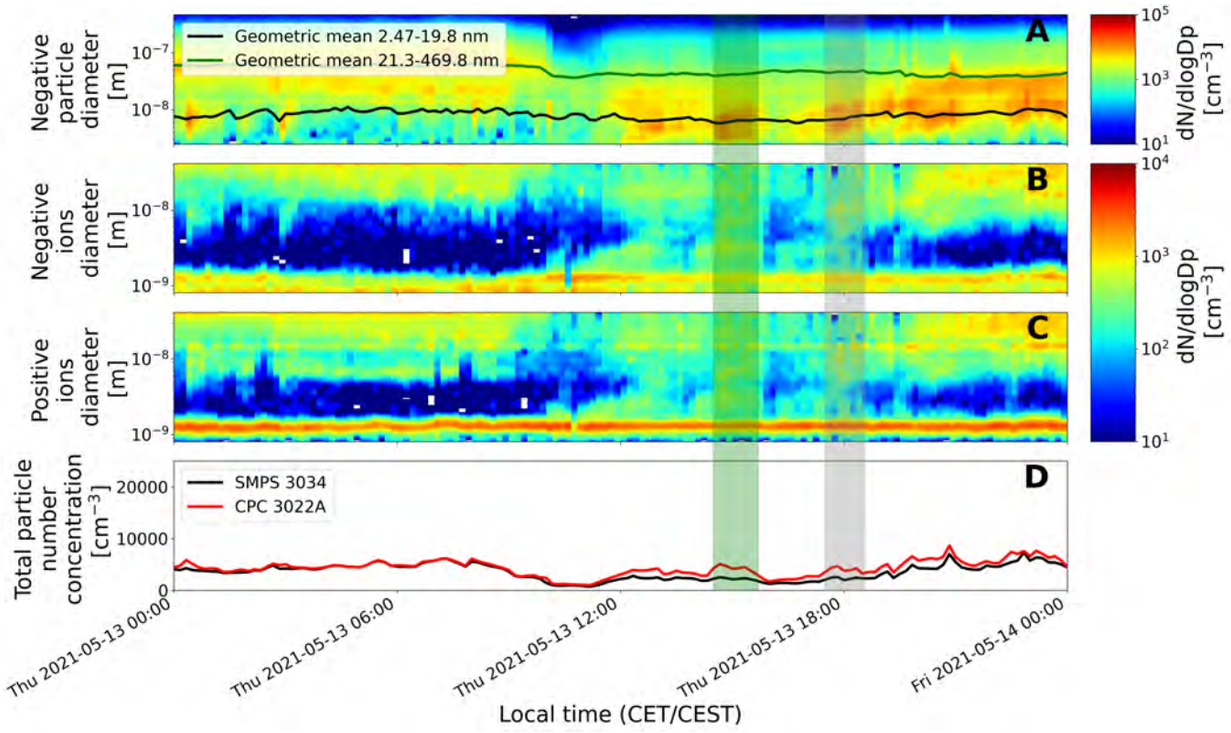

(b)

Figure 33: Same as Figure 17, but also time series for total particle number concentration in the range of 0–25,000 cm^{-3} for SMPS (black) and CPC (red). Measurements conducted on (a) February 17, 2021 (12:30-18:00 LT), can be representative for class I NPF event (grey patch) while the one on (b) May 13, 2021, for both class II (green patch) (14:30-15:30 LT) and class III (grey patch) (17:30-18:50 LT), respectively.

3.4.2 Frequency of new particle formation events

The frequency of each class shows the types of NPF events that occurred at the measurement site. Therefore, we gain a view on the evolution of NPF (if the secondary PM grew or not, if they formed locally at the station or were transported).

Figure 34a depicts the frequency of occurrence of Class I, Class II, Class III NPF events for the period October 2020 – May 2021. Around 9% of the days from the total period showed one or multiple class I NPF events. Class II NPF events were found for only 4.7% of days, while class III events percentage was the smallest with 3.8%.

The occurrence over the months separated by class is shown in Figure 34b. The number of NPF events increased during warmer months (March-May), especially the class I and II events, compared to the colder months (October-February). During the autumn months (October, November), only class III events were present, suggesting transported events to the measurement site. Because there is no data between June and September, we cannot comment on the NPF frequency of occurrence for this period.

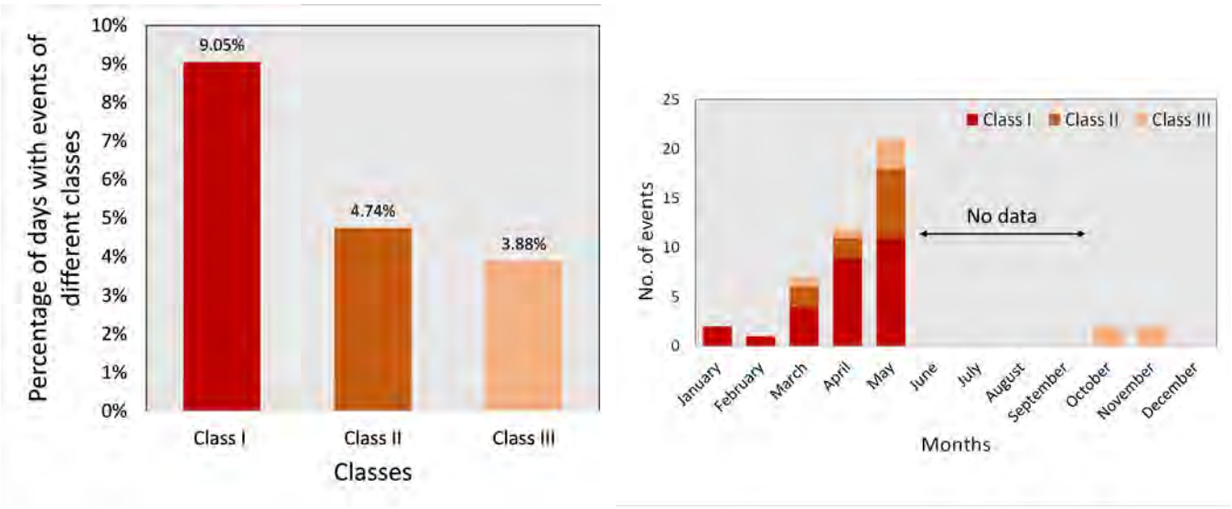

(a) (b)

Figure 34: (a) Frequency of occurrence of Class I, Class II, Class III. (b) Monthly number of events of Class I, Class II, Class III. Measurements during the period October 2020 – May 2021.

The geometric mean diameter at the end of the events provided information about the growth of the NPF. As is shown in Figure 35a, the final geometric mean diameter of the newly formed particles at the end of the NPF event remained within the nucleation mode, i.e. 20 nm or less, for more than 80% of the cases. In the majority of the cases, the growth ended at 10 nm (38% of the events) and 15 nm (32% of the events). The median value of the geometric mean diameter across the entire normalized size distribution was 13 nm. The maximal geometric mean diameter reached at the end of an event was 45 nm for 2.5% of the total NPF. The particles did not grow to be able to become CCN during the event day. However, this does not exclude further growth into the CCN size range on later days, as is seen in the example shown in section 3.1, Figure 22b. The event duration in hours is presented in Figure 35b. Around 32% of the events lasted 2 hours and 4% of the events lasted longer than 10 hours. The median event duration was around 3.2 hours.

Concerning growth rate (GR), because the calculated values of GR using the geometric mean diameter were not in agreement with what was previously established in the literature for the same type of environment (values were one order of magnitude lower than at other rural stations), we used also the maximum concentration method. For the maximum concentration method, we only calculated the maximum concentration for each bin, without further fitting. The GR_{3-15} (in the range of 3-15 nm) was calculated for NAIS values only. As noticed in [Nieminen et al., 2018], the GR values in the rural area are between 0.8-10.9 nm/h, with the majority between 2-4 nm/h. For our measurement site, the values were 0.7, 0.5 and 1.96 nm/h for GR_{3-7}, GR_{7-15} and GR_{3-15}, respectively. Our values may be smaller than the reported ones due to several reasons, e.g. weaker sources of secondary PM, efficient cluster scavenging at small sizes.

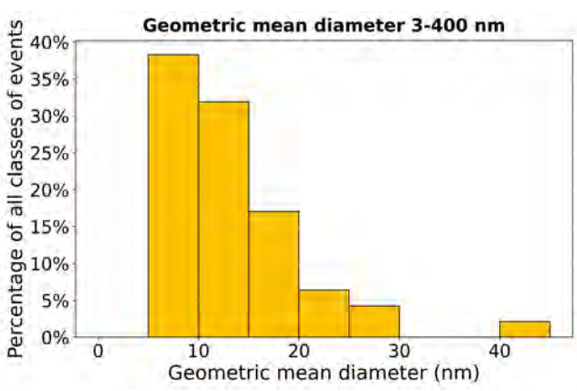

(a)

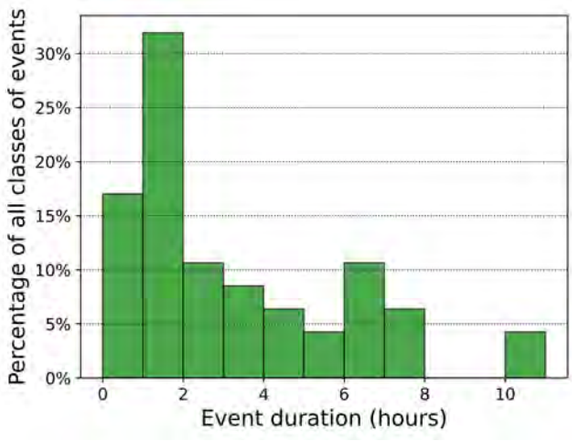

(b)

Figure 35: (a) Percentage histograms showing the frequency distribution of events growing to a certain geometric mean diameter. The geometric mean diameter was considered at the end of the events. (b) Percentage histograms showing the frequency distribution of event duration. Measurements during the period October 2020 – May 2021.

3.4.3 The influence of meteorological parameters on new particle formation events

The meteorological conditions can indicate the favourable conditions that can lead to NPF. Usually, higher solar radiation is the main factor affecting NPF frequency. Because our measurements covered the warmer season, between March and May, we expected to find more NPF events during that period.

The values of the meteorological parameters (solar radiation, temperature, RH, wind direction, wind speed, precipitation) were selected between 10 and 14 LT, being an interval of -2/+2 hours before and after the average occurrence time of NPF events, respectively, which was mainly at 12 LT. The NPF values of the classes quantities presented below represent the mean values of the meteorological parameters between 10 and 14 LT. The meteorological parameters are shown for the entire studied period (October 2020 - May 2021) as mean values in grey dots between 10 and 14 LT. The monthly mean values are plotted with a green line, representing the seasonality driven trend. For further analysis, we consider the trend line a threshold for understanding the driven parameter values for NPF. Classes I, II and III are shown in coloured circles from dark red to pink, respectively.

Figure 36a shows the NPF correlation with solar radiation. Solar radiation is one of the most important meteorological terms related to NPF discussion due to the OH· formation (section 1.4.1.2). By excluding warmer months (March-May) and one event in November, all NPF events occurred only on days with clearly above-average solar radiation, above the threshold values. Days are much longer in late spring and summer, thus sunshine during morning/noontime alone may be sufficient for triggering NPF on days with below-average solar radiation. However, we would need more warm-season data to draw more robust conclusions on this. From our data, higher solar radiation appeared as a favourable condition for NPF.

The correlation of NPF with temperature is presented in Figure 36b. Non-event and event days were similar in temperature values compared to the monthly mean trend. Even if only 53% of the events were found above the threshold line, 83% the NPF occurred at temperature values higher than 10 °C, while the maximum temperature during the studied time period was around 21°C. Higher temperatures usually occur during the time of the day with higher solar radiation, e.g. noontime, afternoon. The higher temperature should a priori counteract NPF. However, solar radiation overcomes the temperature when it comes to driving NPF. Monthly variation of solar radiation and temperature show a similar pattern, higher in spring-summer and lower in autumn-winter [Shrestha et al., 2019], thus the reason of resembling results of the relationships between temperature-NPF and solar radiation-NPF.

Lee et al. [2019] presented the effect of temperature on nucleation in chamber experiments. Lower temperatures are favourable for nucleation at the kinetic regime, decreasing the Gibbs free energy, so the condensation increases. Lower temperatures decrease the oxidation rates, thus the yields of condensable species. There is a competition between the two effects, however, overall there is an increase in the nucleation and growth rate [Baalbaki et al., 2020]. However, chamber experiments are understood typically much easier from a causality perspective, since fewer parameters are being varied simultaneously.

The analysis of NPF correlation to RH is shown in Figure 36c. All events (except for November, March and May) were associated with below-average RH values of a maximum of 70%. As Hamed et al. [2011] mentioned, high RH values may suppress the NPF, but not necessarily [Salma and Németh, 2019], [Baalbaki et al., 2020]. RH increase leads to water vapour increase. Thus, preexisting aerosols take up water vapour, so condensation and coagulation sinks may increase. The increase of CS is correlated with a higher loss term for condensable vapours, e.g. sulfuric acid. The growth of the coagulation sink leads to an increase in the coagulational scavenging of freshly formed clusters on the preexisting particles before they can grow large enough to be detected by instruments. Also, the anticorrelation between the RH and NPF may be related to solar radiation. Solar radiation is the key driver of photochemistry, which further leads to NPF via sulfuric acid and condensable organics. Solar radiation is lower when there are clouds and RH increases. Also, the diurnal pattern of RH shows a minimum around noon-afternoon when temperature has its maximum and can take up more water vapours and usually NPF events occur [Hamed et al., 2011]. Moreover, RH reveals an opposite behaviour compared to temperature and solar radiation, with high and low values in colder and warmer months, respectively [Shrestha et al., 2019].

Wind direction (Figure 36d) and wind speed (Figure 36e) were important factors in analysing the potential sources of NPF. The wind direction trend line suggests that the wind in mean value was mainly blowing from the main road direction (southeast and southwest). Also, NPF events mainly occurred for the wind blowing from the

main road direction (south and southwest). There was a small influence from the airport direction in the north. Thus, the airport could be a source of particles leading to NPF if they were transported from there. The discussion related to airport influence through SO_2 oxidation will be held in section 3.4.4. The wind speed during the NPF events was above the threshold for 70% of the total events, greater than 3 m/s, showing the possibility of particle transport to the site. Regarding the precipitation correlation, all NPF events occurred during no precipitation days.

For all meteorological parameters, by comparing the relationship between each class and the parameter, we concluded that NPF behaved similar regardless of class. The analysis between non-event days (grey dots) and event days (coloured dots) did not reveal similar behaviour in absolute values compared to the monthly mean trend, underlying the meteorological influence on NPF. However, there were non-event days with similar values as the event days ones that did not result in event days, concluding that meteorological parameters alone cannot explain NPF.

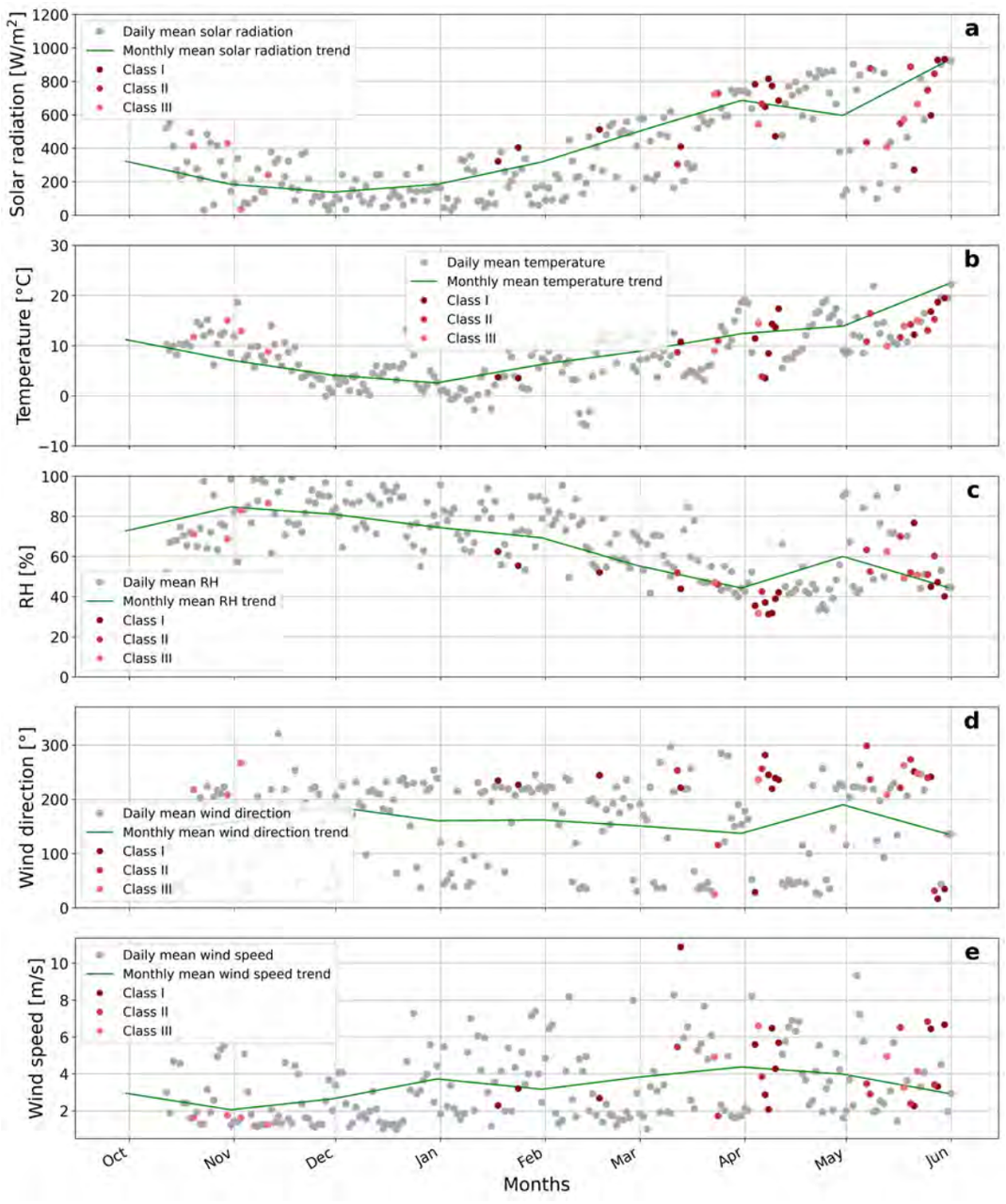

Figure 36: NPF correlation with meteorological parameters: a) solar radiation, b) temperature, c) RH, d) wind direction and e) wind speed for the entire studied period (October 2020 - May 2021) as mean values in grey dots between 10 and 14 LT. The monthly mean trend is plotted with a green line. Classes I, II and III are shown in coloured circles from dark red to pink, respectively.

Figure 37 shows an example of class I NPF event (grey patch) which occurred on May 28, 2021, between 14 and 21 LT. The figure is similar to Figure 17, but there are also time series are plotted for total particle number concentration [cm^{-3}], solar radiation [W/m^2], temperature [°C] and RH [%]. This day constitutes a typical example of the values of solar radiation, temperature and RH during NPF. Both solar radiation and temperature values were high at the start of the NPF event, around 1000 W/m^2 and 20 °C. Also, as it was previously mentioned, the event occurred at low RH values, decreasing from 50 to 25%. The wind rose plots (Figures 38a-38d) illustrate the frequency

of winds blowing from a specific direction for May 28, 2021, between 9-21 LT, with a time step of 3 hours. The plots show that the wind blew between north and northeast from 9 to 15 LT. During the NPF event (between 14-21 LT), the wind direction was north-northeast and the wind speed was between 4 and 5 m/s. This correlation shows a plausible airport influence on this NPF event. However, for a detailed causality between airport and receptor site, a further investigation on trace gas data (sulfuric acid proxy produced from sulfur dioxide) is required, which will be discussed in section 3.4.4.

Same as Figure 37, but for April 9, 2021, we analysed solar radiation, temperature and RH in relationship with NPF, which occurred between 11:30 and 18 LT (Figure 39). All of them were similar in values to the ones from the previous example, even if solar radiation showed one low peak related to clouds presence. On the other hand, the wind direction showed an opposite direction, blowing from the southwest, and its speed was almost double in intensity with a maximum of 9 m/s (Figures 40a-40d). This finding is a counter-example for the airport having an influence on NPF. Therefore, the airport could be relevant in NPF, but this did not represent an exclusive source.

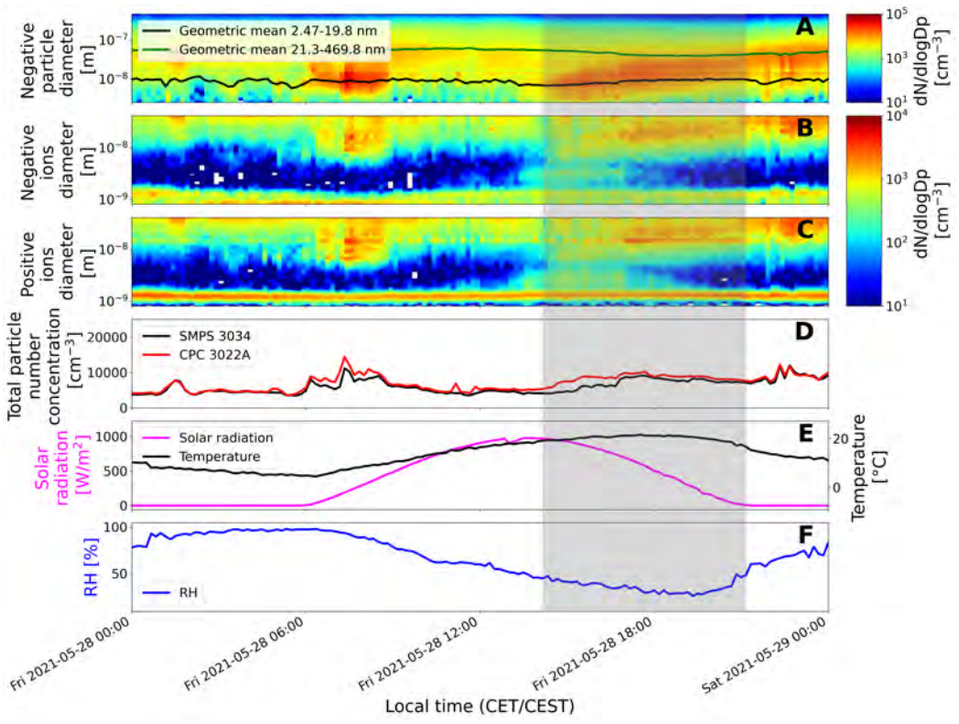

Figure 37: Same as Figure 17, but also time series for D) total particle number concentration, E) solar radiation, temperature and F) RH. Grey patch shows the time period for the Class I NPF event. Measurements conducted on May 28, 2021.

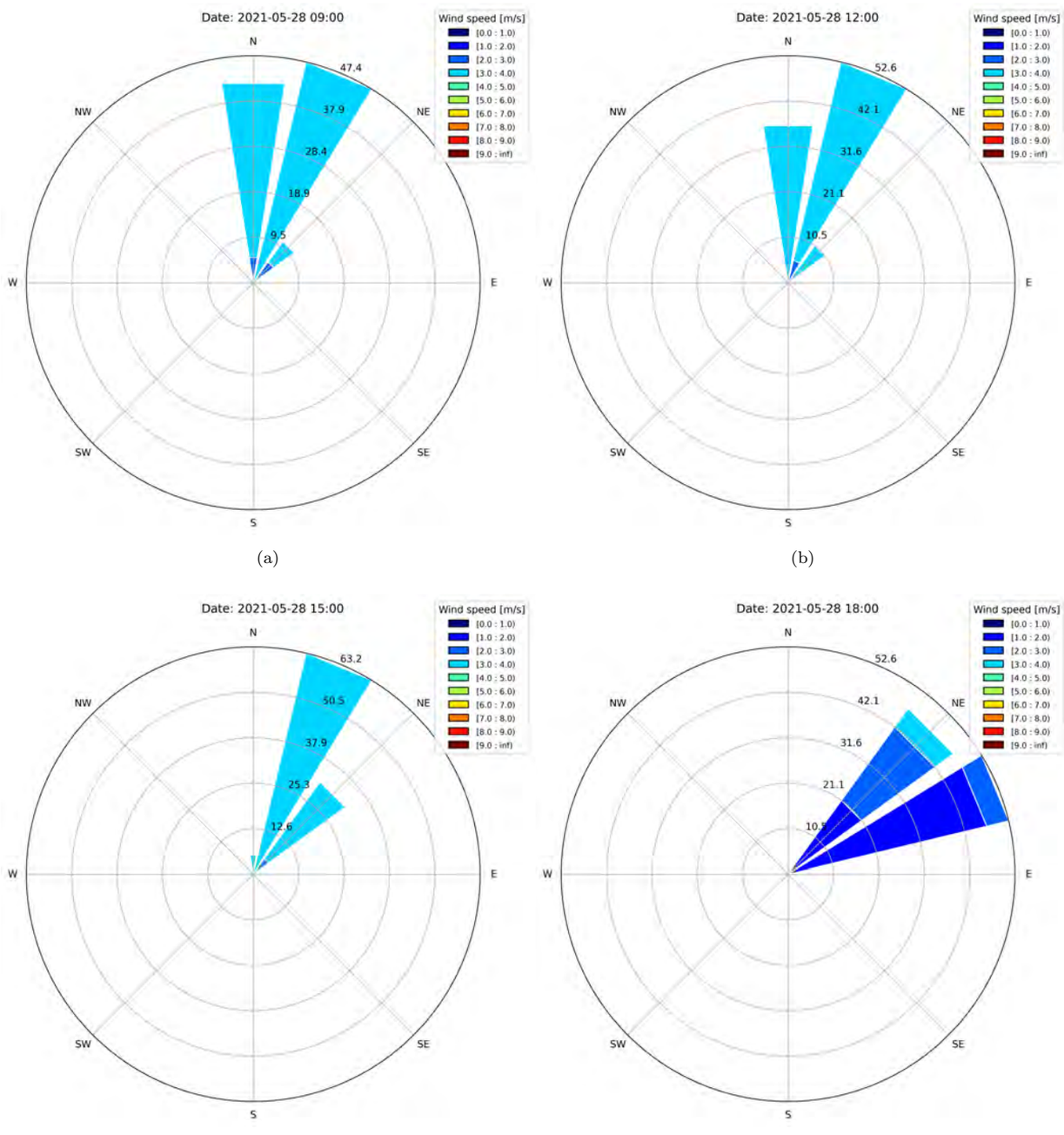

(a) (b)

(c) (d)

Figure 38: Wind rose showing the frequency of winds blowing for May 28, 2021, between a) 9-12 LT, b) 12-15 LT, c) 15-18 LT and d) 18-21 LT. The step is 3 hours. Wind speed is between 0 (dark blue) and 10 m/s (dark red).

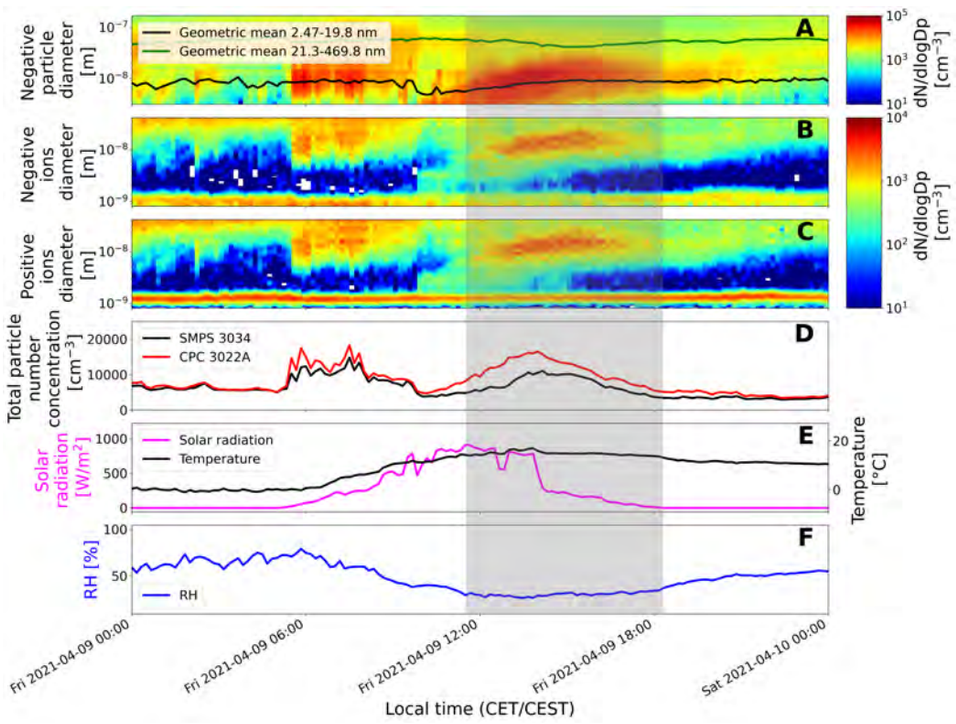

Figure 39: Same as Figure 37, but for April 9, 2021.

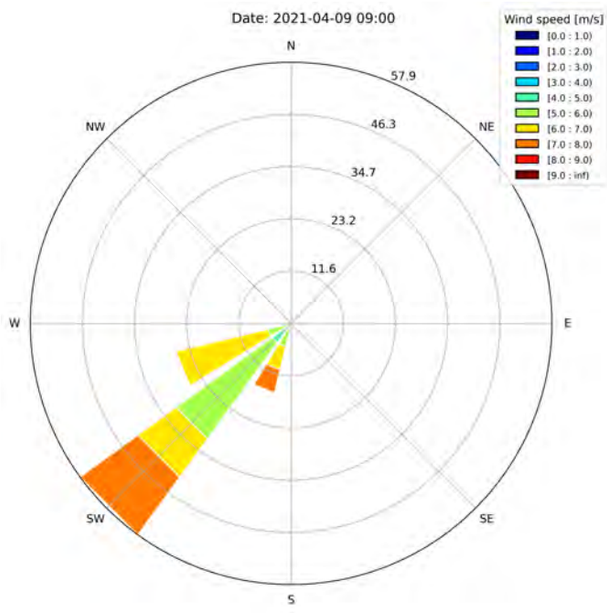

(a)

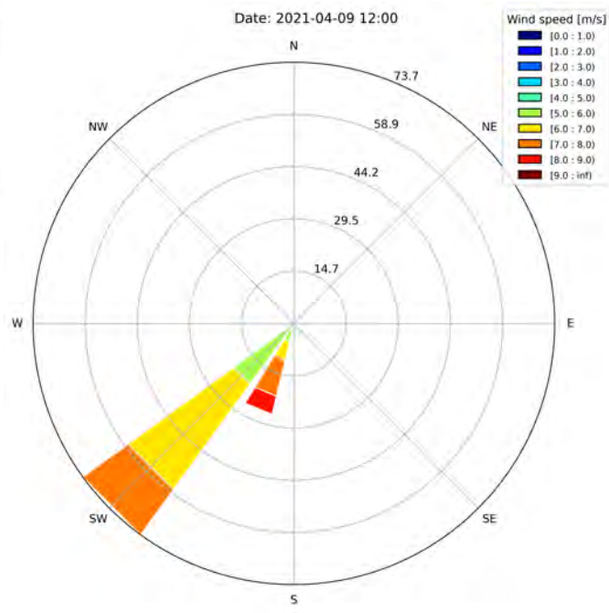

(b)

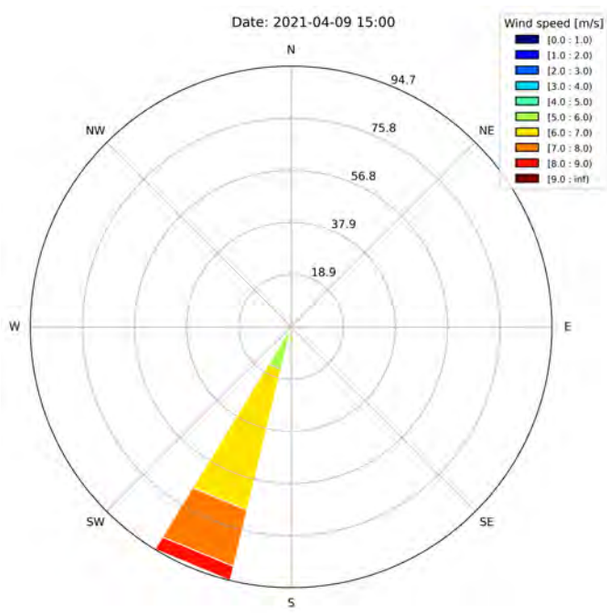

(c)

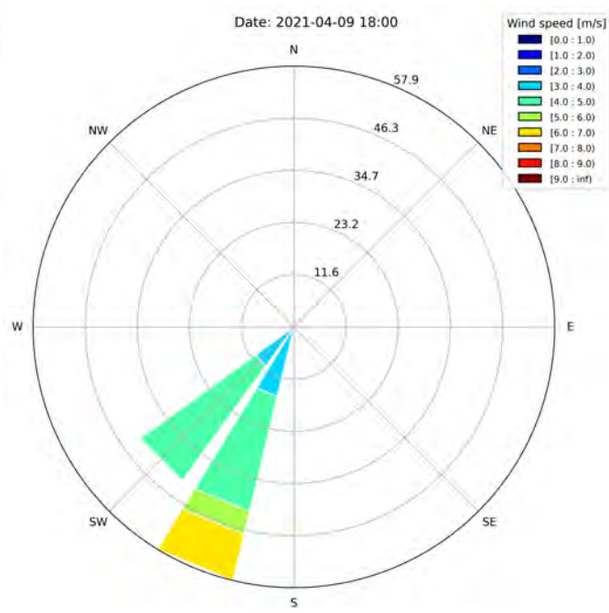

(d)

Figure 40: Same as Figures 38a-38d, but for April 9, 2021.

3.4.4 Trace gas concentration and condensation sink during new particle formation events

We investigated the relationship between the trace gas (sulfuric acid proxy) and the NPF events to understand its role in the NPF. Based on section 1.4.1.1, we expected a positive correlation of sulfuric acid proxy with NPF. Moreover, condensation sink (CS) was discussed together with the sulfuric acid proxy because sulfuric acid was considered the condensable gas in CS calculations (section 1.5.2). CS parameter was investigated in relation to NPF to analyse the efficiency of the cluster scavenging. Nonetheless, because we have no information on organic condensable vapours which may have a strong influence, our interpretations will have to remain hypothetical to a certain extent.

Similar to section 3.4.3, we used the sulfuric acid proxy and CS data between 10-14 LT (-2/+2 hours before and after, respectively, the average occurrence time of NPF events). Figures 41a and 41b present the sulfuric acid proxy and CS, respectively, for the entire studied period (October 2020 - May 2021) as mean values in the grey dots between 10 and 14 LT. The monthly mean values are plotted with a green line, representing the seasonality driven trend. We considered the trend line the threshold of our analysis. Classes I, II and III are shown in coloured circles from dark red to pink, respectively, between 10-14 LT on the occurrence day.

Regarding the sulfuric acid proxy, the NPF events occurred both below and above the threshold line. Yet, the values remained in the range of $0.2{\cdot}10^7$-$1{\cdot}10^7$ cm^{-3}. These values are high enough to trigger NPF in the atmosphere [Dada et al., 2020]. The comparison of the sulfuric acid proxy with values from different locations will be discussed in section 3.5.

Generally, NPF occurred when CS was low (smaller than ~0.002 s^{-1}). This occurrence represents an indication of efficient cluster scavenging. Low CS can support NPF in two ways. Firstly, nucleation occurs if newly produced condensable vapours are not efficiently condensing on preexisting aerosol particles thereby not limiting peak saturation values below nucleation onset. Secondly, nucleation can occur, but newly formed particles are small in number and are not efficiently collected by the background aerosols before a discernible nucleation mode can build up.

Similar to meteorological parameters (section 3.4.3), the event days did not exhibit a differentiating factor in sulfuric acid proxy and CS influence. Moreover, there were non-event days with similar values as the event days ones. This result underlines the need for a concomitant cumulus of factors in NPF, including both meteorological and trace gas data, e.g. high solar radiation, low CS. Separately, the factors cannot lead to gas-to-particle conversion and the following growth.

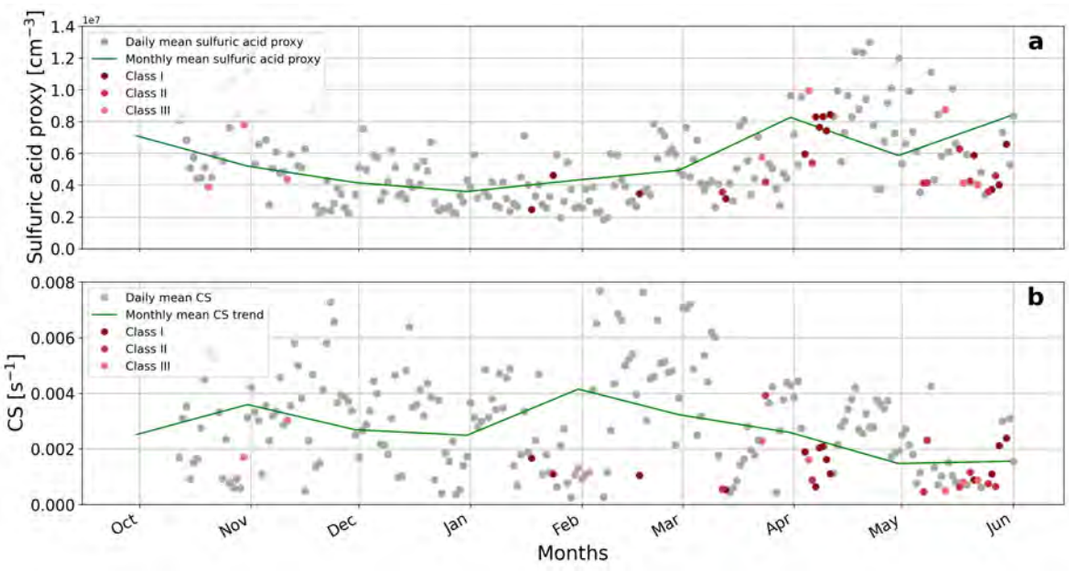

Figure 41: Same as Figure 36, but for sulfuric acid proxy and condensation sink.

Similar to section 3.4.3, Figure 42 shows an example of class I NPF event which occurred on May 28, 2021. The figure is similar to Figure 37, but the time series are plotted for sulfuric acid proxy and CS. This day constitutes an example of the values of trace gas (sulfuric acid proxy) and CS during NPF. Sulfuric acid concentrations decreased from $1{\cdot}10^7$ cm^{-3} at the start of the NPF event to $0.5{\cdot}10^7$ cm^{-3} at the end. Therefore, sulfuric acid exhibited an influence on NPF, especially on the initial nucleation rather than growth. CS showed lower values (0.0020 s^{-1}) during

NPF event compared to the rest of the day (0.0025-0.0050 s^{-1}). Low CS values supported the growth from the initial nucleation to NPF.

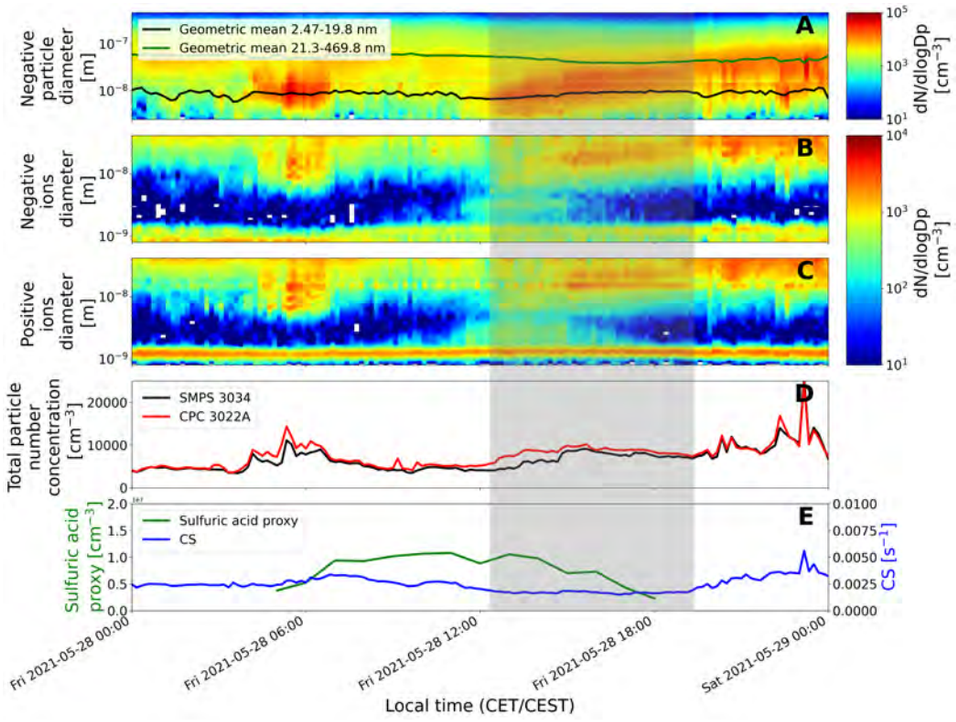

Figure 42: Same as Figure 37, but for sulfuric acid proxy and condensation sink.

3.5 Literature comparison of new particle formation

A considerable amount of literature has been published on the NPF topic. The studies comprehended several environments, e.g. semi-pristine boreal forest [Vana et al., 2016], rural [Baalbaki et al., 2020], urban [Pushpawela et al., 2018], polluted megacity [Kulmala et al., 2017], high-altitude station Jungfraujoch (JFJ) [Tröstl et al., 2016b]. From the comparison of our measurement site results with other environments, we could understand the similarities within the same environmental conditions and resemblances/dissimilarities within the different ones.

3.5.1 New particle formation events at the high-alpine site

The alpine-research station Jungfraujoch (JFJ) is a high-altitude site located in the Swiss Alps on a mountain ridge at 3580 m above sea level (a.s.l.). The site belongs to the GAW network [Bukowiecki et al., 2016], [Laj et al., 2020].

Bianchi et al. [2016] presented 1-year NPF measurements in the free troposphere at JFJ, Switzerland. As specific events, JFJ data shows three types of days and a special case. The first one is a non-event day, despite the sunny conditions. The enhancement in both small and big size particles show a vertical transport of particles to the station. The second day shows a high cloud coverage, thus a suppression of NPF due to the high condensation sink of the clouds. On both the third and special days, NPF occurred. On days like the third one, sulfuric acid concentration showed a diurnal cycle, with concentrations smaller than 10^4 and $5{\cdot}10^5$ cm^{-3} during night and day, respectively. For these concentration values, sulfuric acid cannot explain NPF at JFJ. However, NPF was linked to the high concentration of organic compounds and, thus, HOMs formed during sunny days. The fourth day with a special case had sulfuric acid concentrations up to $6{\cdot}10^6$ cm^{-3}. Only the initial GR of the event can be explained by sulfuric acid and water, assuming the condensation at the kinetic limit [Bianchi et al., 2016].

For Payerne, the sulfuric acid concentration was around $2{\cdot}10^6$ up to $1.3{\cdot}10^7$ during night and noontime, respectively. If we compare with the sulfuric acid concentrations at the JFJ [Bianchi et al., 2016], concentrations at Payerne are 10 times higher. However, they are still low compared to the chamber experiments, thus not explaining the entire NPF. Sulfuric acid may influence the initial nucleation, but not the growth [Tröstl et al., 2016a]. Even if the high solar radiation represented a meteorological condition that supported NPF at JFJ, not all days with high values presented events [Bianchi et al., 2016]. This finding was similar at Payerne. Using in situ and modelling approaches, Bianchi et al. [2016] showed that NPF in the free troposphere is dependent on the availability of highly oxidized organic species. The availability depends on previous surface contact of the air mass and the time to process the precursors from the boundary layer to the free troposphere. Because data on organic species was not available for Payerne, we could not make a comparison from this point of view.

Compared to our station, JFJ did not show a clear seasonal pattern, as is emphasized also by long-term measurements done by [Herrmann et al., 2015]. From the seasonal cycle or the absence of it, we can conclude that there are differences in the behaviour of NPF in different sites, as was suggested by [Yli-Juuti et al., 2011]. However, the GR values were in the range of 1.5-3.1 nm/h [Herrmann et al., 2015], similar to the findings for our semi-rural measurement site.

3.5.2 New particle formation events in the rural environment

Data from 16 different rural sites was analysed by Nieminen et al. [2018] in order to understand the continental boundary layer NPF. They were located at different altitudes and geographical coordinates, so the work comprehends a huge variety of meteorological and pollutants conditions.

Figure 43 presents the annual-median particle growth rates at different sites. The annual-median growth rate colour scheme goes from 2 to 8 nm/h. Payerne site is added to the map, coloured in accordance with the colour scheme. Nieminen et al. [2018] found that GRs for rural sites had a weak variability in the annual-median value and also showed a tendency to increase with NPF occurrence during summer. The annual median GR for Payerne is around 2 nm/h, which is in the lower limit range found in rural sites by Nieminen et al. [2018].

Dada et al. [2020] investigated the sources and sinks that drive sulfuric acid concentrations in different

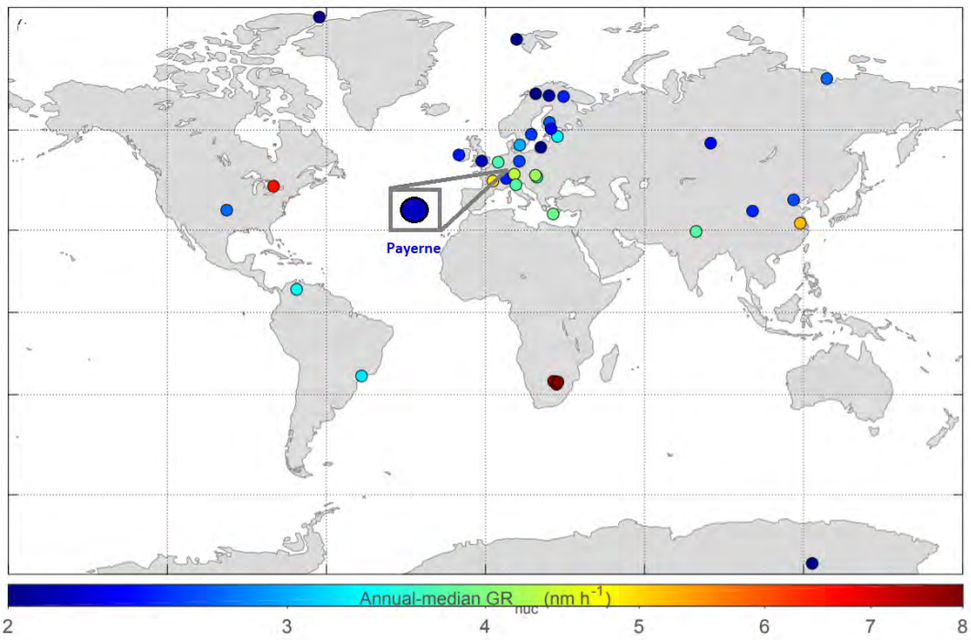

Figure 43: Annual-median particle growth rates at different measurement sites. The annual-median growth rate colour scheme goes from dark blue (2 nm/h) to dark red (8 nm/h). Payerne site is added to the map, coloured in accordance with the colour scheme. Figure adapted from Nieminen et al. [2018].

environments: boreal, rural, urban and megacity. For the analysis, Agia Marina, Cyprus was considered as the rural background site. Its location is at 532 m a.s.l. The measurements were conducted between February 22, and March 3, 2018. We used the same equation for sulfuric acid proxy derivation at the rural location 4 as is stated in [Dada et al., 2020]. Our obtained values for sulfuric acid proxy in Payerne are in the same range (10^6-10^7 cm^{-3}) as in Cyprus.

Figure 44 illustrates the characteristic predictor variables (CS [s^{-1}], SO_2 [cm^{-3}], global radiation [W/m^2]) and sulfuric acid concentration [cm^{-3}] in different types of environments. The concentrations are shown as violin plots. The white circles define the median of the distribution and the edges on the inner grey boxes refer to the 25$^{\text{th}}$ and 75$^{\text{th}}$ percentiles, respectively. For boreal and polluted megacity whole data is shown, while for rural and urban daytime data is shown (solar radiation greater than 50 Wm^2). The vertical red box shows the approximate values for Payerne. The distributions from Payerne were similar to the ones from the rural site. This result may be a confirmation of the veracity of our measurements. Besides the measurements of SO_2 and global radiation, also the calculations of CS and sulfuric acid proxy provided similar values [Dada et al., 2020].

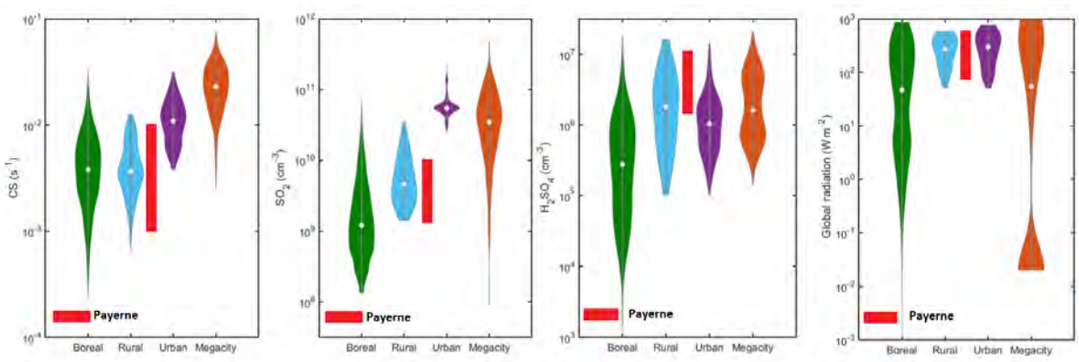

Figure 44: The characteristic predictor variables (condensation sink, SO_2, global radiation) and sulfuric acid concentration in different types of environments. The concentrations are shown as violin plots, which are a combination of boxplot and a kernel distribution function on each side of the boxplot. The white circles define the median of the distribution and the edges on the inner grey boxes refer to the 25$^{\text{th}}$ and 75$^{\text{th}}$ percentiles, respectively. For boreal and polluted megacity whole data is shown, while for rural and urban daytime data is shown (solar radiation greater than 50 Wm^2). The vertical red box shows the approximate values for Payerne. Figure adapted from [Dada et al., 2020].

3.5.3 Comparison of new particle formation events in different environments

For a comparison of our results with ones in different environments, we chose boreal forest. The station is called SMEAR II (Station for Measuring Forest Ecosystem-Atmosphere Relations II), located at 182 m a.s.l., in Southern Finland. It is classified as a rural continental site, with homogeneous boreal forest in its surroundings. The emissions of the forest are biogenic volatile organic compounds, precursors of low-volatile vapours. Due to their presence, NPF events are frequently observed, mostly in spring and autumn [Dal Maso et al., 2005].

Dal Maso et al. [2005] studied the formation and growth of atmospheric aerosols in the boreal forest for a period of 8 years. The measurements lasted for a total period of 2892 days. A total of 699 events were found during the period, meaning that on average every fourth day (24.2%) showed an event. For our site, we found lower events, around 20% of the total days presenting an event. This finding could suggest more NPF in a pristine environment compared to the rural one. However, the comparison is not done between several rural and pristine sites and our data does not comprehend an entire year, thus we cannot conclude a general finding. The finding from the Manninen et al. [2010b] from the comparison of NPF in 12 European sites showed the opposite, more NPF events in rural sites compared to pristine ones.

The GR in Payerne was lower in median value (∼2 nm/h) compared to the boreal forest value, where the 8-year measurements showed a GR of 3 nm/h. Both of the compared sites exhibited seasonal frequency, more events during spring and less in winter. The average CS during an event in boreal forest was $2.4 \cdot 10^{-3}$ s^{-1}, higher than Payerne CS ($\sim 1 \cdot 10^{-3}$ s^{-1}) [Dal Maso et al., 2005]. Vana et al. [2016] carried 2-year measurements at SMEAR II station. By looking at the seasonality, the results were similar to what was previously discussed (higher frequency of events during spring and lower during winter). The GR and CS values were reported with greater values than in Payerne, in the range of 2.2–4.7 nm/h and 3.0–6.5 $\cdot 10^{-3}$ s^{-1}, respectively. Both of the studies ([Dal Maso et al., 2005] and [Vana et al., 2016]) at the SMEAR II station were consistent and also showed a similar pattern compared to the Payerne station.

Dada et al. [2017] conducted measurements to evaluate the influence of meteorological parameters and trace gases on NPF in the boreal forest. The study combined 20 years of data collected at the SMEAR II station, with the focus on clear-sky conditions. Their results underlined that solar radiation is favourable for NPF occurrence. Moreover, very high and very low temperatures were not in favour of NPF events. However, high temperatures resulted in higher biogenic emissions, which were favourable for NPF. Regarding RH, low values correlated with NPF. The results were similar to Payerne results, with high solar radiation and temperature, and low RH raising the NPF frequency. Because of low anthropogenic traces presented in the forest, sulfuric acid concentration was usually low and did not influence NPF. In contrast, at Payerne, sulfuric acid cannot be disproved to influence NPF.

4 Conclusion and Outlook

The ultrafine particles (UFPs) (particle size smaller than 100 µm) were characterized at the rural Payerne observatory during an eight-month measurement campaign. This study set out to determine whether there are primary UPFs and/or secondary particulate matter (PM) leading to new particle formation (NPF) and to identify their potential sources. The primary focus was on their frequency of occurrence, seasonality and potential origins. Their potential sources included the main road in the southern part of the site at around 500 m and the highway and Payerne military airport in the northern part at around 4 km.

Therefore, for the distinction between the type of UFPs, size distribution measurements were conducted between 2.5 and 490 nm, including both nucleation (particle size smaller than 20 nm) and Aitken (particle size between 20 nm and 100 µm) modes. Besides the size distributions, additional measurements were used, such as PM properties (volatile particle number fraction and equivalent black carbon (eBC) mass concentration), trace gas concentrations (sulfuric acid (H_2SO_4) proxy, SO_2 and NO_x) and meteorological parameters (temperature, solar radiation, relative humidity (RH), wind direction, wind speed and precipitation). PM properties and the diurnal cycle of UFPs were used to distinguish between primary UFPs and secondary PM. Trace gas concentrations, such as sulfuric acid proxy for NPF, and SO_2 and NO_x for primary UFPs, were used to understand their role related to UFPs. Moreover, regarding the NPF analysis, the growth rate (GR) and condensation sink (CS) values were used for comparison with other measurement sites, Jungfraujoch (Switzerland), Agia Marina (Cyprus) and boreal forest (Finland).

We started our study with the analysis of the pre-existent normalized size distributions of the year 2020 measured in the range of 15-490 nm. We estimated NPF occurrence at around one per week on average. Moreover, if we excluded the months for which we do not have data, between June and September, the frequency of the events did not change. By additional size distribution data for the particle diameter in the range of 2.47-15 nm, we discovered 47 NPF events, showing the same frequency as previously mentioned. We interpret this finding as the majority of the NPF events observed in SMPS data were NPF. However, not all of the NPF events observed in SMPS data were produced by particles that nucleated at the measurement site, but also covered carried particles horizontally or vertically to the site.

To differentiate between NPF and primary UFPs, we began by analysing the diurnal cycle of volatile particle number fraction and eBC. During the colder season, the background aerosol and primary UFPs and secondary PM related to NPF exhibited similar proportions. On the other hand, in the warmer season, the volatile particle number fraction revealed two high peaks in the concentration values, one during morning rush hours (7-8 local time (LT)) and a second one in the afternoon (15-16 LT). In contrast, eBC high peaks were noticed during rush hours both in the morning and evening (18-20 LT). Comparing both diurnal cycles, an association was observed between rush hours and primary UFPs from the incomplete combustion of motor vehicles and noon-afternoon peak with NPF from the secondary PM. This result also showed that not only secondary PM related to NPF, but also primary UFPs could possess high volatility. The diurnal cycles of nucleation and Aitken modes supported the previous mentioned result, due to their peaks in the morning and evening (in the colder season) and morning and afternoon (in the warmer season).

Regarding the NPF, the seasonality analysis showed more events during the warmer season (40 events between March-May) and fewer during the colder season (7 events between October-February). Also, from the diurnal variability, the conclusion that the occurrence of NPF during noon-afternoon time is a consequence of high solar radiation, due to the OH· formation, can be drawn. Because temperature is correlated to solar radiation, NPF was also associated with high-temperature values, even if the higher temperature should a priori counteract NPF. Relative humidity showed an anticorrelation with NPF. The wind speed varied, with both low and high values, while the wind direction showed that the potential sources of NPF were located to the northern and southern of the station. Although the mentioned values of meteorological parameters represented favourable conditions for NPF enhancement, they did not always trigger NPF.

The investigation related to trace gas concentration revealed that NPF primarily occurred on days with both above- and below-average H_2SO_4 proxy. Yet, based on Dada et al. [2020], the values were in a range that could trigger NPF, underlying that a potential sulfuric acid proxy influence on NPF cannot be excluded. CS values

were lower, suggesting that the clusters are scavenged only by a small fraction of particles, and were comparable to literature values. The atmospheric conditions were not favourable for high GR, as values of 2 nm/h were shown, but they were in a similar range found in other rural environments.

Other significant findings to emerge from this study are related to primary UFPs. As it was previously mentioned, the time period of morning and evening rush hours was associated with primary UFPs from on-going vehicles. The analysis of the total particle number concentration in relation to wind direction highlighted a slight influence of the wind on our measurement site. Despite this, we took into account wind direction as a guide in distinguishing between potential source locations, airport and highway in the north and main road in the south.

Further examination was conducted to determine the influence of non-volatile UFPs on the total UFPs. The study was carried on over a period of five days. Our starting hypothesis claimed that the soot particles in the Aitken ranges (particle sizes between 20 nm and 100 µm) are related to diesel car engines while the nucleation mode particles (smaller than 20 nm) have the gas turbine aeroplanes as a source. However, the hypothesis was contradicted and the reasons could have been several. A potential explanation is that either Diesel Particulate Filters or Gasoline Direct-Injection engines could move the Aitken size non-volatile particles to the edge of nucleation mode. During the days with non-volatile nucleation mode particles, wind direction marked both north and south as potential source locations, promoting both on-road traffic and gas turbine aeroplanes as possible origins. For those days, enhanced NO_x concentrations and both high and low SO_2 concentrations supported the sources being gas turbine aeroplanes and on-road cars, respectively. Because the investigation regarding the sources of primary UFPs was concluded for a short time, for a better-grounded conclusion, more research is required to assess the sources of primary UFPs, including additional data of the airport flights daily schedule.

As future outlook for improving the understanding of UFP sources and NPF events, there are several measurement ideas to be implemented. First of all, we found clear signs of a distinct seasonality. However, achieving robust statistics and seasonally dependent frequency of occurrence would require long-term measurements ([Hari and Kulmala, 2005], [Manninen, 2011]). To further this goal, the necessary data can be gathered if a permanent observation site is established. Data from multiple stations together with the data from the Payerne observation site can then be consolidated in a single large database and used for comparative analyses. Such efforts are currently undertaken as Payerne becomes part of international research infrastructure, ACTRIS (Aerosols, Clouds, and Trace gases Research Infrastructure Network).

Further, to understand the chemical composition of the UFPs, a mass spectrometer can be used, e.g. APi-ToF (Atmospheric Pressure interface Time of Flight Mass Spectrometer). Because APi-ToF has high sensitivity and resolution, it can provide information about the initial steps of nucleation. Because the initial nucleation can be due to sulfuric acid and growth due to Highly-Oxygenated organic Molecules (HOMs), both should be studied. For NPF events, a volatility distribution could be used to distinguish between different organic compounds (ultra-low volatile organic compounds (ULVOC), extremely low-volatile organic compounds (ELVOC), low-volatile organic compounds (LVOC) and semi-volatile organic compounds (SVOC)), as it was previously done in [Chen et al., 2019].

From the analysis point of view, the separation between weekdays and weekends could help to understand the influence of primary traffic-induced UFPs. Airport influence could be better accounted for by taking into consideration flight schedule information. A long-term statistic using particle size information below 20 nm, wind direction and wind speed could add information about the frequency of occurrence of gas turbine particles. Additionally, the morning and evening evolution of UFPs could also be interpreted by boundary layer measurements. From the NPF perspective, further developments could be made by automatizing the detection of the events using machine learning. Up to now, Joutsensaari et al. [2018] realized an automatic classification of the events using deep learning.

The presence of UFPs represents a health threat for the population. Because of UFPs were found in Payerne, another topic for further studies would be to determine if the analysed concentrations are at a relevant level for health concerns.

Glossary

Notation	Definition
Aerodynamic diameter	Diameter of a sphere particle with density equal to 1 g·cm^{-3}, having the same settling velocity as the particle [Seinfeld and Pandis, 2006].
Aerosol cluster	Finite-size system made of different types of particulate matter.
Atmospheric ions	Naturally electrically charged molecules or atoms in the atmosphere [Jiang et al., 2018].
Atmospheric particles	Neutral molecules or atoms in the atmosphere.
Event day	A day when a new particle formation event occurs.
Hygroscopicity	Ability to absorb water by soluble substances.
Negative ions	Molecules or atoms that gained one or more electrons.
Negative particles	Neutral particles that are negatively charged using NAIS instrument.
New particle formation	Cluster formation from precursor gases by nucleation and subsequent growth of clusters to stable new particles [Lee et al., 2019].
New particle formation event	New particle formation that occurred between a specific time period.
Non-event day	A day when no new particle formation event occurs.
Normalized size distribution	Size distribution of particles in a size bin divided by the width of this bin.
Particulate matter	"A suspension of fine solid or liquid particles in a gas (...) that ranges in size from a few nanometres (nm) to tens of micrometres (µm) in diameter" [Seinfeld and Pandis, 2006, p. 55].
Positive ions	Molecules or atoms that lost one or more electrons.
Probability density function	Probability distribution of a random variable to be found in a specific interval.
Relative humidity	Percentage of amount of water in the air in relation to the maximum amount of water vapor that could be held at its current temperature.
Ultrafine particles	Particles smaller than 0.1 µm in aerodynamic diameter [Seinfeld and Pandis, 2006].

Bibliography

I. A. P. BUCK. Mini-BUCK Calibrator M-5, 2017. URL https://www.apbuck.com/shop/item.aspx?itemid=18.

Airel. Neutral cluster and Air Ion Spectrometer (NAIS) - Operation and Service Manual. 2015.

J. Alanen, P. Simonen, S. Saarikoski, H. Timonen, O. Kangasniemi, E. Saukko, R. Hillamo, K. Lehtoranta, T. Murtonen, H. Vesala, J. Keskinen, and T. Rönkkö. Comparison of primary and secondary particle formation from natural gas engine exhaust and of their volatility characteristics. *Atmos. Chem. Phys*, 17:8739–8755, 2017. doi: 10.5194/acp-17-8739-2017. URL https://doi.org/10.5194/acp-17-8739-2017.

C. Allouis, F. Beretta, P. Minutolo, R. Pagliara, M. Sirignano, L. Sgro, and A. D'Anna. Measurements of ultrafine particles from a gas-turbine burning biofuels. *Experimental Thermal and Fluid Science*, 34(3):258–261, 2010. doi: https://doi.org/10.1016/j.expthermflusci.2009.10.034. URL https://www.sciencedirect.com/science/article/pii/S0894177709001897. Sixth Mediterranean Combustion Symposium.

J. Almeida, S. Schobesberger, A. Kürten, I. K. Ortega, O. Kupiainen-Määttä, A. P. Praplan, A. Adamov, A. Amorim, F. Bianchi, M. Breitenlechner, A. David, J. Dommen, N. M. Donahue, A. Downard, E. Dunne, J. Duplissy, S. Ehrhart, R. C. Flagan, A. Franchin, R. Guida, J. Hakala, A. Hansel, M. Heinritzi, H. Henschel, T. Jokinen, H. Junninen, M. Kajos, J. Kangasluoma, H. Keskinen, A. Kupc, T. Kurtén, A. N. Kvashin, A. Laaksonen, K. Lehtipalo, M. Leiminger, J. Leppä, V. Loukonen, V. Makhmutov, S. Mathot, M. J. McGrath, T. Nieminen, T. Olenius, A. Onnela, T. Petäjä, F. Riccobono, I. Riipinen, M. Rissanen, L. Rondo, T. Ruuskanen, F. D. Santos, N. Sarnela, S. Schallhart, R. Schnitzhofer, J. H. Seinfeld, M. Simon, M. Sipilä, Y. Stozhkov, F. Stratmann, A. Tomé, J. Tröstl, G. Tsagkogeorgas, P. Vaattovaara, Y. Viisanen, A. Virtanen, A. Vrtala, P. E. Wagner, E. Weingartner, H. Wex, C. Williamson, D. Wimmer, P. Ye, T. Yli-Juuti, K. S. Carslaw, M. Kulmala, J. Curtius, U. Baltensperger, D. R. Worsnop, H. Vehkamäki, and J. Kirkby. Molecular understanding of sulphuric acid-amine particle nucleation in the atmosphere. *Nature*, 502(7471):359–363, 2013. doi: 10.1038/nature12663. URL https://www.nature.com/articles/nature12663.

Z. An, R.-J. Huang, R. Zhang, X. Tie, G. Li, J. Cao, W. Zhou, Z. Shi, Y. Han, Z. Gu, and Y. Ji. Severe haze in northern China: A synergy of anthropogenic emissions and atmospheric processes. *Proceedings of the National Academy of Sciences of the United States of America*, 116(18):8666, 2019. doi: 10.1073/PNAS.1900125116. URL /pmc/articles/PMC6500134//pmc/articles/PMC6500134/?report=abstracthttps://www.ncbi.nlm.nih.gov/pmc/articles/PMC6500134/.

R. Baalbaki, M. Pikridas, T. Jokinen, T. Laurila, L. Dada, S. Bezantakos, L. Ahonen, K. Neitola, A. Maisser, E. Bimenyimana, A. Christodoulou, F. Unga, C. Savvides, K. Lehtipalo, J. Kangasluoma, G. Biskos, T. Petäjä, V.-M. Kerminen, J. Sciare, and M. Kulmala. Towards understanding the mechanisms of new particle formation in the Eastern Mediterranean. *Atmospheric Chemistry and Physics Discussions*, (11):1–44, 2020. doi: 10.5194/acp-2020-1066.

U. Baltensperger, N. Streit, E. Weingartner, S. Nyeki, A. S. Prévôt, R. Van Dingenen, A. Virkkula, J. P. Putaud, A. Even, H. Ten Brink, A. Blatter, A. Neftel, and H. W. Gäggeler. Urban and rural aerosol characterization of summer smog events during the PIPAPO field campaign in Milan, Italy. *Journal of Geophysical Research Atmospheres*, 107(22), 2002. doi: 10.1029/2001JD001292.

T. Berndt, F. Stratmann, M. Sipilä, J. Vanhanen, T. Petäjä, J. Mikkilä, A. Grüner, G. Grüner, G. Spindler, R. Lee, M. Iii, J. Curtius, M. Kulmala, and J. Heintzenberg. Laboratory study on new particle formation from the reaction OH + SO2 : influence of experimental conditions, H 2 O vapour, NH 3 and the amine tert-butylamine on the overall process. *Atmospheric Chemistry and Physics*, 10:7101–7116, 2010. doi: 10.5194/acp-10-7101-2010. URL www.atmos-chem-phys.net/10/7101/2010/.

F. Bianchi, J. Tröstl, H. Junninen, C. Frege, S. Henne, C. R. Hoyle, U. Molteni, E. Herrmann, A. Adamov, N. Bukowiecki, X. Chen, J. Duplissy, M. Gysel, M. Hutterli, J. Kangasluoma, J. Kontkanen, A. Kürten, H. E. Manninen, S. Münch, O. Peräkylä, T. Petäjä, L. Rondo, C. Williamson, E. Weingartner, J. Curtius, D. R. Worsnop, M. Kulmala, J. Dommen, and U. Baltensperger. New particle formation in the free troposphere: A question of chemistry and timing. *Science*, 352(6289):1109–1112, 2016. doi: 10.1126/science.aad5456.

F. Bianchi, T. Kurtén, M. Riva, C. Mohr, M. P. Rissanen, P. Roldin, T. Berndt, J. D. Crounse, P. O. Wennberg, T. F. Mentel, J. Wildt, H. Junninen, T. Jokinen, M. Kulmala, D. R. Worsnop, J. A. Thornton, N. Donahue, H. G. Kjaergaard, and M. Ehn. Highly Oxygenated Organic Molecules (HOM) from gas-phase autoxidation involving peroxy radicals: A key contributor to atmospheric aerosol. *Chemical Reviews*, 119(6):3472–3509, 2019. doi: 10.1021/ACS.CHEMREV.8B00395. URL https://pubs.acs.org/doi/abs/10.1021/acs.chemrev.8b00395.

M. Brines, M. Dall'Osto, D. C. Beddows, R. M. Harrison, F. Gómez-Moreno, L. Núñez, B. Artíñano, F. Costabile, G. P. Gobbi, F. Salimi, L. Morawska, C. Sioutas, and X. Querol. Traffic and nucleation events as main sources of ultrafine particles in high-insolation developed world cities. *Atmospheric Chemistry and Physics*, 15(10):5929–5945, 2015. doi: 10.5194/ACP-15-5929-2015.

N. Bukowiecki, E. Weingartner, M. Gysel, M. Collaud Coen, P. Zieger, E. Herrmann, M. Steinbacher, H. W. Gäggeler, and U. Baltensperger. A review of more than 20 years of aerosol observation at the high altitude research station Jungfraujoch, Switzerland (3580 m asl). *Aerosol and Air Quality Research*, 16:764–788, 2016. doi: 10.4209/aaqr.2015.05.0305. URL http://www.hfsjg.ch.

K. P. Cain, E. Karnezi, and S. N. Pandis. Challenges in determining atmospheric organic aerosol volatility distributions using thermal evaporation techniques. *https://doi.org/10.1080/02786826.2020.1748172*, 54(8):941–957, 2020. doi: 10.1080/02786826.2020.1748172. URL https://www.tandfonline.com/doi/abs/10.1080/02786826.2020.1748172.

G. R. Cass, L. A. Hughes, P. Bhave, M. J. Kleeman, J. O. Allen, and L. G. Salmon. The chemical composition of atmospheric ultrafine particles. *Philosophical Transactions: Mathematical, Physical and Engineering Sciences*, 358 (1775):2581–2592, 2000. URL http://www.jstor.org/stable/2666941.

G. Catalytic Instruments. Model CS015 Catalytic Stripper, 2020. URL https://catalytic-instruments.com/product/cs015/.

X. Chen, W. Yang, Z. Wang, J. Li, M. Hu, J. An, Q. Wu, Z. Wang, H. Chen, Y. Wei, H. Du, and D. Wang. Improving new particle formation simulation by coupling a volatility-basis set (VBS) organic aerosol module in NAQPMS+APM. *Atmospheric Environment*, 204:1–11, 2019. doi: 10.1016/J.ATMOSENV.2019.01.053.

H. C. Cheung, L. Morawska, and Z. D. Ristovski. Observation of new particle formation in subtropical urban environment. *Atmospheric Chemistry and Physics*, 11(8):3823–3833, 2011. doi: 10.5194/acp-11-3823-2011. URL https://acp.copernicus.org/articles/11/3823/2011/.

R. Chirico, P. F. Decarlo, M. F. Heringa, T. Tritscher, R. Richter, A. S. H. Prévôt, J. Dommen, E. Weingartner, G. Wehrle, M. Gysel, M. Laborde, and U. Baltensperger. Impact of aftertreatment devices on primary emissions and secondary organic aerosol formation potential from in-use diesel vehicles: results from smog chamber experiments. *Atmospheric Chemistry and Physics*, 10:11545–11563, 2010. doi: 10.5194/acp-10-11545-2010. URL www.atmos-chem-phys.net/10/11545/2010/.

J. Curtius. Nucleation of atmospheric aerosol particles. *Comptes Rendus Physique*, 7(9-10):1027–1045, 2006. doi: 10.1016/j.crhy.2006.10.018.

L. Dada, P. Paasonen, T. Nieminen, S. Buenrostro Mazon, J. Kontkanen, O. Peräkylä, K. Lehtipalo, T. Hussein, T. Petäjä, V. M. Kerminen, J. Bäck, and M. Kulmala. Long-term analysis of clear-sky new particle formation events and nonevents in Hyytiälä. *Atmospheric Chemistry and Physics*, 17(10):6227–6241, 2017. doi: 10.5194/acp-17-6227-2017. URL www.atmos-chem-phys.net/17/6227/2017/.

L. Dada, R. Chellapermal, S. Buenrostro Mazon, P. Paasonen, J. Lampilahti, H. E Manninen, H. Junninen, T. Petäjä, V. M. Kerminen, and M. Kulmala. Refined classification and characterization of atmospheric new-particle formation events using air ions. *Atmospheric Chemistry and Physics*, 18(24):17883–17893, 2018. doi: 10.5194/acp-18-17883-2018.

L. Dada, I. Ylivinkka, R. Baalbaki, C. Li, Y. Guo, C. Yan, L. Yao, N. Sarnela, T. Jokinen, K. R. Daellenbach, R. Yin, C. Deng, B. Chu, T. Nieminen, Y. Wang, Z. Lin, R. C. Thakur, J. Kontkanen, D. Stolzenburg, M. Sipilä, T. Hussein, P. Paasonen, F. Bianchi, I. Salma, T. Weidinger, M. Pikridas, J. Sciare, J. Jiang, Y. Liu, T. Petäjä, V.-M. Kerminen, and M. Kulmala. Sources and sinks driving sulfuric acid concentrations in contrasting environments: implications on proxy calculations. *Atmospheric Chemistry and Physics*, 20:11747–11766, 2020. doi: 10.5194/acp-20-11747-2020. URL https://doi.org/10.5194/acp-20-11747-2020.

M. Dal Maso. Condensation and coagulation sinks and formation of nucleation mode particles in coastal and boreal forest boundary layers. *Journal of Geophysical Research*, 107(D19):8097, 2002. doi: 10.1029/2001JD001053. URL http://doi.wiley.com/10.1029/2001JD001053.

M. Dal Maso, M. Kulmala, I. Riipinen, R. Wagner, T. Hussein, P. P. Aalto, and K. E. Lehtinen. Formation and growth of fresh atmospheric aerosols: Eight years of aerosol size distribution data from SMEAR II, Hyytiälä, Finland. *Boreal Environment Research*, 10(5):323–336, 2005.

D. W. Dockery, C. A. Pope, X. Xu, J. D. Spengler, J. H. Ware, M. E. Fay, B. G. J. Ferris, and F. E. Speizer. An association between air pollution and mortality in six U.S. cities. *The New England Journal of Medicine*, 329(24):1753–1759, 2010. doi: 10.1056/NEJM199312093292401. URL https://www.nejm.org/doi/10.1056/NEJM199312093292401.

L. Durdina, B. T. Brem, A. Setyan, F. Siegerist, T. Rindlisbacher, and J. Wang. Assessment of Particle Pollution from Jetliners: from Smoke Visibility to Nanoparticle Counting. *Environmental Science Technology*, 2017. doi: 10.1021/acs.est.6b05801. URL https://pubs.acs.org/sharingguidelines.

F. L. Eisele, E. R. Lovejoy, E. Kosciuch, K. F. Moore, R. L. Mauldin, J. N. Smith, P. H. McMurry, and K. Iida. Negative atmospheric ions and their potential role in ion-induced nucleation. *Journal of Geophysical Research: Atmospheres*, 111(D4):4305, 2006. doi: 10.1029/2005JD006568. URL https://onlinelibrary.wiley.com/doi/full/10.1029/2005JD006568https://onlinelibrary.wiley.com/doi/abs/10.1029/2005JD006568https://agupubs.onlinelibrary.wiley.com/doi/10.1029/2005JD006568.

E. Emanuelsson. *Formation, Ageing and Thermal Properties of Secondary Organic Aerosol*. Number 5. 2013. ISBN 9789162886202. URL https://gupea.ub.gu.se/handle/2077/31839%5Cnhttp://hdl.handle.net/2077/31839.

D. K. Farmer, E. K. Boedicker, and H. M. Debolt. Dry deposition of atmospheric aerosols: Approaches, observations, and mechanisms. *Annual Review of Physical Chemistry*, 2021. doi: 10.1146/annurev-physchem-090519. URL https://doi.org/10.1146/annurev-physchem-090519-.

S. Freeman, D. S. Lee, L. L. Lim, A. Skowron, and R. R. D. León. Trading off aircraft fuel burn and NOx emissions for optimal climate policy. *Environmental Science Technology*, 52(5):2498–2505, 2018. doi: 10.1021/ACS.EST.7B05719. URL https://pubs.acs.org/doi/full/10.1021/acs.est.7b05719.

N. Fuchs and A. Sutugin. High-dispersed aerosols. In *Topics in Current Aerosol Research*, page 1. Elsevier, 1971.

S. Fuzzi, U. Baltensperger, K. Carslaw, S. Decesari, H. Denier Van Der Gon, M. C. Facchini, D. Fowler, I. Koren, B. Langford, U. Lohmann, E. Nemitz, S. Pandis, I. Riipinen, Y. Rudich, M. Schaap, J. G. Slowik, D. V. Spracklen, E. Vignati, M. Wild, M. Williams, and S. Gilardoni. Particulate matter, air quality and climate: Lessons learned and future needs. *Atmospheric Chemistry and Physics*, 15(14):8217–8299, 2015. doi: 10.5194/acp-15-8217-2015.

R. Gieré and X. Querol. Soli Particulate Matter in the atmosphere. *Elements*, 6:215–222, 2010. doi: 10.2113/gselements.6.4.215.

S. G. Gonser, F. Klein, W. Birmili, J. Größ, M. Kulmala, H. E. Manninen, A. Wiedensohler, and A. Held. Ion-particle interactions during particle formation and growth at a coniferous forest site in central Europe. *Atmospheric Chemistry and Physics*, 14(19):10547–10563, 2014. doi: 10.5194/acp-14-10547-2014.

A. Hamed, H. Korhonen, S. L. Sihto, J. Joutsensaari, H. Jrvinen, T. Petäjä, F. Arnold, T. Nieminen, M. Kulmala, J. N. Smith, K. E. Lehtinen, and A. Laaksonen. The role of relative humidity in continental new particle formation. *Journal of Geophysical Research Atmospheres*, 116(3):3202, 2011. doi: 10.1029/2010JD014186. URL https://agupubs.onlinelibrary.wiley.com/doi/full/10.1029/2010JD014186https://agupubs.onlinelibrary.wiley.com/doi/abs/10.1029/2010JD014186https://agupubs.onlinelibrary.wiley.com/doi/10.1029/2010JD014186.

E. Hammer, N. Bukowiecki, M. Gysel, Z. Jurányi, C. R. Hoyle, R. Vogt, U. Baltensperger, and E. Weingartner. Investigation of the effective peak supersaturation for liquid-phase clouds at the high-alpine site Jungfraujoch, Switzerland (3580 m a.s.l.). *Atmospheric Chemistry and Physics*, 14:1123–1139, 2014. doi: 10.5194/acp-14-1123-2014. URL www.atmos-chem-phys.net/14/1123/2014/.

P. Hari and M. Kulmala. Station for measuring ecosystem-atmosphere relations (SMEAR II). *Boreal Environment Research*, 2005. URL https://www.researchgate.net/publication/237563032_Station_for_measuring_Ecosystem-Atmosphere_relations_SMEAR_II.

J. Haywood. Atmospheric Aerosols and Their Role in Climate Change. In *Climate Change: Observed Impacts on Planet Earth: Second Edition*, pages 449–463. Elsevier Inc., 2016. ISBN 9780444635242. doi: 10.1016/B978-0-444-63524-2.00027-0.

E. Herrmann, E. Weingartner, S. Henne, L. Vuilleumier, N. Bukowiecki, M. Steinbacher, F. Conen, M. C. Coen, E. Hammer, Z. Jurányi, U. Baltensperger, and M. Gysel. Analysis of long-term aerosol size distribution data from Jungfraujoch with emphasis on free tropospheric conditions, cloud influence, and air mass transport. *Journal of Geophysical Research: Atmospheres*, 120(18):9459–9480, 2015. doi: 10.1002/2015JD023660. URL https://agupubs.onlinelibrary.wiley.com/doi/full/10.1002/2015JD023660https://agupubs.onlinelibrary.wiley.com/doi/abs/10.1002/2015JD023660https://agupubs.onlinelibrary.wiley.com/doi/10.1002/2015JD023660.

C. Hüglin, S. K. Grange, B. G. Purghart, R. Weber, and R. Ballaman. Chemical characterisation and source identification of PM 10 and PM 2.5 in Switzerland-Project report-View of the urban air quality monitoring station Zürich-Kaserne from above. Project monitoring FOEN, Air Quality Management Section. Technical report.

IPCC. 2013: Anthropogenic and Natural Radiative Forcing. In T. Stocker, D. Qin, G.-K. Plattner, M. Tignor, S. Allen, J. Boschung, A. Nauels, Y. Xia, V. Bex, and P. Midgley, editors, *Climate Change 2013: The Physical Science Basis. Contribution of Working Group I to the Fifth Assessment Report of the Intergovernmental Panel on Climate Change*, chapter 8. Cambridge University Press, Cambridge, United Kingdom and New York, NY, USA, 2013.

S.-Y. Jiang, A. Ma, and S. Ramachandran. Negative air ions and their effects on human health and air quality improvement. *International Journal of Molecular Sciences*, 19(10), 2018. doi: 10.3390/IJMS19102966. URL /pmc/articles/PMC6213340//pmc/articles/PMC6213340/?report=abstracthttps://www.ncbi.nlm.nih.gov/pmc/articles/PMC6213340/.

J. Joutsensaari, M. Ozon, T. Nieminen, S. Mikkonen, T. Lähivaara, S. Decesari, M. C. Facchini, A. Laaksonen, and K. E. Lehtinen. Identification of new particle formation events with deep learning. *Atmospheric Chemistry and Physics*, 18(13):9597–9615, 2018. doi: 10.5194/ACP-18-9597-2018.

V. I. Kalilmanov. *Lecture Notes in Physics - Nucleation Theory*, volume 860. Springer, 2013. URL http://www.springer.com/series/5304.

G. Kamita, B. Frka-Petesic, A. Allard, M. Dargaud, K. King, A. G. Dumanli, and S. Vignolini. Biocompatible and Sustainable Optical Strain Sensors for Large-Area Applications. *Advanced Optical Materials*, 4(12):1950–1954, 2016. doi: 10.1002/adom.201600451.

K. Kim, D. Woo, J. H. Park, S. G. Doo, and T. Kim. Formation of silicon nanoparticles using SiH 4 pyrolysis at atmospheric- and low-pressure. *Journal of the Korean Physical Society*, 54(3):1021–1026, 2009. doi: 10.3938/jkps.54.1021.

K. H. Kim, S. B. Lee, D. Woo, and G. N. Bae. Influence of wind direction and speed on the transport of particle-bound PAHs in a roadway environment. *Atmospheric Pollution Research*, 6(6):1024–1034, 2015. doi: 10.1016/J.APR.2015.05.007.

C. Kuang. Condensation Particle Counter instrument handbook. Technical report, 2016. URL https://www.osti.gov/servlets/purl/1245983/.

M. Kulmala, M. Dal Maso, J. M. Mäkelä, L. Pirjola, M. Väkevä, P. Aalto, P. Miikkulainen, K. Hämeri, C. D. O'dowd, J. M. Ma¨kela¨, M. Ma¨kela, M. Ma¨kela¨, M. Va¨keva¨, Va¨, V. Va¨keva¨, P. Aalto, Va¨keva¨, K. Ha¨meri, and H. Ha¨meri. On the formation, growth and composition of nucleation mode particles. *Tellus B: Chemical and Physical Meteorology*, 53(4):479–490, 2001. doi: 10.3402/tellusb.v53i4.16622. URL https://www.tandfonline.com/action/journalInformation?journalCode=zelb20.

M. Kulmala, L. Laakso, K. E. J. Lehtinen, I. Riipinen, M. Dal Maso, T. Anttila, V.-M. Kerminen, U. Hõrrak, M. Vana, and H. Tammet. Initial steps of aerosol growth. *Atmospheric Chemistry and Physics*, 4(11/12):2553–2560, 2004a. doi: 10.5194/acp-4-2553-2004.

M. Kulmala, H. Vehkamäki, T. Petäjä, M. Dal Maso, A. Lauri, V. M. Kerminen, W. Birmili, and P. H. McMurry. Formation and growth rates of ultrafine atmospheric particles: a review of observations. *Journal of Aerosol Science*, 35(2):143–176, 2004b. doi: 10.1016/J.JAEROSCI.2003.10.003.

M. Kulmala, T. Petäjä, T. Nieminen, M. Sipilä, H. E. Manninen, K. Lehtipalo, M. Dal Maso, P. P. Aalto, H. Junninen, P. Paasonen, I. Riipinen, K. E. Lehtinen, A. Laaksonen, and V. M. Kerminen. Measurement of the nucleation of atmospheric aerosol particles. *Nature Protocols*, 7(9):1651–1667, 2012. doi: 10.1038/nprot.2012.091.

M. Kulmala, V.-M. Kerminen, T. Petäjä, A. J. Ding, and L. Wang. Atmospheric gas-to-particle conversion: why NPF events are observed in megacities? *Faraday Discussions*, 200(0):271–288, 2017. doi: 10.1039/C6FD00257A. URL `https://pubs.rsc.org/en/content/articlehtml/2017/fd/c6fd00257ahttps://pubs.rsc.org/en/content/articlelanding/2017/fd/c6fd00257a`.

T. Kurtén, V. Loukonen, H. Vehkamäki, and M. Kulmala. Amines are likely to enhance neutral and ion-induced sulfuric acid-water nucleation in the atmosphere more effectively than ammonia. *Atmospheric Chemistry and Physics*, 8(14):4095–4103, 2008. doi: 10.5194/acp-8-4095-2008. URL `https://acp.copernicus.org/articles/8/4095/2008/`.

P. Laj, A. Bigi, C. Rose, E. Andrews, C. Lund Myhre, M. Collaud Coen, Y. Lin, A. Wiedensohler, M. Schulz, J. A. Ogren, M. Fiebig, J. Gliß, A. Mortier, M. Pandolfi, T. Petäja, S. W. Kim, W. Aas, J. P. Putaud, O. Mayol-Bracero, M. Keywood, L. Labrador, P. Aalto, E. Ahlberg, L. Alados Arboledas, A. Alastuey, M. Andrade, B. Artinano, S. Ausmeel, T. Arsov, E. Asmi, J. Backman, U. Baltensperger, S. Bastian, O. Bath, J. Paul Beukes, B. T. Brem, N. Bukowiecki, S. Conil, C. Couret, D. Day, W. Dayantolis, A. Degorska, K. Eleftheriadis, P. Fetfatzis, O. Favez, H. Flentje, M. I. Gini, A. Gregorič, M. Gysel-Beer, A. Gannet Hallar, J. Hand, A. Hoffer, C. Hueglin, R. K. Hooda, A. Hyvärinen, I. Kalapov, N. Kalivitis, A. Kasper-Giebl, J. Eun Kim, G. Kouvarakis, I. Kranjc, R. Krejci, M. Kulmala, C. Labuschagne, H. J. Lee, H. Lihavainen, N. H. Lin, G. Löschau, K. Luoma, A. Marinoni, S. Martins Dos Santos, F. Meinhardt, M. Merkel, J. M. Metzger, N. Mihalopoulos, N. Anh Nguyen, J. Ondracek, N. Pérez, M. Rita Perrone, J. M. Pichon, D. Picard, J. M. Pichon, V. Pont, N. Prats, A. Prenni, F. Reisen, S. Romano, K. Sellegri, S. Sharma, G. Schauer, P. Sheridan, J. Patrick Sherman, M. Schütze, A. Schwerin, R. Sohmer, M. Sorribas, M. Steinbacher, J. Sun, G. Titos, B. Toczko, T. Tuch, P. Tulet, P. Tunved, V. Vakkari, F. Velarde, P. Velasquez, P. Villani, S. Vratolis, S. H. Wang, K. Weinhold, R. Weller, M. Yela, J. Yus-Diez, V. Zdimal, P. Zieger, and N. Zikova. A global analysis of climate-relevant aerosol properties retrieved from the network of Global Atmosphere Watch (GAW) near-surface observatories. *Atmospheric Measurement Techniques*, 13(8):4353–4392, 2020. doi: 10.5194/AMT-13-4353-2020.

M. Lajili. Assessments of gaseous and particulate matter emissions from biomass combustion and their effect on human health energy conversion of lignocellulosic biomass using heat processes view project assessments of gaseous and particulate matter emissions from biomass combustion and their effect on human health. *Journal of Scientific Technical Research*, 2019. doi: 10.26717/BJSTR.2019.17.002979. URL `https://www.researchgate.net/publication/332571957`.

D. S. Lee, G. Pitari, V. Grewe, K. Gierens, J. E. Penner, A. Petzold, M. J. Prather, U. Schumann, A. Bais, T. Berntsen, D. Iachetti, L. L. Lim, and R. Sausen. Transport impacts on atmosphere and climate: Aviation. *Atmospheric Environment*, 44:4678–4734, 2010. doi: 10.1016/j.atmosenv.2009.06.005. URL `http://www.icas2006.org/index2.php,`.

S. H. Lee, H. Gordon, H. Yu, K. Lehtipalo, R. Haley, Y. Li, and R. Zhang. New particle formation in the atmosphere: From molecular clusters to global climate. *Journal of Geophysical Research: Atmospheres*, 124(13):7098–7146, 2019. doi: 10.1029/2018JD029356.

J. Liggio, M. Gordon, G. Smallwood, S.-M. Li, C. Stroud, R. Staebler, G. Lu, P. Lee, B. Taylor, and J. R. Brook. Are emissions of black carbon from gasoline vehicles underestimated? Insights from near and on-road measurements. *Environmental ScienceTechnology*, pages 4819–4828, 2012. doi: dx.doi.org/10.1021/es2033845. URL `https://pubs.acs.org/doi/pdf/10.1021/es2033845`.

E. R. Lovejoy, J. Curtius, and K. D. Froyd. Atmospheric ion-induced nucleation of sulfuric acid and water. *Journal of Geophysical Research: Atmospheres*, 109(D8):8204, 2004. doi: 10.1029/2003JD004460. URL `https://onlinelibrary.wiley.com/doi/full/10.1029/2003JD004460https://onlinelibrary.wiley.com/doi/abs/10.1029/2003JD004460https://agupubs.onlinelibrary.wiley.com/doi/10.1029/2003JD004460`.

W. C. Malm, J. F. Sisler, D. Huffman, R. A. Eldred, and T. A. Cahill. Spatial and seasonal trends in particle concentration and optical extinction in the United States. *Journal of Geophysical Research: Atmospheres*, 99(D1):1347–1370, 1994. doi: 10.1029/93JD02916. URL https://onlinelibrary.wiley.com/doi/full/10.1029/93JD02916https://onlinelibrary.wiley.com/doi/abs/10.1029/93JD02916https://agupubs.onlinelibrary.wiley.com/doi/10.1029/93JD02916.

Manchester University - Centre for Atmospheric Science. Black Carbon Aerosol. Technical report. URL http://www.cas.manchester.ac.uk/resactivities/aerosol/topics/black/.

H. Manninen. *Direct Detection Of Atmospheric Particle Formation Using The Neutral Cluster And Air Ion Spectrometer*, volume 122. 2011. ISBN 9789525822410. URL http://ethesis.helsinki.fi/.

H. Manninen, S. Mirme, A. Mirme, T. Petäjä, and M. Kulmala. How to reliably detect molecular clusters and nucleation mode particles with Neutral cluster and Air Ion Spectrometer (NAIS). *Atmospheric Measurement Techniques*, pages 3577–3605, 2016. doi: 10.5194/amt-9-3577-2016.

H. E. Manninen, T. Nieminen, E. Asmi, S. Gagné, S. Häkkinen, K. Lehtipalo, P. Aalto, M. Vana, A. Mirme, S. Mirme, U. Hõrrak, C. Plass-Dülmer, G. Stange, G. Kiss, A. Hoffer, N. Törő, M. Moerman, B. Henzing, G. de Leeuw, M. Brinkenberg, G. N. Kouvarakis, A. Bougiatioti, N. Mihalopoulos, C. O'Dowd, D. Ceburnis, A. Arneth, B. Svenningsson, E. Swietlicki, L. Tarozzi, S. Decesari, M. C. Facchini, W. Birmili, A. Sonntag, A. Wiedensohler, J. Boulon, K. Sellegri, P. Laj, M. Gysel, N. Bukowiecki, E. Weingartner, G. Wehrle, A. Laaksonen, A. Hamed, J. Joutsensaari, T. Petäjä, V.-M. Kerminen, and M. Kulmala. Eucaari ion spectrometer measurements at 12 european sites – analysis of new particle formation events. *Atmospheric Chemistry and Physics*, 10(16):7907–7927, 2010a. doi: 10.5194/acp-10-7907-2010. URL https://acp.copernicus.org/articles/10/7907/2010/.

H. E. Manninen, T. Nieminen, E. Asmi, S. Gagné, S. Häkkinen, K. Lehtipalo, P. Aalto, M. Vana, A. Mirme, S. Mirme, U. Hõrrak, C. Plass-Dülmer, G. Stange, G. Kiss, A. Hoffer, N. Töro, M. Moerman, B. Henzing, G. De Leeuw, M. Brinkenberg, G. N. Kouvarakis, A. Bougiatioti, N. Mihalopoulos, C. O'Dowd, D. Ceburnis, A. Arneth, B. Svenningsson, E. Swietlicki, L. Tarozzi, S. Decesari, M. C. Facchini, W. Birmili, A. Sonntag, A. Wiedensohler, J. Boulon, K. Sellegri, P. Laj, M. Gysel, N. Bukowiecki, E. Weingartner, G. Wehrle, A. Laaksonen, A. Hamed, J. Joutsensaari, T. Petäjä, V. M. Kerminen, and M. Kulmala. EUCAARI ion spectrometer measurements at 12 European sites-analysis of new particle formation events. *Atmospheric Chemistry and Physics*, 10(16):7907–7927, 2010b. doi: 10.5194/acp-10-7907-2010.

H. Matsui, M. Koike, Y. Kondo, N. Takegawa, A. Wiedensohler, J. D. Fast, and R. A. Zaveri. Impact of new particle formation on the concentrations of aerosols and cloud condensation nuclei around Beijing. *Journal of Geophysical Research: Atmospheres*, 116(D19):19208, 2011. doi: 10.1029/2011JD016025. URL https://agupubs.onlinelibrary.wiley.com/doi/full/10.1029/2011JD016025https://agupubs.onlinelibrary.wiley.com/doi/abs/10.1029/2011JD016025https://agupubs.onlinelibrary.wiley.com/doi/10.1029/2011JD016025.

G. Mcfiggans, P. Artaxo, U. Baltensperger, H. Coe, M. C. Facchini, G. Feingold, S. Fuzzi, M. Gysel, A. Laaksonen, U. Lohmann, T. F. Mentel, D. M. Murphy, C. D. O'dowd, J. R. Snider, and E. Weingartner. The effect of physical and chemical aerosol properties on warm cloud droplet activation. *Atmos. Chem. Phys*, 6:2593–2649, 2006. URL www.atmos-chem-phys.net/6/2593/2006/.

J. Merikanto, D. V. Spracklen, G. W. Mann, S. J. Pickering, and K. S. Carslaw. Impact of nucleation on global CCN. *Atmospheric Chemistry and Physics*, 9:8601–8616, 2009. URL www.atmos-chem-phys.net/9/8601/2009/.

S. Mirme and A. Mirme. The mathematical principles and design of the NAIS – a spectrometer for the measurement of cluster ion and climate of the past nanometer aerosol size distributions. *Atmospheric Measurement Techniques*, pages 1061–1071, 2013. doi: 10.5194/amt-6-1061-2013.

T. Nieminen, V.-M. Kerminen, T. Petäjä, P. P. Aalto, M. Arshinov, E. Asmi, U. Baltensperger, D. C. S. Beddows, J. P. Beukes, D. Collins, A. Ding, R. M. Harrison, B. Henzing, R. Hooda, M. Hu, U. Hõrrak, N. Kivekäs, K. Komsaare, R. Krejci, A. Kristensson, L. Laakso, A. Laaksonen, W. R. Leaitch, H. Lihavainen, N. Mihalopoulos, Z. Németh, W. Nie, C. O'dowd, I. Salma, K. Sellegri, B. Svenningsson, E. Swietlicki, P. Tunved, V. Ulevicius, V. Vakkari, M. Vana, A. Wiedensohler, Z. Wu, A. Virtanen, and M. Kulmala. Global analysis of continental boundary layer new particle formation based on long-term measurements. *Atmospheric Chemistry and Physics*, 18:14737–14756, 2018. doi: 10.5194/acp-18-14737-2018. URL https://doi.org/10.5194/acp-18-14737-2018.

H. J. Oh, Y. Ma, and J. Kim. Human inhalation exposure to aerosol and health effect: Aerosol monitoring and modelling regional deposited doses. *International Journal of Environmental Research and Public Health*, 17(6), 2020. doi: 10.3390/ijerph17061923. URL https://www.ncbi.nlm.nih.gov/pmc/articles/PMC7142517/.

A. Petzold, J. A. Ogren, M. Fiebig, P. Laj, S.-M. Li, U. Baltensperger, T. Holzer-Popp, S. Kinne, G. Pappalardo, N. Sugimoto, C. Wehrli, A. Wiedensohler, and X.-Y. Zhang. Recommendations for reporting "black carbon" measurements. *Atmospheric Chemistry and Physics*, 13:8365–8379, 2013. doi: 10.5194/acp-13-8365-2013. URL www.atmos-chem-phys.net/13/8365/2013/.

C. A. Pope III, R. T. Burnett, M. J. Thun, E. E. Calle, D. Krewski, K. Ito, and G. D. Thurston. Lung cancer, cardiopulmonary mortality, and long-term exposure to fine particulate air pollution. *JAMA*, 287(9):1132–1141, 2002. doi: 10.1001/JAMA.287.9.1132. URL https://jamanetwork.com/journals/jama/fullarticle/194704.

U. Pöschl, D. Rose, and M. O. Andreae. Part 2: Particle Hygroscopicity and Cloud Condensation Nucleus Activity. In *Clouds in the Perturbed Climate System: Their Relationship to Energy Balance, Atmospheric Dynamics, and Precipitation*, pages 58–72. MIT Press, 2009. ISBN 9780262255448. URL https://ieeexplore.ieee.org/xpl/ebooks/bookPdfWithBanner.jsp?fileName=6279662.pdf&bkn=6267202&pdfType=chapter.

B. Pushpawela, R. Jayaratne, and L. Morawska. Temporal distribution and other characteristics of new particle formation events in an urban environment. *Environmental Pollution*, 233:552–560, 2018. doi: 10.1016/J.ENVPOL.2017.10.102.

V. Ramanathan. Atmospheric brown clouds: Health, climate and agriculture impacts. *Scripta Varia*, 2006. URL www.pas.va/content/dam/accademia/pdf/sv106/sv106-ramanathan.pdf.

M. Raza, L. Chen, F. Leach, and S. Ding. A review of particulate number (PN) emissions from Gasoline Direct Injection (GDI) engines and their control techniques. *Energies*, 11(6), 2018. doi: 10.3390/en11061417.

C. L. Reddington, K. S. Carslaw, D. V. Spracklen, M. G. Frontoso, L. Collins, J. Merikanto, A. Minikin, T. Hamburger, H. Coe, M. Kulmala, P. Aalto, H. Flentje, C. Plass-D, . Ulmer, W. Birmili, A. Wiedensohler, B. Wehner, T. Tuch, A. Sonntag, C. D. O'dowd, S. G. Jennings, R. Dupuy, U. Baltensperger, E. Weingartner, H.-C. Hansson, P. Tunved, P. Laj, K. Sellegri, J. Boulon, J.-P. Putaud, C. Gruening, E. Swietlicki, P. Roldin, J. S. Henzing, M. Moerman, N. Mihalopoulos, G. Kouvarakis, V. . Zdímal, N. Zíková, A. Marinoni, P. Bonasoni, and R. Duchi. Primary versus secondary contributions to particle number concentrations in the European boundary layer. *Atmosospheric Chemistry Physics*, 11:12007–12036, 2011. doi: 10.5194/acp-11-12007-2011. URL www.atmos-chem-phys.net/11/12007/2011/.

M. Rotach and P. Calanca. Boundary layer meteorology (651-4053-05L): Boundary layer cycle, lecture notes, ETHZ. *ETHZ*, 2019.

I. Salma and Z. Németh. Dynamic and timing properties of new aerosol particle formation and consecutive growth events. *Atmospheric Chemistry and Physics*, 19(9):5835–5852, 2019. doi: 10.5194/acp-19-5835-2019. URL https://acp.copernicus.org/articles/19/5835/2019/.

E. S. Saltzman. Marine aerosols. *Geophysical Monograph Series*, 2009. doi: 10.1029/2008GM000769. URL https://escholarship.org/uc/item/5kb8309g.

A. Sandu. Piecewise polynomial solutions of aerosol dynamic equation. *Aerosol Science and Technology*, 40(4):261–273, 2006. doi: 10.1080/02786820500543274. URL https://www.tandfonline.com/action/journalInformation?journalCode=uast20.

J. Schmale, S. Henning, S. Decesari, B. Henzing, H. Keskinen, K. Sellegri, J. Ovadnevaite, M. Pöhlker, J. Brito, A. Bougiatioti, A. Kristensson, N. Kalivitis, I. Stavroulas, S. Carbone, A. Jefferson, M. Park, P. Schlag, Y. Iwamoto, P. Aalto, M. Äijälä, N. Bukowiecki, M. Ehn, R. Fröhlich, A. Frumau, E. Herrmann, H. Herrmann, R. Holzinger, G. Kos, M. Kulmala, N. Mihalopoulos, A. Nenes, C. O'Dowd, T. Petäjä, D. Picard, C. Pöhlker, U. Pöschl, L. Poulain, E. Swietlicki, M. Andreae, P. Artaxo, A. Wiedensohler, J. Ogren, A. Matsuki, S. Soo Yum, F. Stratmann, U. Baltensperger, and M. Gysel. Long-term cloud condensation nuclei number concentration, particle number size distribution and chemical composition measurements at regionally representative observatories. *Atmospheric Chemistry and Physics*, 18(4):2853–2881, 2018. doi: 10.5194/ACP-18-2853-2018.

J. H. Seinfeld and S. N. Pandis. *Atmospheric Chemistry And Physics: From Air Pollution To Climate Change*. John Wiley and Sons, New York, 2006. ISBN 9781118947401.

A. K. Shrestha, A. Thapa, and H. Gautam. Solar radiation, air temperature, relative humidity, and dew point study: Damak, jhapa, Nepal. *International Journal of Photoenergy*, 2019, 2019. doi: 10.1155/2019/8369231.

M. Shrivastava, C. D. Cappa, J. Fan, A. H. Goldstein, A. B. Guenther, J. L. Jimenez, C. Kuang, A. Laskin, S. T. Martin, N. L. Ng, T. Petaja, J. R. Pierce, P. J. Rasch, P. Roldin, J. H. Seinfeld, J. Shilling, J. N. Smith, J. A. Thornton, R. Volkamer, J. Wang, D. R. Worsnop, R. A. Zaveri, A. Zelenyuk, and Q. Zhang. Recent advances in understanding secondary organic aerosol: Implications for global climate forcing. *Reviews of Geophysics*, 2016. doi: 10.1002/2016RG000540.

S.-L. Sihto, M. Kulmala, V.-M. Kerminen, M. Dal Maso, T. Petäjä, I. Riipinen, H. Korhonen, F. Arnold, R. Janson, M. Boy, A. Laaksonen, and K. E. J. Lehtinen. Atmospheric sulphuric acid and aerosol formation: implications from atmospheric measurements for nucleation and early growth mechanisms. *Atmosospheric Chemistry and Physics*, 6:4079–4091, 2006. URL `www.atmos-chem-phys.net/6/4079/2006/`.

A. Singh and S. Dey. Influence of aerosol composition on visibility in megacity Delhi. *Atmospheric Environment*, 62: 367–373, 2012. doi: 10.1016/J.ATMOSENV.2012.08.048.

D. Stauffer and C. S. Kiang. Heteromolecular nucleation theory for multicomponent gas mixtures. *Tellus*, 26(1-2):295–297, 1974. doi: 10.1111/j.2153-3490.1974.tb01981.x. URL `http://tellusa.net/index.php/tellusa/article/view/9800`.

M. o. S. Swiss Confederation, 2021. URL `https://map.geo.admin.ch/`.

J. Tröstl, W. K. Chuang, H. Gordon, M. Heinritzi, C. Yan, U. Molteni, L. Ahlm, C. Frege, F. Bianchi, R. Wagner, M. Simon, K. Lehtipalo, C. Williamson, J. S. Craven, J. Duplissy, A. Adamov, J. Almeida, A. K. Bernhammer, M. Breitenlechner, S. Brilke, A. Dias, S. Ehrhart, R. C. Flagan, A. Franchin, C. Fuchs, R. Guida, M. Gysel, A. Hansel, C. R. Hoyle, T. Jokinen, H. Junninen, J. Kangasluoma, H. Keskinen, J. Kim, M. Krapf, A. Kürten, A. Laaksonen, M. Lawler, M. Leiminger, S. Mathot, O. Möhler, T. Nieminen, A. Onnela, T. Petäjä, F. M. Piel, P. Miettinen, M. P. Rissanen, L. Rondo, N. Sarnela, S. Schobesberger, K. Sengupta, M. Sipilä, J. N. Smith, G. Steiner, A. Tomè, A. Virtanen, A. C. Wagner, E. Weingartner, D. Wimmer, P. M. Winkler, P. Ye, K. S. Carslaw, J. Curtius, J. Dommen, J. Kirkby, M. Kulmala, I. Riipinen, D. R. Worsnop, N. M. Donahue, and U. Baltensperger. The role of low-volatility organic compounds in initial particle growth in the atmosphere. *Nature*, 533(7604):527–531, 2016a. doi: 10.1038/nature18271. URL `https://www.nature.com/articles/nature18271`.

J. Tröstl, E. Herrmann, C. Frege, F. Bianchi, U. Molteni, N. Bukowiecki, C. R. Hoyle, M. Steinbacher, E. Weingartner, J. Dommen, M. Gysel, and U. Baltensperger. Contribution of new particle formation to the total aerosol concentration at the high-altitude site Jungfraujoch (3580 m asl, Switzerland). *Journal of Geophysical Research: Atmospheres*, 121(19):11,692–11,711, 2016b. doi: 10.1002/2015JD024637. URL `https://agupubs.onlinelibrary.wiley.com/doi/full/10.1002/2015JD024637`.

TSI Incorporated. Model 3022A Condensation Particle Counter. (8), 2002. URL `http://www.tsi.com/documents/1933763i-3022A.pdf`.

TSI Incorporated. Model 3034 Scanning Mobility Particle Sizer. (3), 2003.

TSI Incorporated. Model 3776 Ultrafine Condensation Particle Condensation. (9), 2007.

TSI Incorporated. TSI knows nanoparticle measurement - nano instrumentation understanding, accelerated. Technical report, 2014.

TSI Incorporated. Scanning Mobility Particle Sizer Spectrometer 3034, 2020. URL `https://www.tsi.com/discontinued-products/scanning-mobility-particle-sizer-spectrometer-3034/`.

M. Vana, K. Komsaare, U. Hõrrak, S. Mirme, T. Nieminen, J. Kontkanen, H. E. Manninen, T. Petäjä, S. M. Noe, and M. Kulmala. Characteristics of new-particle formation at three SMEAR stations. 2016.

Ville de Payerne. Home | Municipality of Payerne, 2020. URL `https://www.payerne.ch/`.

R. Wagner, H. E. Manninen, A. Franchin, K. Lehtipalo, S. Mirme, G. Steiner, T. Petäjä, and M. Kulmala. On the accuracy of ion measurements using a Neutral cluster and Air Ion Spectrometer. *Boreal Environment Research*, 6095(5):230–241, 2016.

J. Wang, Y. Wu, X. Ge, Y. Shen, S. Ge, and M. Chen. Characteristics and sources of ambient refractory black carbon aerosols: Insights from soot particle aerosol mass spectrometer. *Atmospheric Environment*, 185:147–152, 2018. doi: https://doi.org/10.1016/j.atmosenv.2018.05.011. URL `https://www.sciencedirect.com/science/article/pii/S1352231018303145`.

R. J. Weber, J. J. Marti, P. H. McMURRY, F. L. Eisele, D. J. Tanner, and A. Jefferson. Measured atmospheric new particle formation rates: Implications for nucleation mechanisms. *Chemical Engineering Communications*, 151(1):53–64, 1996. doi: 10.1080/00986449608936541. URL `https://www.tandfonline.com/action/journalInformation?journalCode=gcec20`.

E. Weingartner. Aerosols I: Physical and Chemical Principles (402-0572-00L), Lecture 2: Measurement techniques, lecture notes. ETHZ. *ETHZ*, 2020.

N. Yanagisawa, K. Shibata, K. Ennya, Y. Tashiro, and K. Satou. VOCs and particle emission from DPF equipped diesel engine during regeneration measured by on-line PTR mass spectrometer. In *14th ETH-Conference on Combustion Generated Nanoparticles, Zürich, Switzerland*, 2010.

T. Yli-Juuti, T. Nieminen, A. Hirsikko, P. P. Aalto, E. Asmi, U. H. . Orrak, H. E. Manninen, J. Patokoski, M. Dal Maso, T. Petäjä, P. Petäj, P. Petäjä, J. Rinne, M. Kulmala, and I. Riipinen. Growth rates of nucleation mode particles in Hyytï aï a during 2003-2009: variation with particle size, season, data analysis method and ambient conditions. *Atmospheric Chemistry and Physics*, 11:21267–21317, 2011. doi: 10.5194/acpd-11-21267-2011. URL `www.atmos-chem-phys-discuss.net/11/21267/2011/`.

Acknowledgements

This work for my Master thesis at Paul Scherrer Institute (PSI), Laboratory for Atmospheric Chemistry (LAC) would not have been possible without the help of different people. For the support I receive during this period, I like to thank to all of them.

- **Prof. Dr. Margit Schwikowski** was the person who introduced PSI and their work to me. I like to thank you for being my supervisor and my responsible person at University of Bern.
- **Dr. Martin Gysel-Beer** was the person who pushed me out of my comfort zone through his scientific questions. He always had numerous solutions for each problem. I like to thank you for being my supervisor during the thesis.
- **Dr. Benjamin Tobias Brem** was the person who had the ideas of measurements. He always wanted to analyse different parameters, periods and so on because of his curiosity. Thank you for being my advisor and putting a lot of effort in the thesis.
- **Dr. Lubna Dada** was the person who had the right answer for my scientific questions. Thank you for making nucleation to look easier!
- **Günther Wehrle** was the person who initiated me in how to survive a night on Jungfraujoch. I like to thank you for the stories and laughs.
- Thank you to all **Aerosol Physics Group members** who asked questions about my thesis during the weekly meetings.
- Last but not the least, a big thank you is for **my family** and **my husband**. Thank you for your support during this period, especially during pandemic times!

This work was supported by MeteoSwiss in the framework of the GAW-CH science programme, and by the Swiss State Secretariate for Research and Innovation in the framework of the ACTRIS research infrastructure.

Declaration of consent

on the basis of Article 30 of the RSL Phil.-nat. 18

Name/First Name: Amarandi-Netedu Lidia-Marta

Registration Number: 19-113-448

Study program: Graduate School of Climate Sciences

Bachelor ☐ Master ☑ Dissertation ☐

Title of the thesis: Investigating the Characteristics and Origins of Primary Ultrafine Particles and New Particle Formation Events at the Rural Payerne Observatory

Supervisor: Supervisor: Prof. Dr. Margit Schwikowski-Gigar
Co-supervisor: Dr. Martin Gysel-Beer

I declare herewith that this thesis is my own work and that I have not used any sources other than those stated. I have indicated the adoption of quotations as well as thoughts taken from other authors as such in the thesis. I am aware that the Senate pursuant to Article 36 paragraph 1 litera r of the University Act of 5 September, 1996 is authorized to revoke the title awarded on the basis of this thesis.

For the purposes of evaluation and verification of compliance with the declaration of originality and the regulations governing plagiarism, I hereby grant the University of Bern the right to process my personal data and to perform the acts of use this requires, in particular, to reproduce the written thesis and to store it permanently in a database, and to use said database, or to make said database available, to enable comparison with future theses submitted by others.

Place/Date

Olten, 07.11.2021

Signature